

Iana Cristina Camino Romero

## **Composite Tower Design**



**FRP++**

Advanced structural analysis and  
design using composite materials

Master Dissertation  
European Master Advanced Structural Analysis and  
Design using Composite Materials

Work developed under the supervision of  
**Professor Doctor Bruno Castanié**



Funded by  
the European Union

## DECLARATION

**Name:** Iana Cristina Camino Romero

**Email:** cristinacamino96@gmail.com    **Phone number:** +330632997709/+593982518547

**Citizen Card Number:** A9451529

**Title of the Thesis:** Composite Tower Design

**Supervisors:**

Professor Doctor Bruno Castanié

**Year of Conclusion:** 2025

Master Course in Advanced Structural Analysis and Design using Composite Materials

THE ENTIRE REPRODUCTION OF THIS THESIS IS AUTHORIZED ONLY FOR RESEARCH PURPOSES,  
UPON WRITTEN DECLARATION BY THE INTERESTED PERSON, WHICH IS COMMITTED TO.

University of Toulouse III Paul Sabatier, 15/08/2025

Signature:

## **ACKNOWLEDGEMENTS**

I would like to express my sincere gratitude to all my professors for their guidance and constant support throughout my academic journey. I am especially thankful to Professor Bruno Castanié for his dedicated mentorship and invaluable advice during the course of this project. I also wish to acknowledge Retis Solutions, whose support and provision of opportunities to explore this topic in depth were fundamental to the success of this work.

I am profoundly grateful to my family for their continuous encouragement, for making me believe that anything is possible, and for the sacrifices they have made to support my education and dreams. Their love, patience, and faith in me have been a constant source of motivation, and I dedicate this achievement to them. To God, I am thankful for granting me the strength, health, and perseverance to complete this work.

My thanks also go to the FRP++ consortium for awarding me the consortium scholarship. I am grateful to my classmates and colleagues for their collaboration and constructive discussions. I would also like to thank the University of Girona, the Université de Toulouse, and the Institute Clément Ader for providing the academic environment, resources, and facilities that made this research possible.

Finally, I wish to thank my friends, near and far, for their understanding, kindness, and encouragement during the most challenging moments of this journey.

# Conception de Tour Composite

## RESUME

Cette thèse étudie la faisabilité de remplacer les tours de télécommunication en acier conventionnelles par des structures en polymères renforcés de fibres (FRP), en se concentrant sur les matériaux en polymère renforcé de fibres de verre (GFRP) et de fibres de carbone (CFRP). La recherche suit la méthodologie GAP (Géométrie–Architecture–Processus), combinant la conception conceptuelle, la sélection des matériaux et l'évaluation des performances au moyen d'analyses par éléments finis dans Abaqus. Deux boucles de conception itératives ont été menées. La première a conservé la géométrie initiale de la tour en acier tout en remplaçant les matériaux par des FRP, afin d'évaluer la rigidité, le poids et les performances en état de service. La seconde a redessiné la géométrie afin d'exploiter les propriétés anisotropes des FRP, en intégrant des solutions telles que le profil conique et des dispositions alternatives de contreventement, et a étudié des configurations en GFRP pur, hybrides GFRP–CFRP et en CFRP pur. Le comportement structurel des tours a été analysé selon les scénarios de chargement définis par l'Eurocode, y compris les états limites de service et les états limites ultimes. Les résultats montrent que le GFRP permet une réduction significative du poids et offre une excellente résistance à la corrosion, mais a du mal à respecter les limites de serviceabilité sans optimisation géométrique importante. En revanche, les configurations en CFRP et hybrides atteignent une meilleure rigidité et respectent les exigences de serviceabilité, bien que leur coût en matériaux soit plus élevé.

Dans l'ensemble, les résultats démontrent que les tours en FRP constituent une alternative prometteuse et durable aux structures en acier traditionnelles, en réduisant les besoins de maintenance et en améliorant la durabilité. Toutefois, une optimisation supplémentaire de la géométrie, des systèmes d'assemblage et des dispositions de matériaux, ainsi qu'une validation expérimentale à grande échelle, sont nécessaires avant une adoption généralisée.

**MOTS-CLES:** Polymères renforcés de fibres (FRP) ; Tour de télécommunication ; Analyse par éléments finis (FEA) ; Méthodologie GAP ; Eurocode ; Durabilité.

# Composite Tower Design

## ABSTRACT

This thesis investigates the feasibility of replacing conventional steel telecommunication towers with structures made from fibre-reinforced polymers (FRP), focusing on glass fibre reinforced polymer (GFRP) and carbon fibre reinforced polymer (CFRP) materials. The research follows the GAP (Geometry–Architecture–Process) methodology, combining conceptual design, material selection, and performance evaluation through finite element analysis in Abaqus. Two iterative design loops were conducted. The first maintained the original steel tower geometry while substituting FRP materials to assess stiffness, weight, and serviceability performance. The second redesigned the geometry to exploit the anisotropic properties of FRP, incorporating features such as tapering and alternative bracing arrangements, and explored full GFRP, hybrid GFRP–CFRP, and full CFRP configurations.

The structural behaviour of the towers was analysed under Eurocode-defined loading scenarios, including serviceability and ultimate limit states. Results indicate that GFRP offers substantial weight reduction and corrosion resistance but struggles to meet serviceability limits without significant geometric optimisation. In contrast, CFRP and hybrid configurations achieve improved stiffness and compliance with serviceability requirements, though at higher material costs.

Overall, the findings demonstrate that FRP towers are a promising and sustainable alternative to traditional steel structures, offering reduced maintenance demands and enhanced durability. However, further optimisation of geometry, joint systems, and material layouts, as well as full-scale experimental validation, are necessary steps before widespread adoption can be achieved.

**KEYWORDS:** Fibre-Reinforced Polymers (FRP); Telecommunication Tower; Finite Element Analysis (FEA); GAP Methodology; Eurocode; Sustainability.

# TABLE OF CONTENTS

Acknowledgements.....	III
Résumé.....	IV
Abstract.....	V
Table of Contents .....	VI
List of Figures.....	X
List of Tables.....	XII
List of Abbreviations and Symbols.....	XIV
1. Introduction .....	1
1.1. Motivation.....	2
1.2. Objectives.....	3
1.3. Structure of the Dissertation.....	4
2. Literature Review .....	6
2.1. Fiber Reinforced Polymers (FRP) .....	6
2.1.1. Composite materials.....	6
2.1.2. Fiber Reinforced Polymers (FRP).....	7
2.1.3. Fiber Reinforcements in Composite Materials.....	8
2.1.4. Matrix Materials in Composite Materials .....	10
2.2. Telecommunication tower .....	12
2.2.1. History of telecommunication structures .....	12
2.2.2. Overview and Importance .....	12
2.2.3. Structural Classification of Towers.....	13
2.2.4. Design Considerations and Structural Efficiency .....	15
2.2.5. Sustainability in Telecommunication Structures .....	16
2.3. FRP Lattice Structures.....	17
2.3.1. Lattice structures.....	17
2.3.2. FRP trusses.....	19
2.4. Previous studies.....	21
2.4.1. Case Studies .....	21

2.4.2.	FRP Towers vs Steel Towers .....	23
2.5.	Structural Behaviour of FRP Towers.....	25
2.5.1.	Wind-Induced Dynamic Response .....	25
2.5.2.	Failure Mechanisms and Buckling Behaviour.....	25
2.5.3.	Long-Term Performance and Creep Effects .....	26
2.6.	Manufacturing .....	27
2.6.1.	Filament Winding.....	27
2.6.2.	Pultrusion.....	28
2.6.3.	Joining techniques.....	30
2.7.	Design Actions and Verification Criteria.....	34
2.7.1.	Permanent Actions – Dead Load.....	34
2.7.2.	Wind Actions .....	34
2.7.3.	Ice/Frost Actions.....	35
2.7.4.	Operational Actions.....	36
2.7.5.	Ultimate Limit State (ULS) .....	36
2.7.6.	Serviceability Limit State (SLS).....	36
2.7.7.	Design Verification of Pultruded FRP Members.....	36
3.	Methodology.....	38
3.1.	Introduction .....	38
3.2.	Conceptual Design and Material Selection (GAP Methodology) .....	38
3.2.1.	Overview of the GAP Approach.....	38
3.2.2.	Design Alternatives Considered .....	39
3.2.3.	GAP Results and Final Configuration Selection.....	40
3.3.	Load Definition.....	42
3.3.1.	Permanent actions .....	42
3.3.2.	Wind Actions on Structure and Equipment .....	42
3.3.3.	Wind Actions on Antennas .....	48
3.3.4.	Operational actions.....	48
3.3.5.	Ice Frost Actions.....	49

3.3.6.	Load Combinations.....	49
3.4.	FRP Design Considerations .....	50
3.4.1.	Design Value of Resistance .....	50
3.4.2.	Partial Factors for Materials ( $\gamma_m$ ) .....	51
3.4.3.	Partial Factors for Resistance Models ( $\gamma_{Rd}$ ).....	52
3.4.4.	Conversion factor ( $\eta_c$ ) .....	52
3.4.5.	Long-term effects – Creep.....	52
3.5.	Finite Element Modelling in Abaqus.....	53
3.5.1.	Initial Geometry .....	53
3.5.2.	FEM Setup .....	54
3.6.	Structural Evaluation Criteria.....	60
3.6.1.	Axial tension .....	60
3.6.2.	Axial compression.....	61
3.6.3.	Bending.....	61
3.6.4.	Shear .....	62
4.	First Design Loop.....	64
4.1.	Model Description .....	64
4.2.	Material Properties.....	65
4.3.	Results of Load Calculation .....	65
4.4.	Comparison of results (Steel vs GFRP).....	69
4.4.1.	Maximum lateral displacement in Steel and GFRP Towers .....	69
4.4.2.	Maximum Stress in Steel and GFRP Towers .....	70
4.4.3.	Summary of results and verification .....	71
4.5.	Redesign for Stiffness Improvement .....	72
4.5.1.	Objective .....	72
4.5.2.	Wind Load Scenarios and Geometric Properties .....	73
4.5.3.	Iterative Design Modifications – Performance under SLS Combination .....	75
4.5.4.	Comparative Summary and Conclusion.....	82
5.	Second Design Loop .....	84

5.1.	Objective .....	84
5.2.	Setup.....	84
5.2.1.	Geometry .....	84
5.2.2.	Load Cases and Boundary Conditions .....	85
5.3.	Results and Selection of Small-Scale Prototypes .....	86
5.4.	Scaling to 36 m Tower .....	88
	Non-Tapered Towers .....	88
5.5.	Scaling to 36 m – Tapered Designs.....	91
5.6.	Discussion and Design Implications.....	95
5.7.	ULS Verification .....	96
6.	Results and Discussion .....	100
6.1.	First Design Loop Overview .....	100
6.2.	Second Design Loop Overview.....	101
6.3.	Discussion .....	103
6.3.1.	Consistency with Literature Findings .....	104
7.	Conclusion and Future Work .....	106
7.1.	Conclusions.....	106
7.2.	Future Work.....	107
8.	References .....	108

## LIST OF FIGURES

<b>Figure 2. 1:</b> Composite materials .....	6
<b>Figure 2. 2:</b> Composite materials in diverse industries, reproduced from [29], [30] .....	8
<b>Figure 2. 3:</b> Glass fibres, reproduced from [33] .....	9
<b>Figure 2. 4:</b> Glass fibres, reproduced from [34] .....	10
<b>Figure 2. 5:</b> Antennas and telecommunication tower, reproduced from [40] .....	13
<b>Figure 2. 6:</b> Self-supported towers, reproduced from [43] .....	14
<b>Figure 2. 7:</b> Guyed tower, reproduced from [1] .....	14
<b>Figure 2. 8:</b> Monopole, reproduced from [1] .....	15
<b>Figure 2. 9:</b> Composite grid-stiffened panel, adapted from [50] .....	18
<b>Figure 2. 10:</b> Composite lattice sandwich panel, reproduced from [52] .....	18
<b>Figure 2. 11:</b> IsoTruss lattice beam, adapted from [54] .....	19
<b>Figure 2. 12:</b> Examples of FRP trusses, reproduced from [23], [58] .....	20
<b>Figure 2. 13:</b> GFRP guyed tower, reproduced from [15] .....	21
<b>Figure 2. 14:</b> GFRP guyed tower, adapted from [19] .....	22
<b>Figure 2. 15:</b> Local buckling of GFRP profiles, adapted from [64]. .....	26
<b>Figure 2. 16:</b> Filament winding, reproduced from [68] .....	27
<b>Figure 2. 17:</b> WrapToR Truss, reproduced from [48] .....	28
<b>Figure 2. 18:</b> Pultrusion process, reproduced from [70] .....	29
<b>Figure 2. 19:</b> Composite tower – Valencia, reproduced from [72] .....	30
<b>Figure 2. 20:</b> Bolted connection, adapted from [20] .....	31
<b>Figure 2. 21:</b> Bonded connection and its failure mode, reproduced from [14] .....	32
<b>Figure 2. 22:</b> Bonded connection and its failure mode, reproduced from [14] .....	33
<b>Figure 3. 1:</b> Gap Methodology map .....	41
<b>Figure 3. 2:</b> Fundamental basic wind velocity map, obtained from [88] .....	43
<b>Figure 3. 3:</b> Considered wind directions .....	47
<b>Figure 3. 4:</b> Working platform .....	49
<b>Figure 3. 5:</b> Ice frost on the structural elements .....	49
<b>Figure 3. 6:</b> Diagram of the tower geometry .....	53
<b>Figure 3. 7:</b> Schematic of the tower geometry and element type .....	54
<b>Figure 3. 8:</b> Mechanical properties of materials .....	55

<b>Figure 3. 9:</b> Beam section and profiles .....	57
<b>Figure 3. 10:</b> Material orientation definition .....	57
<b>Figure 3. 11:</b> Boundary condition of the tower .....	58
<b>Figure 3. 12:</b> Definition of Dead Load and Wind Load Cases in the FEM Model .....	59
<b>Figure 3. 13:</b> Static analysis step .....	59
<b>Figure 3. 14:</b> Mesh definition .....	60
<b>Figure 3. 15:</b> Shear area formula, adapted from [85]. .....	62
<b>Figure 4. 1:</b> Cross-section distribution along the tower .....	65
<b>Figure 4. 2:</b> Maximum displacement U2 of the steel tower.....	69
<b>Figure 4. 3:</b> Maximum displacement U2 of the GFRP tower .....	70
<b>Figure 4. 4:</b> Maximum stress (Von Mises) of the steel tower.....	70
<b>Figure 4. 5:</b> Maximum axial stress (S11) of GFRP tower.....	71
<b>Figure 4. 6:</b> Maximum tip displacement – iteration 1 .....	76
<b>Figure 4. 7:</b> Maximum tip displacement – iteration 2 .....	77
<b>Figure 4. 8:</b> Maximum tip displacement – iteration 3 .....	77
<b>Figure 4. 9:</b> Maximum tip displacement – iteration 4 .....	78
<b>Figure 4. 10:</b> Maximum tip displacement – iteration 4.....	80
<b>Figure 4. 11:</b> Maximum tip displacement – iteration 6.....	81
<b>Figure 4. 12:</b> Maximum tip displacement – iteration 7.....	81
<b>Figure 5. 1:</b> Bracing configurations for triangular, square, and hexagonal prototypes .....	84
<b>Figure 5. 2:</b> Load application setup in prototype models (reference point) .....	85
<b>Figure 5. 3:</b> Specific displacement results for triangular geometry models.....	87
<b>Figure 5. 4:</b> Specific displacement results for square geometry models.....	87
<b>Figure 5. 5:</b> Specific displacement results for hexagonal geometry models .....	88
<b>Figure 5. 6:</b> Non-Tapered 36 m Tower Configuration .....	89
<b>Figure 5. 7:</b> Loads and wind incidence angles .....	89
<b>Figure 5. 8:</b> Tapered tower geometry.....	92
<b>Figure 5. 9:</b> Results of the tapered geometry .....	94
<b>Figure 6. 1:</b> Mass and tip displacement vs main member base diameter .....	101
<b>Figure 6. 2:</b> Prototype models selected based on specific displacement performance.....	102
<b>Figure 6. 3:</b> Observed tip displacement of a GFRP tower, reproduced from [19]. .....	105

## LIST OF TABLES

<b>Table 2. 1:</b> Comparison between FRP and Steel in Structural Applications.....	25
<b>Table 3. 1:</b> Proposed Composite Joint Configurations.....	40
<b>Table 3. 2:</b> Material partial factors .....	51
<b>Table 3. 3:</b> Resistance models partial factors ( $\gamma_{Rd}$ ).....	52
<b>Table 3. 4:</b> M2/Elium Glass Mechanical Properties (GFRP) .....	56
<b>Table 4. 1:</b> Member Profiles and Dimensions.....	64
<b>Table 4. 2:</b> Parameters for wind action calculations for each tower section (with and without frost) .	66
<b>Table 4. 3:</b> Antenna geometry and aerodynamic coefficients for wind action calculations .....	66
<b>Table 4. 4:</b> Calculated wind forces for structure, linear equipment, and antennas by section.....	67
<b>Table 4. 5:</b> Summary of permanent and variable loads applied to the reference tower .....	67
<b>Table 4. 6:</b> Load combinations (SLS and ULS) .....	68
<b>Table 4. 7:</b> Strength Verification of GFRP Pultruded Profiles under Maximum Stresses.....	71
<b>Table 4. 8:</b> Strength Verification of GFRP Pultruded Profiles under Maximum Stresses.....	72
<b>Table 4. 9:</b> Member Dimensions for Modified Tower Configurations.....	73
<b>Table 4. 10:</b> Governing SLS Loads per Tower Section for Modified Configurations .....	75
<b>Table 4. 11:</b> Results from iteration 1 .....	76
<b>Table 4. 12:</b> Results from iteration 2 .....	77
<b>Table 4. 13:</b> Results from iteration 3 .....	78
<b>Table 4. 14:</b> Results from iteration 4 .....	78
<b>Table 4. 15:</b> M1/Elium Carbon Mechanical Properties (CFRP) [90].....	79
<b>Table 4. 16:</b> Results from iteration 5 .....	80
<b>Table 4. 17:</b> Results from iteration 6 .....	81
<b>Table 4. 18:</b> Results from iteration 7 .....	82
<b>Table 4. 19:</b> Performance Summary of First Design Loop (SLS with Long-Term Coefficient Applied)	82
<b>Table 5. 1:</b> Summary of Prototype-Scale Tower Models and Performance Metrics.....	86
<b>Table 5. 2:</b> Non-tapered 36 m tower displacement results for selected geometries. ....	90
<b>Table 5. 3:</b> Structural performance of non-tapered 36 m tower configurations .....	91
<b>Table 5. 4:</b> Tapered 36 m tower displacement results for selected geometries.....	93
<b>Table 5. 5:</b> Structural performance of tapered 36 m tower configurations.....	93
<b>Table 5. 6:</b> Structural verification of main members – legs, X-bracing GFRP tower .....	96

<b>Table 5. 7:</b> Structural verification of diagonals – X-bracing GFRP tower .....	98
<b>Table 5. 8:</b> Structural verification of horizontals – X-bracing GFRP tower .....	98
<b>Table 6. 1:</b> Key results from the first design loop used for interpretation .....	100
<b>Table 6. 2:</b> Key results from the second design loop – non-tapered towers .....	102
<b>Table 6. 3:</b> Key results from the second design loop – tapered towers.....	103

# LIST OF ABBREVIATIONS AND SYMBOLS

## Abbreviations

CAD	Computer-Aided Design
CFRP	Carbon Fibre Reinforced Polymer
CO <sub>2</sub>	Carbon Dioxide
FEM	Finite Element Modelling
FRP	Fibre Reinforced Polymer
GAP	Geometry–Architecture–Procedure
GFRP	Glass Fibre Reinforced Polymer
ISO	International Organization for Standardization
LCA	Life Cycle Assessment
LCC	Life Cycle Cost
NA	National Annex
RF	Reserve Factor
S11	Axial stress in fibre direction (1-direction)
S22	Axial stress in 2-direction
S33	Axial stress in 3-direction
SLS	Serviceability Limit State
T <sub>g</sub>	Glass transition temperature
UD	Unidirectional
ULS	Ultimate Limit State
U2	Tip displacement in direction Y

## Symbols

A <sub>v</sub>	Shear area of the cross-section
A <sub>f</sub>	Reference area (wind load)
C <sub>f</sub>	Force coefficient
C <sub>scd</sub>	Structural factor
c <sub>0</sub>	Orography coefficient
E <sub>11</sub>	Elastic modulus in 1-direction
E <sub>22</sub>	Elastic modulus in 2-direction

$E_{33}$	Elastic modulus in 3-direction
$f_{11,c}$	Compressive strength in 1-direction
$f_{11,t}$	Tensile strength in 1-direction
$f_{22,c}$	Compressive strength in 2-direction
$f_{22,t}$	Tensile strength in 2-direction
$f_{xy,v,k}$	Characteristic in-plane shear strength
$G_{12}$	Shear modulus in 1–2 plane
$G_{13}$	Shear modulus in 1–3 plane
$G_{23}$	Shear modulus in 2–3 plane
$H_{ref}$	Reference height of the tower
$I_v$	Wind turbulence intensity
$M_{ed}$	Design value of applied bending moment
$M_{Rd}$	Design bending moment resistance
$S_{11}$	Axial stress in fibre direction (1-direction)
$S_{22}$	Axial stress in 2-direction
$S_{33}$	Axial stress in 3-direction
$u_2$	Tip displacement (transverse)
$\nu_{12}$	Poisson's ratio in 1–2 direction
$\nu_{13}$	Poisson's ratio in 1–3 direction
$\nu_{23}$	Poisson's ratio in 2–3 direction
$V_{Rd}$	Design shear resistance
$\gamma_{Rd}$	Partial safety factor for resistance
$\gamma_m$	Partial safety factor for material
$\eta_c$	Conversion factor
$\theta$	Tilt angle

THIS PAGE WAS INTENTIONALLY LEFT BLANK

## 1. INTRODUCTION

Telecommunication towers are critical infrastructures that support antennas used to transmit and receive radio signals, enabling communication systems essential for individuals, businesses, commerce, and governments. These systems form the foundation of today's interconnected and globalized world, where mobile phones and internet access have become indispensable elements of daily life and central to modern society [1], [2].

With the growing reliance on such technologies, the demand for telecommunication towers has increased significantly, along with the energy requirements needed to operate the corresponding radio stations [2], [3]. This trend has encouraged engineers and researchers to investigate innovative and sustainable design alternatives, incorporating environmentally friendly materials and optimized structural configurations [4].

Currently, telecommunication towers are commonly classified into three main types: monopoles, guyed masts, and self-supporting towers. These structures are primarily subjected to wind loads, which induce axial forces in tension or compression. Among them, self-supporting towers—lattice structures with triangular or rectangular bases—are widely used across Europe and globally, especially when a specific height is needed to ensure proper signal transmission (including microwave antennas, waveguides, and related devices). These towers are typically erected in hilly or remote terrain, ranging in height from 20 to 80 meters, and are often constructed using steel angle sections or tubular profiles arranged in a bracing pattern. A protective galvanized coating is applied to prevent corrosion from environmental exposure, and the towers are anchored to reinforced concrete foundations. This design allows for relatively straightforward assembly, making it particularly suitable for installations in hard-to-access locations [4], [5].

Nowadays, conventional steel telecommunication towers are increasingly affected by corrosion—a degradation phenomenon caused by electrochemical or chemical reactions when the metal is exposed to a corrosive environment for prolonged periods. Although corrosion can progress slowly, it inevitably occurs in all types of metals and significantly compromises the mechanical properties of structural components. This deterioration reduces the durability of towers and may even lead to premature structural failure, resulting in substantial economic losses. Corrosion-related issues have also been observed in lattice towers constructed with weathering steel, particularly at critical connection points such as leg member joints and anchorages [6], [7], [8], [9].

To mitigate this problem, preventive maintenance is essential. However, in many cases, maintenance is only performed when damage becomes clearly visible, making repairs more costly due to delayed intervention. According to industry standards, inspections should be conducted at least every five years, and more frequently in the event of extreme weather conditions such as storms or ice storms, or when towers are located in highly corrosive environments [8], [10]. Globally, the presence of corrosion in infrastructure results in an estimated \$2.5 trillion in annual expenditures for maintenance activities, including protective coatings and galvanization treatments [6], [11], [12]. In most cases, corrosion assessments rely on manual and visual inspections, which are labour-intensive, expensive, and prone to subjective interpretation [13].

In response to the durability issues—particularly corrosion—and high maintenance demands of conventional steel telecommunication towers, fibre-reinforced polymers (FRP) offer an innovative alternative due to their favourable mechanical properties. These include a high strength-to-weight ratio and excellent resistance to harsh environmental conditions [7], [14]. FRP materials present a viable solution for replacing steel in telecommunication structures, while also eliminating the need for protective coatings or galvanization. This establishes FRP as a material with sufficient stiffness and durability, capable of reducing lifecycle costs over the operational lifespan of the structure [15].

The aim of this study is to investigate the feasibility of replacing a conventional steel telecommunication tower with a structure made from Glass Fiber Reinforced Polymers (GFRP). The research focuses on comparing the stiffness and weight of the GFRP tower with those of a steel counterpart. Additionally, a custom joint is proposed to take advantage of the anisotropic properties of the composite material. The study follows the GAP (Geometry–Assembly–Performance) methodology and employs finite element analysis (FEA) to evaluate structural behaviour, considering the relevant loading conditions and design guidelines established by the Eurocodes.

### **1.1. Motivation**

FRPs have demonstrated significant potential not only in terms of structural performance but also from an economic and environmental perspectives. One of the key advantages of FRPs is their impact on life cycle economic analysis. Although the initial cost of FRP materials is generally higher compared to conventional materials like steel, they offer substantial savings over the structure's lifespan due to minimal maintenance requirements and longer durability. This has been clearly demonstrated by the case study of three bridges in West Virginia. By using FRP profiles they extended the service life and reduced

maintenance, resulting in overall cost-effectiveness and demonstrated to be effective particularly in scenarios where regular maintenance is difficult or costly to perform [16]

FRPs combine excellent stiffness-to-weight ratios with good mechanical performance, making them ideal for modular, lightweight, and easy-to-assemble structures. Their corrosion resistance, low maintenance needs, and design flexibility make them attractive for infrastructure applications [17], [18], [19], [20].

Additionally, while conventional materials such as steel have a high environmental footprint—especially regarding CO<sub>2</sub> emissions during production and disposal—FRPs present a more sustainable alternative. They are already widely adopted in sectors like aerospace, automotive, and energy, and offer potential recyclability [19].

In recent years, numerous studies have explored the use of GFRP in structures such as transmission and telecommunication towers. Results highlight benefits such as reduced structural weight, corrosion resistance, and negligible maintenance, all of which contribute to more sustainable infrastructure. Given these advantages, the adoption of FRP in civil infrastructure has steadily increased over the past decade, especially in applications that demand durability under harsh environmental conditions and contribute to decarbonization efforts [21].

Despite these promising developments, the application of FRP in energy infrastructure, particularly in truss systems, remains limited. A major challenge lies in the joining of composite elements. While advanced fabrication technologies such as filament winding, anisogrid, or braiding provide innovative solutions, they come with high initial costs. In contrast, cost-effective approaches using pultruded GFRP profiles are underexplored. One key reason is the reliability concern associated with bolted joints, which often cause fibre tearing and local damage due to hole perforation. On the other hand, bonded joints raise concerns about long-term durability and environmental degradation [19], [22], [23], [24], [25].

Further research into GFRP-based telecommunication towers is needed to establish them as a sustainable alternative to conventional steel towers. Despite their proven advantages, GFRP is still underutilized in this field, requiring several studies — even in real-world conditions — to validate its structural performance. GFRP remains a highly promising material whose potential to replace traditional steel towers has yet to be realized.

### 1.2. Objectives

The objective of this study is to design and analyse a 36-metre telecommunication tower using FRP materials, specifically GFRP and CFRP. The design is intended to have a service life of 50 years, a

maximum allowable head offset of 0.66 degrees, and modular truss segments of 6 meters in height. The tower has been designed to support an antenna surface area of 24m<sup>2</sup>, which is located within the uppermost 12 metres of the structure (from 24 to 36 metres in height). The objective of this study is to assess the feasibility and structural performance of FRP towers as a sustainable alternative to traditional steel towers.

To achieve this aim, the study will pursue the following goals:

- To apply the Geometry-Architecture-Process (GAP) methodology to define the configuration, material, and manufacturing approach of the tower.
- To analyse the design actions acting on the tower in accordance with Eurocode standards.
- To simulate the structural behaviour of the FRP tower using FEA and compare it with a conventional steel tower.
- To evaluate the structural performance of the FRP tower under service and ultimate conditions.
- To verify the Serviceability Limit States (SLS), including tip displacement and tilt angle, as well as Ultimate Limit State (ULS) load combinations, to ensure the proper design of the tower.
- To compare the self-weight of the FRP tower with that of the reference steel tower.
- To assess different structural configurations and truss arrangements of the tower.

### 1.3. Structure of the Dissertation

This dissertation is organised into eight chapters. Chapter 1 introduces the motivation, objectives, scope, and research questions. Chapter 2 reviews the state of the art on FRP composites, telecommunication towers, and joining strategies, and highlights the gaps that motivate this work. Chapter 3 details the methodology, including the GAP analysis framework, the 36 m steel reference model, material datasets for GFRP and CFRP, the FEM setup in Abaqus, wind-load modelling per EN 1991-1-4/EN 1993-3-1 (French NA), and the SLS/ULS verification criteria. Chapter 4 reports the first design loop using the original steel geometry with FRP substitutions, discussing stiffness–mass trade-offs and serviceability checks. Chapter 5 presents the second design loop with a geometry redesign to exploit FRP anisotropy (e.g., tapering, bracing layouts) and calculated the ULS Verification. Chapter 6 highlights the results and discusses them in relation to similar findings in the literature. Chapter 7 concludes the study, noting limitations and directions for future research. Chapter 8 presents the references. The appendices compile wind-load calculations, material properties, and ULS verification.

THIS PAGE WAS INTENTIONALLY LEFT BLANK

## 2. LITERATURE REVIEW

### 2.1. Fiber Reinforced Polymers (FRP)

#### 2.1.1. Composite materials

Composite materials are the combination of two or more different materials to form a new one with superior properties compared to the individual constituents. This combination usually involves a reinforcing phase—such as fibres or particles—embedded within a continuous matrix (See Figure 2.1). The target is to enhance mechanical performance, such as stiffness, strength, or durability, by leveraging the strengths of each component. Composites can also be found in the nature some examples include wood and bone, where fibrous structures are embedded in a matrix-like material [26], [27].

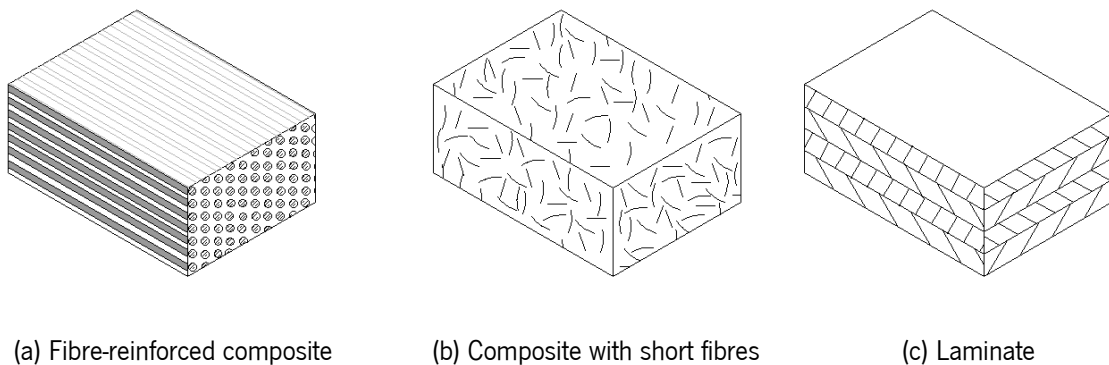


**Figure 2. 1:** Composite materials

Composite materials can be classified in several ways depending on their reinforcement type, structure, and matrix composition. One common classification is based on the type and arrangement of the reinforcement phase. These include particle-reinforced composites, which may have random or preferred orientations, and fibre-reinforced composites, which can be subdivided into continuous fibres—such as unidirectional, bidirectional (woven), or randomly oriented fibres—and discontinuous (short) fibres, which also follow random or preferential alignment. The mechanical behaviour of these composites is typically anisotropic, meaning their properties vary depending on direction. In unidirectional (UD) composites, for example, stiffness and strength are highest along the fibre direction, while transverse properties are dominated by the matrix [26], [27], [28].

Another important classification distinguishes between single-layer and multilayer composites, where the latter are typically called laminates. Laminates consist of multiple plies bonded together, either with the same fibre orientation or in varying orientations to optimize strength in multiple directions. When different types of reinforcements or materials are combined within the laminate—such as carbon fibres with glass or aramid—it is referred to as a hybrid laminate, offering a tailored balance of properties. In some advanced designs, even metallic sheets can be combined with fibre-reinforced composites to form hybrid structures [26], [27].

Composites may also be categorized according to the nature of the matrix material. These include polymeric matrices (such as thermosets, thermoplastics, or elastomers), metal matrices (metals, alloys, intermetallic), and ceramic matrices (oxides, non-oxides, and carbon-based ceramics). Among polymeric composites, thermosetting resins remain the most widely used due to their ease of processing and excellent structural performance. However, thermoplastic matrices are gaining popularity because they are tougher and recyclable [27].

### *2.1.2. Fiber Reinforced Polymers (FRP)*

Among modern composites, those that use a polymeric matrix—known as fibre-reinforced polymers—represent a widely used category, particularly in structural and high-performance applications. FRPs are composed of high-strength continuous fibres—most commonly glass or carbon—embedded in a polymeric matrix. The fibre phase is primarily responsible for carrying loads and providing stiffness, while the matrix ensures load transfer between fibres and offers protection from environmental degradation. This combination results in an anisotropic material, whose properties depend on fibre orientation. Engineers take advantage of this characteristic by aligning fibres along principal stress directions to maximize performance [24], [28].

FRPs are especially valued for their high specific strength and stiffness, which often surpass those of traditional materials like steel. GFRP components typically weigh only one-quarter as much as their steel equivalents, while CFRP components can be as light as one-tenth. These weight savings are particularly important in aerospace and automotive industries, as demonstrated in Figure 2.2; where reducing mass translates directly into lower fuel consumption [27].

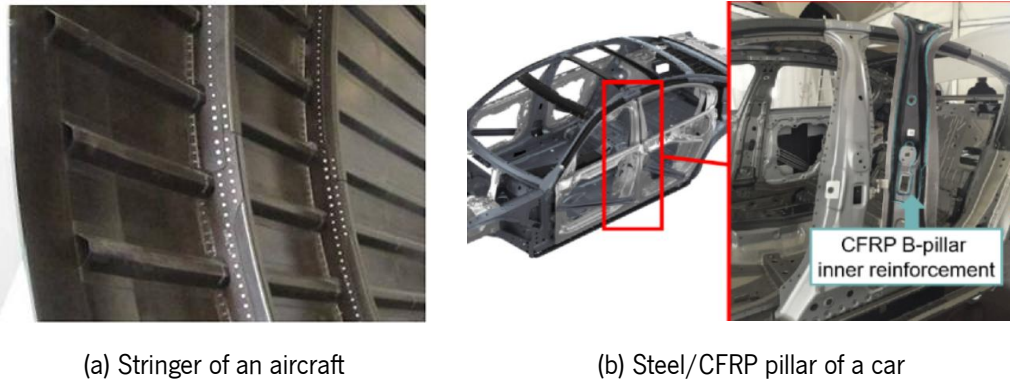


**Figure 2. 2:** Composite materials in diverse industries, reproduced from [29], [30]

The matrix phase in FRPs can be either thermoset or thermoplastic. Thermosetting resins—such as epoxies, vinyl esters, and polyesters—cure via cross-linking, resulting in a rigid, infusible structure that is difficult to recycle. Thermoplastics, on the other hand, consist of linear polymer chains that can be remelted and reshaped, making them recyclable and better suited for applications that require to be reshaped [28], [31].

In addition to their mechanical performance, FRPs offer several advantages: resistance to corrosion, fatigue, impact, and vibration; low energy consumption during production; and the ability to form complex shapes in a single manufacturing step. However, they also present drawbacks such as higher initial cost, susceptibility to damage in the transverse direction, difficulty in recycling—especially with thermosets—and the presence of manufacturing defects. Today, FRPs are used across diverse sectors, including civil engineering, automotive, wind energy, aerospace, marine, and medical applications [26], [27], [32], [33].

### 2.1.3. Fiber Reinforcements in Composite Materials

The fibre reinforcement phase plays a critical role in composite materials, as it primarily provides the strength and stiffness of the system. Fibers are typically much stronger and stiffer than the matrix and are also lightweight, making them highly efficient for structural applications. Depending on the application, various types of fibres can be used, including continuous or discontinuous (short) fibres, with different orientations such as unidirectional, bidirectional, or randomly distributed arrangements. The choice of fibre is usually based on performance requirements, cost, mechanical properties, and environmental factors [26].

#### Glass Fibers

Among synthetic fibres, glass fibres are the most widely used due to their affordability, corrosion resistance, environmental durability, and acceptable mechanical performance. They are produced by

melting a mixture of silica ( $\text{SiO}_2$ ), limestone, and other oxides, then extruding the melt into fine filaments typically 5 to 25  $\mu\text{m}$  in diameter. Several grades of glass fibre exist, including E-glass (electrical grade,  $\sim 3.5$  GPa strength), and S-glass (structural grade,  $\sim 4.8$  GPa strength), among others. Despite their widespread use, glass fibres have limitations such as a relatively low modulus of elasticity, poor abrasion resistance, and weak bonding with polymer matrices—often mitigated through protective coatings—They are commonly used in applications like filament winding and general industrial manufacturing [26], [34], [35].

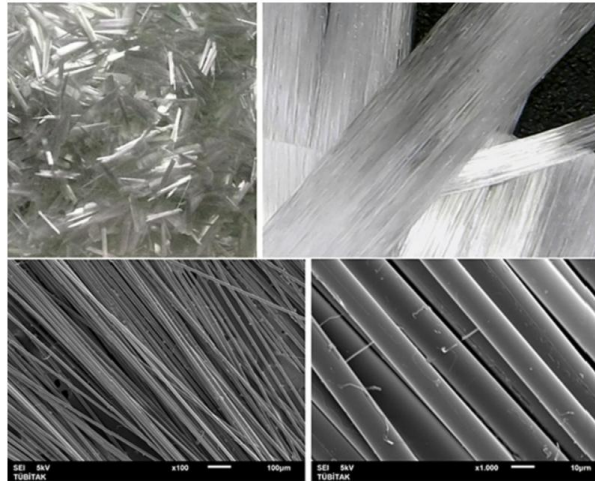


**Figure 2. 3:** Glass fibres, reproduced from [36]

### Carbon fibres

Carbon fibres are high-performance reinforcements known for their excellent strength-to-weight ratio, stiffness, chemical resistance, and low thermal expansion. These fibres are typically produced from polyacrylonitrile (PAN) or pitch precursors through thermal processes including stabilization, carbonization, and graphitization, which influence their mechanical properties. PAN-based fibres offer higher strength and dominate the market, while pitch-based fibres, which are more economical, exhibit larger crystalline structures but lower strength—about half the tensile strength and one-third the compressive strength of PAN fibres. Due to their high cost, carbon fibres are most used in aerospace, though they have also been adopted in civil engineering for retrofitting and strengthening concrete structures [26], [31], [32], [33], [35].



**Figure 2. 4:** Glass fibres, reproduced from [37]

### **Natural fibres**

Natural fibres such as hemp, jute, and flax, are derived from plant sources and are primarily composed of cellulose. These fibres exhibit variable mechanical properties depending on species, composition, and fibre orientation. Their mechanical behaviour is largely influenced by the angle of cellulose microfibrils; smaller angles result in higher strength and stiffness. While the variability among natural fibres is high, some types exhibit specific stiffness values comparable to glass fibres. Their advantages include low cost, renewable sourcing, low embodied energy, and good recyclability, making them attractive for sustainable applications [26]. A well-known example is wood, often considered the first bio-composite. Its use in mobility dates back to around 4000 BCE with early chariots and boats, and it has since been extensively studied, modelled, and optimized for applications in automotive, naval, and even aeronautic industries. Beyond its lightweight and mechanical performance, wood and plywood are also recognized for their sustainability, making them relevant eco-materials for modern design challenges [38].

#### *2.1.4. Matrix Materials in Composite Materials*

In fibre-reinforced polymer (FRP) composites, the matrix phase plays a fundamental role in binding the fibres together and forming the interface between them. While the fibres provide most of the strength and stiffness in the fibre direction, the matrix governs transverse strength, shear behaviour, and bearing stress, which are typically lower due to the matrix's comparatively lower mechanical properties. The matrix also defines the temperature range and environmental conditions the composite can endure, making it critical for durability and long-term performance [26].

Matrix materials can be metallic, ceramic, or polymeric; however, polymeric matrices are by far the most used in structural composites due to their ease of processing, lightweight, and low manufacturing cost.

Polymeric matrices are classified into thermosets and thermoplastics, each with distinct structural and performance characteristics [26], [39].

### **Thermoset Matrices**

Thermosetting polymers cure via an irreversible chemical reaction that forms a rigid, cross-linked molecular network. Once cured, they cannot be re-melted or reshaped, which limits their recyclability but ensures their high strength, dimensional stability, and excellent thermal and chemical resistance [39].

Common thermosets used in FRPs include epoxy, polyester, vinyl ester, and phenolic resins. Polyester resins, synthesized from polyhydric alcohol and dibasic organic acids, are among the most economical and widely used thermosets, however, they exhibit lower mechanical properties compared to other thermosets. Epoxy resins, produced by the cross-linking of epichlorohydrin and bisphenol compounds, offer superior mechanical performance, chemical resistance, and low shrinkage, making them ideal for high-performance applications—though at a higher cost. Thermosets lose their load-carrying capacity once heated above their glass transition temperature ( $T_g$ ), which limits their thermal service range [26], [34].

### **Thermoplastic Matrices**

Thermoplastics are polymers with linear or branched molecular chains that soften when heated and harden when solidification takes place, allowing them to be re-melted and reprocessed. This gives thermoplastics a key advantage in recyclability and toughness over thermosets. Their properties depend strongly on the crystallinity and temperature, and while they are generally more ductile than thermosets, their high melt viscosity can complicate fibre impregnation during manufacturing [35], [39].

Common thermoplastics used in composites include polypropylene (PP), polyethylene (PE), polyamide (PA), and polyetheretherketone (PEEK), PEEKs are used for more demanding structural applications and usually used in industries that require fast processing and reform-ability [39].

### **Novel Thermoplastic: Elium®**

An emerging innovation in matrix development is Elium, a liquid thermoplastic resin developed by Arkema, chemically based on methyl methacrylate (MMA). Unlike conventional thermoplastics, Elium cures at room temperature through peroxide-initiated polymerization, combining the low viscosity and easy fibre impregnation of thermosets with the recyclability of thermoplastics. Elium-based composites demonstrate mechanical performance comparable to epoxy systems in terms of tensile strength and stiffness, while offering superior toughness and impact resistance, which makes them particularly suitable for damage-tolerant applications [40].

## 2.2. Telecommunication tower

### 2.2.1. History of telecommunication structures

The development of telecommunication towers has evolved in parallel with advances in electronic communication. The first concept of transmission infrastructure was introduced by Claude Chappe in the 1790s, who developed the optical semaphore telegraph—a system of towers equipped with pivoting arms mounted on wooden structures. Messages were relayed visually from one tower to another using telescopes, creating a multi-hop communication network that did not require wires. The first operational line was built between Paris and Lille in 1794, consisting of 18 towers spaced approximately 10–15 km apart. This system later expanded across France and into other European countries [41].

One of the first documented uses of a steel tower for telecommunication purposes occurred in 1903 at the Eiffel Tower, where radio transmitters for wireless telegraphy were installed by the French military. In the early 20th century, public broadcasting via medium-frequency (MF) signals emerged, with timber towers—selected for their favourable electromagnetic properties—supporting early Marconi transmitters at heights of up to 64 meters. These were later replaced by steel masts, due to their superior structural performance and reaching up to 122 meters. By 1925, the world's first high-power low-frequency (long-wave) broadcasting station was established in Daventry, covering approximately 85% of the UK [42], [43]. As the industry progressed toward very-high frequency (VHF) transmission, tower designs also advanced. A significant milestone was reached in 1936 with the introduction of regular television and telephone service at Alexandra Palace, using a 65.6 m steel lattice tower built on the palace roof. Following World War II, the deployment of new VHF and Ultra High Frequency (UHF) stations accelerated, including the construction of a 219 m self-supporting tower at Crystal Palace in London in 1957 [43]. These developments laid the foundation for the modern telecommunication towers seen today, which are typically constructed as lattice structures, guyed masts, or monopoles depending on functional and environmental requirements.

### 2.2.2. Overview and Importance

Telecommunication towers are essential infrastructure in today's interconnected world, serving as the backbone for wireless communication networks. These structures support antennas and equipment for mobile communication, television and radio broadcasting, satellite links, and emergency response systems, as demonstrated in Figure 2.5. As internet access and digital services have become integral to

modern life—including education, work, government services, and entertainment—the demand for reliable and widespread telecommunication infrastructure continues to increase [2].



**Figure 2. 5:** Antennas and telecommunication tower, reproduced from [44]

This demand has intensified with the rollout of fifth generation (5G) mobile networks. 5G enables unprecedented transmission speeds, reduced latency, and massive device connectivity—key features for the development of smart cities, autonomous vehicles, the Internet of Things (IoT), and real-time applications such as remote surgery or industrial automation. To meet these requirements, 5G networks must achieve speeds of at least 20 Gbps for downlink and 10 Gbps for uplink, with a maximum latency of 4 milliseconds [45]. As a result, the installation of additional telecommunication towers and small-cell sites, particularly in urban areas, is needed.

Telecommunication towers play a vital role in both technological advancement and society development. Their strategic utilization of technology ensures that everyone, regardless of their geographical location, has access to the internet. The design, enhancement and selection of materials for these towers have become pivotal factors in determining their functionality, cost-effectiveness and environmental impact [2].

### *2.2.3. Structural Classification of Towers*

Telecommunication towers are primarily classified into three main types based on their structural system in self-supporting towers, guyed masts/towers and monopoles.

#### **Self-Supporting Towers**

As demonstrated in Figure 2.6, these towers have either triangular or square bases and consist of three-dimensional steel truss systems. They are tapered—wider at the base and narrower at the top—and use bracing systems such as K, X, Z, or D. X-bracing is often favoured for its superior structural performance.

Self-supporting towers are widely used due to their ability to support multiple antennas and their efficient land use in both rural and urban areas [1], [4], [46].



(a) Square self-supported tower



(b) Triangular self-supported tower

**Figure 2. 6:** Self-supported towers, reproduced from [47]

### Guyed towers

Consist of a central mast supported by tensioned cables at different heights that are anchored to the ground, typically with an anchor radius of about two-thirds the tower's height (See Figure 2.7). These are efficient and cost-effective for tall installations (usually over 60 m), especially in rural areas where land availability is less constrained. The mast or tower carries compressive loads while the cables resist tension. However, failure of any guy cable can lead to collapse, making proper installation and maintenance critical [1], [4].



**Figure 2. 7:** Guyed tower, reproduced from [1]

## Monopoles

Monopole towers are cantilever structures made from circular hollow steel sections, often tapered (See Figure 2.8). They are suitable for heights up to 40 m and are preferred in urban environments due to their compact footprint and better aesthetic appearance. Monopoles resist bending moments through their cross-section and generally require thicker material to achieve the necessary stiffness under wind loading [1], [4], [46].



**Figure 2. 8:** Monopole, reproduced from [1]

### *2.2.4. Design Considerations and Structural Efficiency*

The design and implementation of telecommunication towers is influenced by several site-specific factors and considerations of structural efficiency. These factors directly impact performance, safety, and cost-effectiveness. One of the most critical decisions is the selection of the tower site, which affects signal coverage, interference levels, and operational reliability. Optimal locations are those that provide maximum coverage at minimal cost, while avoiding topographic obstructions and minimizing exposure to extreme environmental conditions [48].

From a structural perspective, tower geometry, member configuration, and bracing systems play a central role in resisting external loads and optimizing material use. Telecommunication towers are subjected to various environmental actions such as wind, ice, snow, and in some regions, seismic forces. Wind is typically the governing load and is evaluated based on elevation, terrain roughness, topographic category, and local wind zones. Ice frost is also considered, not only for its additional self-weight but also for its

impact on the aerodynamic profile of the structure. These loads are generally analysed through static methods, although dynamic analysis may be required for taller or more flexible towers [43].

Self-supported towers can be categorized by their cross-sectional geometry, which directly affects their structural behaviour and torsional stiffness. Shapes include triangular, square, rectangular, hexagonal, and other polygonal configurations. Triangular cross-sections are the lightest and most economical but offer lower torsional rigidity. In contrast, square and hexagonal sections provide enhanced stability and are typically heavier—by approximately 10% and 20%, respectively, compared to triangular configurations [1]. The choice of cross-section is often determined by the required tower height and stiffness: triangular-based towers are efficient for heights between 20 m and 70 m, while square-based towers are preferred for taller structures exceeding 70 m [4].

The bracing configuration is another critical factor that influences the structural performance of telecommunication towers. Bracing systems such as X, K, Z, or D arrangements are selected based on design requirements, as they affect load distribution, global stiffness, and construction complexity [4].

#### *2.2.5. Sustainability in Telecommunication Structures*

With the growing number of towers worldwide, the environmental impact of traditional steel structures has become a concern. Steel production accounts for significant CO<sub>2</sub> emissions—representing approximately 15% of China's total greenhouse gas emissions—primarily due to the high embedded energy involved in extracting, processing, and transporting raw materials [2], [49]. As a response, sustainability goals (aligned with the UN's Sustainable Development Goals) call for the adoption of greener materials and designs.

Innovative strategies are being explored to reduce the environmental impact of telecommunication towers, particularly by substituting steel with more sustainable materials. One such initiative within the European Union aims to construct at least 1% of new telecommunication towers using engineered wood, which could lead to a reduction of approximately 17,000 t of CO<sub>2</sub> emissions. The wooden towers are currently undergoing testing, with prototypes developed in countries such as Hungary to evaluate their feasibility and long-term performance [2].

Concurrently, fibre-reinforced polymers (FRPs) are being considered as a viable alternative due to their lower embodied energy, corrosion resistance, and favourable strength-to-weight ratio. In comparison with steel, FRPs offer enhanced durability and diminished maintenance requirements, rendering them a compelling option for long-term sustainability in the telecommunications sector. These material

innovations contribute directly to the SDGs, particularly those related to climate action, sustainable cities and communities, responsible consumption and production, and industry, innovation, and infrastructure [2], [50], [51].

## 2.3. FRP Lattice Structures

### 2.3.1. Lattice structures

Lattice structures are spatial frameworks composed of primary and secondary members connected through joints. These systems are geometrically efficient because they are primarily loaded under axial forces—tension and compression—which makes them ideal for exploiting the anisotropic behaviour of FRP composites. When axial loading dominates, fibres can be strategically aligned along the load paths, thus maximizing the material's strength and stiffness in the desired directions [52].

Despite these advantages, the use of FRPs in lattice or truss structures remains relatively limited, particularly in large-scale infrastructure such as telecommunication towers. One of the primary challenges lies in the assembly and joining of members, especially when combining primary and secondary elements made of composites. Unlike metals, composites are not easily welded or bolted without compromising structural integrity, and bonding or co-curing methods often require precise manufacturing conditions [52].

One promising fabrication method for composite lattice structures is filament winding, where secondary or helical (shear) members are wound at specific angles around pre-placed primary members. These helical members are often co-cured or bonded during the winding process, forming an integrated truss or grid system [25], [52].

Composite lattice structures are typically categorized into:

- Composite grid-stiffened panels
- Composite lattice sandwich cores
- Composite lattice beams
- And systems formed using pultruded profiles joined mechanically or adhesively to form trusses

### **Composite grid-stiffened panels**

Composite grid-stiffened panels are lightweight, high-performance structural elements composed of a stiffening grid bonded to a thin skin, as shown in Figure 2.9. The grid is primarily responsible for efficient load distribution and can be configured in various patterns such as isogrid, orthogrid, or anglegrid. The

skin, on the other hand, provides aerodynamic coverage and resists localized damage, such as low-velocity impacts. These structures exhibit high stiffness and exceptional damage tolerance, as demonstrated by tests showing minimal strength reduction after impact. Due to these advantageous properties, composite grid-stiffened panels are widely applied in aerospace engineering, including in fuselage skins, airframes, and satellite components [33], [53], [54].



**Figure 2. 9:** Composite grid-stiffened panel, adapted from [54]

### **Composite lattice sandwich cores**

Composite lattice sandwich cores are structural cores used in sandwich panels as a replacement for conventional foam cores. They offer higher stiffness and strength, often utilizing carbon fibre for the fabrication of the trusses. These trusses are typically arranged in a pyramidal configuration and are manufactured together with the sandwich face sheets, which are commonly made from unidirectional (UD) carbon fibre prepregs. After curing, the core is bonded to the face sheets. These lattice cores exhibit superior compressive modulus and energy absorption, resulting in enhanced impact resistance, while maintaining relatively simple and efficient manufacturing processes [55], [56], [57].



**Figure 2. 10:** Composite lattice sandwich panel, reproduced from [56]

### **Composite lattice beams**

Composite lattice beams typically consist of longitudinal members (or chords) aligned with the beam axis to carry axial loads, and diagonal shear members that resist transverse loads. These beams are often fabricated using filament winding techniques. One of the most well-known technologies in this category is the IsoTruss (See Figure 2.11), which forms the lattice structure by winding fibres into six helical

members. In this system, Kevlar layers are wrapped around the joints to provide local reinforcement. Another manufacturing approach involves braiding carbon fibre tows around a cylindrical mandrel, using prepreg materials that are later consolidated. An additional example is the WrapToR truss, which employs filament winding to create a triangular cross-section composed of three helical chords and six helical shear members. A key advantage of these methods is the efficiency of manufacturing, as the axial and shear tows are cured simultaneously, resulting in a fully integrated composite lattice beam [24].



**Figure 2. 11:** IsoTruss lattice beam, adapted from [58]

Several studies have investigated the mechanical performance of composite lattice beam systems. One notable example is a numerical study analysing the use of an IsoTruss-based configuration for a 60 m tall, 1.5 MW wind turbine tower. This work assessed the structural efficiency and stability of different IsoTruss models using finite element simulations in ANSYS. The analysis focused on compressive buckling capacity, stress distribution, and vibrational response under both static and seismic loading. Among the configurations tested, the model with both internal and external longitudinal members exhibited the highest specific buckling load capacity (buckling load relative to weight) and the lowest deflection values. The study concluded that IsoTruss towers could offer significant weight reduction and improved structural performance compared to conventional steel tubular towers, indicating their potential for future wind energy applications, although their fabrication remains more costly than conventional steel solutions due to the complexity of manufacturing processes and higher material costs. [59].

### 2.3.2. FRP trusses

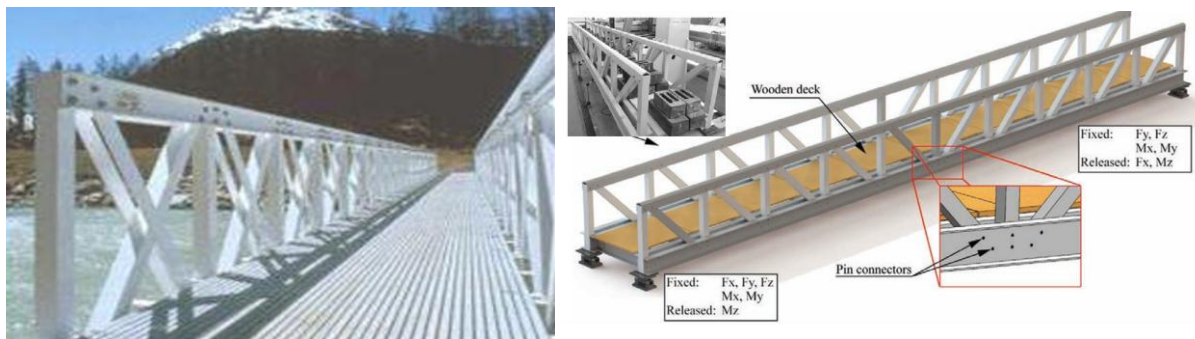
Trusses, a subclass of lattice structures, are typically made from triangular arrangements of members that ideally transfer only axial loads. Traditionally, connections are modelled as hinged or pinned, allowing free rotation at the joints. In practice, however, truss behaviour often deviates from this idealization, as

joints exhibit partial fixity and members are subjected to bending, shear, and torsion. FRP trusses benefit from the directional tailoring of fibres, allowing primary members to be optimized for axial loading, which enhances structural efficiency [24], [25].

FRP truss structures have been successfully applied in temporary and dismantlable bridge systems, where advantages such as lightweight for transport, rapid assembly, and reduced maintenance are especially valuable. In such applications, flexural buckling of diagonal members has been observed as a dominant failure mode, emphasizing the importance of joint design and member stability [60].

Historically, trusses date back to ancient Greek and Roman architecture, where they were used in timber roof construction. Today, they remain fundamental in the design of bridges, towers, roofs, and components in the aerospace and automotive industries. Their structural efficiency stems from the subdivision of global loads into local axial forces, which minimizes bending and enables optimized material use. However, one of the key limitations in truss design—especially for FRPs—is the requirement to individually join many members, increasing complexity in both design and manufacturing [61].

Examples of FRP truss structures include the Pontresina Bridge in Switzerland (See Figure 2.12 – a), a pedestrian bridge entirely constructed from pultruded GFRP profiles using a combination of bolted and bonded joints. Long-term durability assessments of the structure revealed no visible damage, confirming the suitability of FRP trusses for harsh outdoor environments [23]. Another case is shown in Figure 2.12 (b), a prototype pedestrian bridge developed in Lithuania by the Research Laboratory of Innovative Building Structures at Vilnius Gediminas Technical University. This bridge was designed, fabricated, and tested using GFRP pultruded profiles, bolted connections, and GFRP brackets. Experimental results confirmed that GFRP profiles exhibit adequate mechanical performance and structural behaviour for use in trussed pedestrian bridges [62].



(a) Pontresina Bridge

(b) Prototype pedestrian bridge - Lithuania

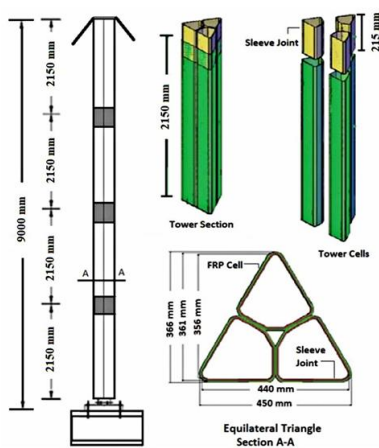
**Figure 2. 12:** Examples of FRP trusses, reproduced from [23], [62]

## 2.4. Previous studies

### 2.4.1. Case Studies

#### GFRP guyed tower of 81 meters

Alshurafa et al. conducted a series of studies demonstrating the feasibility and structural performance of GFRP guyed towers as viable alternatives to traditional steel structures. A full-scale 81 m GFRP guyed tower was modelled using ANSYS finite element software to simulate both static and dynamic behaviour under wind loading conditions. The structure consisted of 16 prismatic segments interconnected by internal sleeve joints, with a triangular cross-section and guyed using three sets of seven cables, each set oriented  $120^\circ$  apart, as illustrated in Figure 2.13. The tower was pinned at the base, and analyses were conducted in compliance with CSA-S37 requirements for ultimate and serviceability limit states. The chosen layup sequence of  $[90^\circ/0^\circ/0^\circ/90^\circ]$  provided an optimal balance of stiffness and deformation control. The dynamic analysis revealed that the natural frequencies of the full tower were significantly lower than those of short segments, likely due to the added mass of the guy cables. Using the Tsai–Wu failure criterion, maximum strain/stress criteria, the structure was verified to have a safety factor of 2.5, ensuring its reliability under critical load scenarios [11], [17].



(a) Geometry of the GFRP guyed tower



(b) Manufacturing of the tower

**Figure 2. 13:** GFRP guyed tower, reproduced from [15]

Furthermore, validation of their numerical model was performed by experimentally fabricating and testing a 9 m GFRP tower segment using a novel manufacturing approach based on a collapsible mandrel system. The prismatic tower cells were produced using unidirectional fiberglass mats and bonded via epoxy-infused sleeve joints. The experimental setup involved static testing to simulate wind loads, strain and deflection were measured, showing strong correlation with finite element predictions. The study

concluded that GFRP has high potential as a structural material for guyed communication towers, offering reduced weight, corrosion resistance, and significant cost savings [15].

### Case Study: 25 m GFRP-Steel Hybrid Self-Supporting Tower

One notable study explored the mechanical performance of a 25-meter self-supporting communication tower using GFRP pultruded pipes as the main vertical members, combined with steel components for secondary members and connections—resulting in a hybrid lattice structure, as illustrated in Figure 2.14. The motivation was to overcome the limitations of traditional steel towers, such as high weight and poor corrosion resistance, by evaluating the viability of GFRP composites as a structural alternative. The research involved material characterization of the GFRP components, followed by the design and analysis of the tower using large deflection theory to account for its nonlinear deformation behaviour under load. The connections were realized through steel inserts and adhesive bonding using a sleeved system [19].

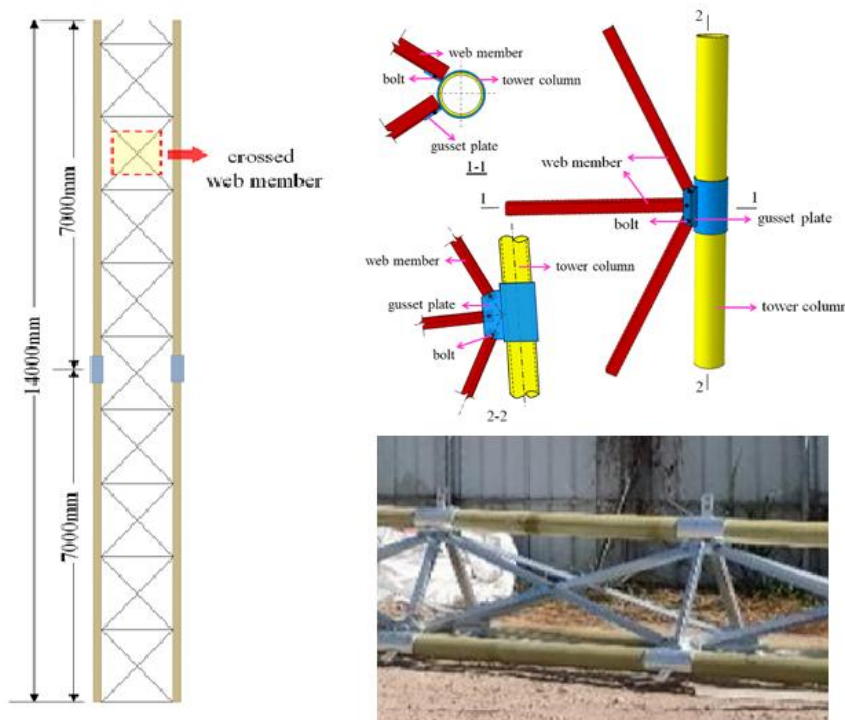


**Figure 2. 14:** GFRP guyed tower, adapted from [19].

The tower's structural response was assessed through both bending tests and finite element analysis under wind loading. The results indicated relatively high flexibility compared to steel towers, with maximum displacements of approximately 12% of the tower height under bending and 4.41% under simulated wind loads. Despite this, the structure demonstrated high resilience in a real-world installation in China, during a typhoon with wind speeds reaching 17.26 m/s, the measured top displacement was about 10 m (40% of the tower's height); despite the large displacement, the tower sustained no damage and remained in serviceable condition [19].

### **Stability Analysis of a 33.5 m Composite Transmission Lattice Tower**

A study conducted on a 220 kV power transmission tower explored the use of glass fibre reinforced polyamide in a full-scale lattice tower configuration. The structure of 36 meters height was designed to replace traditional steel towers with a lighter, corrosion-resistant alternative. The analysis included linear buckling simulations and modal analysis under wind loads to evaluate the tower's stability and dynamic behaviour. Results indicated that the composite tower exhibited deformation and critical load responses comparable to steel, suggesting that thermoplastic composites can offer structurally viable solutions for tall lattice structures [63]. Although the study focused on energy infrastructure, its findings provide valuable insight for the application of composite materials in telecommunication tower design.

### **Design and Analysis of a 30 m Pultruded GFRP Telecommunication Tower**

A 30-meter self-supporting telecommunication tower was designed and analysed using pultruded GFRP profiles to evaluate their potential as a structural replacement for conventional steel. The study adopted a modular approach, employing commercially available FRP members configured to replicate the geometry of standard steel lattice towers. The primary aim was to assess whether GFRP could meet the structural demands of telecom infrastructure while offering benefits such as reduced weight, corrosion resistance, and ease of installation [64].

The structural performance was evaluated through finite element analysis in ANSYS under dead load, wind pressure, and seismic conditions. The tower was modelled as a 3D truss system with pinned connections. Results showed that the GFRP configuration exhibited higher displacements compared to a conventional steel tower but remained within the allowable limits defined. These findings confirm the viability of pultruded GFRP profiles for use in self-supporting tower structures, while also highlighting the importance of accounting for serviceability performance and joint behaviour in future applications [64].

#### *2.4.2. FRP Towers vs Steel Towers*

Several studies have demonstrated the advantages of using FRPs over traditional steel in telecommunication tower design—particularly regarding weight reduction, corrosion resistance, and lifecycle cost-efficiency. For example, GFRP towers weigh approximately 30% of their steel counterparts, due to their lower material density ( $1.8 \times 10^3 \text{ kg/m}^3$  versus  $7.85 \times 10^3 \text{ kg/m}^3$ ), resulting in lighter foundations, easier transportation, and faster on-site assembly. Comparative cost analyses have shown that initial investment and maintenance costs for GFRP towers are approximately 59.46% and 29.33% lower, respectively, than for steel towers. These savings are largely attributed to the elimination of

corrosion-related maintenance, as FRP materials are inherently resistant to humidity, temperature fluctuations, ultraviolet radiation, and chemically aggressive environments [19]

In terms of durability and installation efficiency, GFRP towers also present clear benefits. Their projected service life exceeds 70 years, compared to roughly 50 years for steel towers. Moreover, GFRP towers can often be erected in just 7 days, while steel alternatives may require 15 days or more. Beyond durability, FRP materials offer superior chemical, thermal, and fire resistance, making them suitable for harsh environmental conditions where steel performance deteriorates. From a structural perspective, FRP failures are governed by local buckling or fibre rupture along the principal material axes, reflecting the anisotropic behaviour of unidirectional composites. Additionally, some studies have reported up to a 62% reduction in total structural mass when using GFRP, further reinforcing its suitability for sustainable infrastructure [19], [21]

In a study assessing the feasibility of pultruded FRP profiles in lattice towers for electricity transmission, similar advantages over steel were confirmed. FRP structures were found to be lightweight, corrosion-resistant, and easy to transport and assemble, offering a cost-effective alternative in areas with limited accessibility or corrosive environmental conditions. However, the research also highlighted several important design limitations. FRP members have a lower elastic modulus than steel, which leads to greater deflection under service loads. This makes serviceability criteria—such as displacement and vibration control—more challenging to satisfy in FRP-based towers. Furthermore, the long-term behaviour of FRP, including creep, must be considered during the design phase to ensure structural integrity over time. A critical design concern also lies in the connections between FRP elements, as the anisotropic and brittle nature of composites makes them sensitive to stress concentrations. Both bolted and bonded joints require careful detailing to ensure reliable load transfer and to avoid premature failure [65].

These issues are similarly evident in studies focused on FRP cross arms as replacements for steel in transmission towers. FRPs provide exceptional corrosion resistance and lower maintenance demands, with a high stiffness-to-weight ratio that enables the design of lighter elements for remote or constrained locations. Nonetheless, their increased deformability and brittle failure modes—due to their lower stiffness—mean that serviceability performance, particularly deflection and vibration, remains a key design constraint. This reinforces the need for careful structural detailing and performance-based assessments when substituting steel with FRP in both tower structures and their components [66].

A comparative summary of the main characteristics of FRP and structural steel is presented in Table 2.1, highlighting the key differences in terms of mechanical performance, durability, installation, and lifecycle costs.

**Table 2. 1:** Comparison between FRP and Steel in Structural Applications

Property	FRP (e.g. GFRP)	Steel
Weight	~40-80 % lighter	Heavy
Strength-to-weight ratio	High tensile strength	Very high tensile and compressive strength
Compressive stiffness	Lower stiffness	High stiffness
Corrosion resistance	Excellent; intrinsic resistivity	Requires coatings or galvanization
Maintenance	Minimal over lifespan	Frequent for anti-corrosion
Electrical and thermal conductivity	Very low (insulating)	Conductive; high thermal conductivity
Lifecycle cost	~52 % lower when full-service life considered	Higher lifecycle cost due to maintenance
Environmental impact	Lower CO <sub>2</sub> emissions	Higher emissions from production
Installation & logistics	Prefabricated, quicker & easier	Requires heavy equipment, more labour
Design flexibility	Easily tailored to shape and size	Less flexibility, heavier manufacture

## 2.5. Structural Behaviour of FRP Towers

### 2.5.1. Wind-Induced Dynamic Response

A 60 m square GFRP telecommunication tower was numerically analysed under wind loading to evaluate its dynamic structural behaviour. The tower was considered clamped base supports and rigidly connected joints. The results highlighted the inherently high flexibility of GFRP structures, leading to excessive displacements at the top of the tower. To address this, a passive mass attenuator was proposed to reduce tip deformation. The study emphasized the importance of considering dynamic effects and vibration control in the design of composite towers. Due to the low stiffness of GFRP materials, flexible structures like these may require additional damping systems to improve serviceability and extend their operational lifespan by limiting cyclic movements and fatigue accumulation [67].

### 2.5.2. Failure Mechanisms and Buckling Behaviour

Beyond dynamic considerations, the structural integrity of GFRP towers under compressive loading and real operational conditions has also been experimentally assessed. A full-scale 24 m GFRP telecommunication tower, built with pultruded square hollow profiles in a triangular layout, was tested under gradually applied axial loads to investigate failure behaviour. The initial failure was attributed to a combination of local buckling and torsional deformation in the leg members, particularly near the joints (See Figure 2.15). This response highlighted the necessity of accounting for compression-specific

behaviour in GFRP elements, which differ from their tensile capacity due to the material's anisotropy. To enhance structural performance, a second configuration incorporating secondary bracing was implemented. This modification altered the failure mode to crushing near the joints and demonstrated that at least two bolts are required in the bracing connections to effectively restrain leg deformation. The study underscores the importance of detailed joint design and local buckling verification in composite tower structures, complementing earlier findings on their global dynamic behaviour [68].



**Figure 2. 15:** Local buckling of GFRP profiles, adapted from [68].

### 2.5.3. Long-Term Performance and Creep Effects

Creep is a time-dependent plastic deformation that occurs when a material is subjected to sustained loading over an extended period, particularly under constant stress and elevated temperatures [66], [69]. In composite structures, such prolonged loading can lead to an increase in deformation over time, a phenomenon known as creep. Although composite materials are widely recognized for their high strength-to-weight ratio, numerous studies have highlighted their vulnerability to long-term failure mechanisms such as creep, buckling, and environmental degradation due to humidity and temperature fluctuations [66]. These factors can compromise the structural integrity and reliability of composite systems, ultimately reducing their service life.

One of the key challenges in the application of GFRP pultruded profiles is the evaluation of long-term strain accumulation and creep deformation. Studies have shown that after 30 years of service, the stiffness of GFRP elements can decrease significantly, and creep-induced deflections can increase by up to 50% [70], [71]. However, in specific cases such as a GFRP transmission cross-arm analysed under operational loading, only minor creep displacements were observed—even under high stress levels—suggesting that creep can be manageable with proper structural design [71].

Due to the inherent viscoelasticity of polymer matrices, composite materials are susceptible to creep, especially under long-term loading. This limits their use in applications where strict deflection control is required. Experimental studies indicate that creep strains increase with both applied stress and ambient temperature. Elevated temperatures accelerate the creep response, while higher loads amplify strain accumulation. Furthermore, pultruded GFRP profiles exhibit lower creep under tensile loading and more significant deformation under flexural loading—primarily because the polymer matrix, which governs out-of-plane behaviour, influences the mechanical response in bending. When loading is aligned with the fibre direction, creep deformation is notably reduced. Despite these challenges, GFRP pultruded profiles remain viable for infrastructure applications, provided that stresses are properly controlled, temperature exposure is limited, and the design appropriately accounts for long-term creep behaviour [71].

## 2.6. Manufacturing

### 2.6.1. Filament Winding

Filament winding is an automated composite manufacturing process used to produce high-strength, lightweight structural components by winding continuous fibre tows—such as glass, carbon, or aramid—around a rotating mandrel in precise patterns (See Figure 2.16). These fibres can be impregnated with resin during the winding process (wet winding) or pre-impregnated (dry winding) and are applied under controlled tension to ensure optimal fibre alignment, minimal voids, and consistent quality. Curing of the resin typically occurs in heated dies, ovens, or autoclaves, depending on the resin system used—commonly epoxy or polyester.

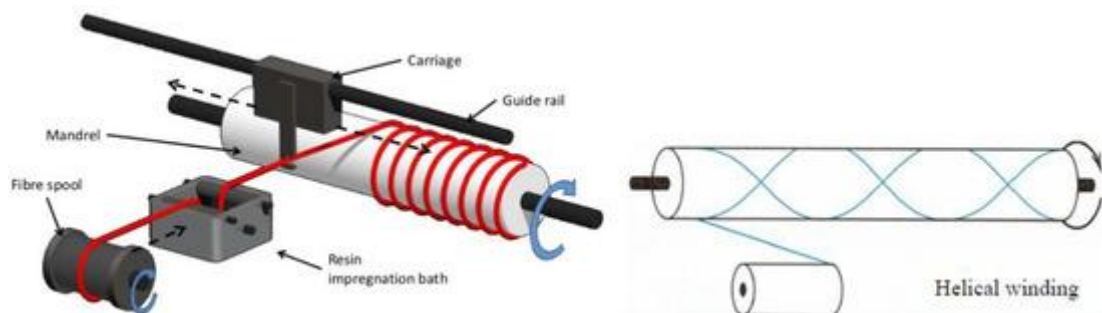


**Figure 2. 16:** Filament winding, reproduced from [72]

The mandrel may be metallic, collapsible, or inflatable, depending on the final geometry and extraction method. Filament winding supports a variety of winding angles (e.g., helical, hoop), enabling the designer to tailor the mechanical properties (axial, circumferential, torsional) to the structural load requirements. It is widely used in the production of tubes, tanks, pipes, and pressure vessels due to its high fibre content,

low material waste, and scalability. However, the process requires precise control and programming to ensure repeatability and accuracy in fibre placement [35].

Beyond conventional applications, filament winding has also enabled the development of advanced lattice truss structures, especially for aerospace and high-performance civil engineering components. An example is the anisogrid composite lattice developed for aerospace applications, characterized by openwork geometries where stiffness is directionally optimized to match load paths. This architecture eliminates many of the joints present in traditional lattice structures, enhancing both structural integrity and manufacturing efficiency. Filament winding is the preferred method for producing these anisogrid systems, due to its ability to create continuous fibre paths across complex geometries with minimal interruption [30].

A particularly notable innovation is the WrapToR truss, illustrated in Figure 2.17, a fully wound composite structure that uses continuous fibres to form truss members—especially chords and diagonals—without mechanical joints. This approach results in lightweight, joint-free structures with significantly increased stiffness and strength. Experimental results have demonstrated that WrapToR trusses outperform equivalent-mass sandwich panels in structural efficiency and can be manufactured using scalable, automated winding processes [24], [25], [73]. Further developments in ultra-efficient wound trusses have shown stiffness improvements up to 10 times greater than traditional pultruded tubes, highlighting the transformative potential of filament winding for truss-based applications in both aerospace and civil infrastructure [61].

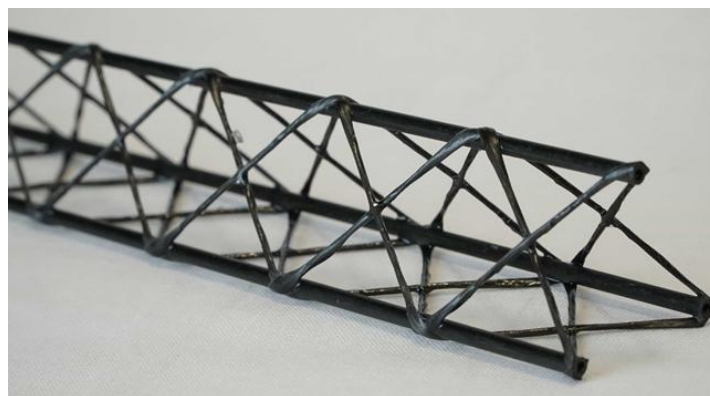


**Figure 2. 17:** WrapToR Truss, reproduced from [52]

### 2.6.2. Pultrusion

Pultrusion is a continuous, automated manufacturing process widely used to produce FRP structural elements with consistent quality and repeatable mechanical properties. The process involves aligning

continuous fibre reinforcements—typically glass, carbon, or aramid—and pulling them through a resin bath to ensure full impregnation. The wetted fibres are then drawn through a heated die, where the thermosetting resin cures, forming a rigid, dimensionally stable composite profile, as presented in Figure 2.18. The resulting elements can be fabricated in virtually unlimited lengths with uniform cross-sections, making the method ideal for high-volume production at relatively low cost [34].

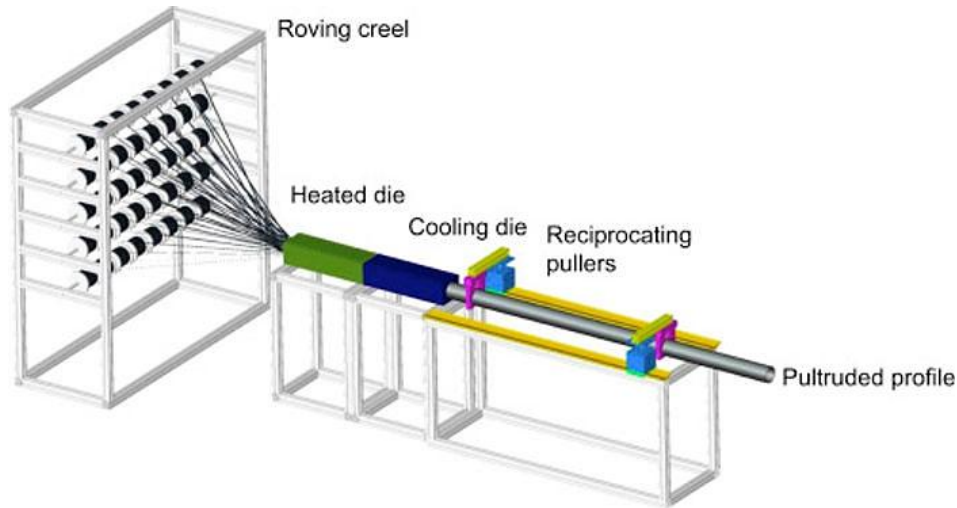


**Figure 2. 18:** Pultrusion process, reproduced from [74]

One of the key characteristics of pultrusion is the unidirectional alignment of fibres along the profile axis, which provides excellent longitudinal strength and stiffness. Common resins used include polyester, vinyl ester, and epoxy, depending on the mechanical and environmental performance requirements. Curing usually takes place within the die, although some systems incorporate post-curing using tunnel ovens to complete the polymerization process. The process supports a wide range of cross-sectional geometries—including I-beams, angles, tubes, channels, and custom profiles—allowing for versatility in structural design [35].

In civil engineering applications, pultruded FRP profiles are among the most commonly used composite products due to their durability, dimensional stability, and cost-effectiveness. Initially employed in industrial and chemical plant structures, their use has expanded to include pedestrian bridges, buildings, and transmission towers. However, one of the key challenges in their application remains the design of effective connections, particularly due to the anisotropic mechanical behaviour and brittle failure modes of the material [14], [75].

In the field of telecommunication towers, pultruded GFRP sections have been adopted in self-supporting lattice tower configurations, offering benefits such as mass production capability, uniform mechanical properties, and corrosion resistance [68]. Despite these advantages, the structural performance and

durability of joints—especially bonded or mechanically fastened connections—remain critical issues requiring careful consideration in design.

A notable example of pultrusion in tower construction is the Torre Rovira in Valencia, Spain—the tallest known tower built entirely from pultruded FRP elements (See Figure 2.19). Standing 44 meters high, the structure features a dodecagonal base transitioning into a hexagonal cross-section and is composed of GFRP struts manufactured using vinyl ester-based pultrusion. This project demonstrates the architectural and structural potential of pultruded composites in slender, tall civil structures [76].



**Figure 2. 19:** Composite tower – Valencia, reproduced from [76]

### *2.6.3. Joining techniques*

Effective joining methods are critical in ensuring the structural integrity and performance of FRP composite trusses and towers. Due to the anisotropic and brittle nature of composite materials, traditional steel joining methods like bolting often lead to premature failures, while bonded joints present challenges related to durability and installation. The three main joining strategies are bolted, bonded, and hybrid joints.

#### **Bolted Joints**

Bolted joints are a widely used mechanical fastening method in which a bolt is inserted through aligned holes in the components to be joined and secured with a nut [77], as illustrated in Figure 2.20. Bolted connections are commonly used due to their simplicity, ease of assembly, and compatibility with on-site

construction. However, several studies have shown that bolted joints significantly reduce the mechanical performance of FRP profiles. The primary failure mechanisms include fibre tearing, delamination, shear-out, and bearing failure due to stress concentration around the drilled holes [19], [23], [30], [60], [78], [79].

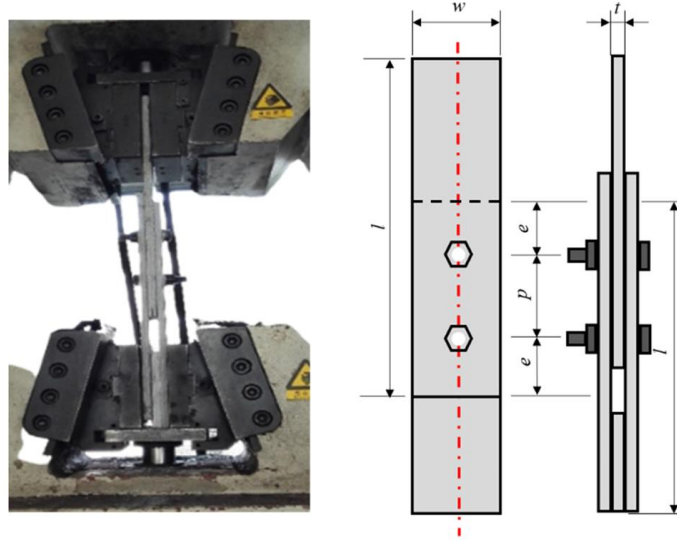


**Figure 2. 20:** Bolted connection, adapted from [20]

These joints reduce the load-bearing capacity of composites because they cannot transfer loads efficiently, often resulting in failure near the bolt hole [30]. This was corroborated in a study of GFRP cross-arms, which observed fibre tearing and delamination around bolt zones, proposing an increase in edge distance and thickness to mitigate these effects [78].

In structural frames, such as the GFRP space frame tested under fatigue conditions, bolted connections combined with steel gusset plates sustained two million load cycles without delamination [23]. Nevertheless, localized failures still emerged in other cases, highlighting variability in performance depending on joint detailing and load conditions.

A recommended design criterion is to ensure a minimum joint length equal to one-tenth ( $1/10$ ) of the length of the connected member, in order to allow full development of axial forces and prevent premature failure [17].

### **Bonded Joints**

Bonded joints, rely on structural adhesives that transfer the loads across the interface, making them an alternative that avoids the need to drill holes—preserving fibre continuity and minimizing stress concentrations (See Figure 2.21). These joints can offer higher fatigue resistance, better sealing (reducing moisture ingress), and distribute stresses more uniformly [14], [23], [79], [80].

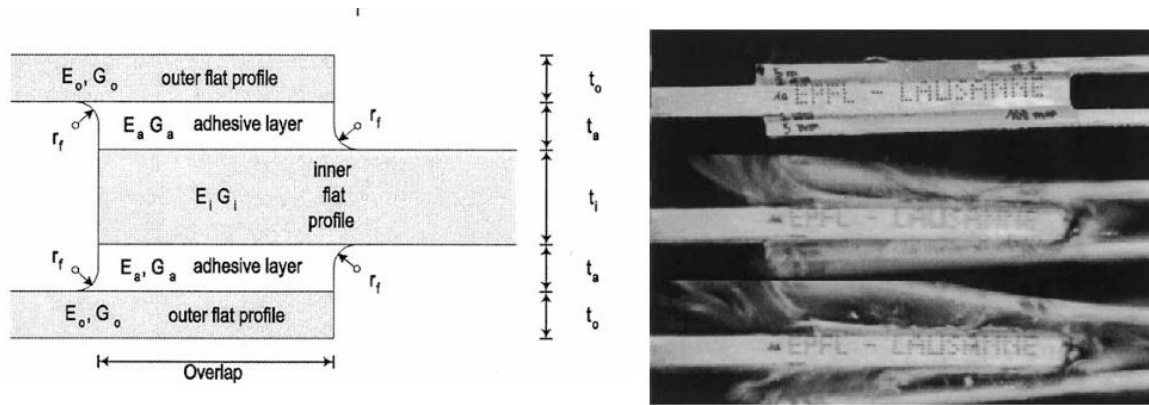


**Figure 2. 21:** Bonded connection and its failure mode, reproduced from [14]

The ideal failure mode in bonded joints is cohesive failure within the adherent (the GFRP itself), rather than failure in the adhesive or at the adhesive–adherent interface [14], [23]. However, poor surface preparation or geometric mismatch can result in interfacial failure or peeling stresses, which can propagate cracks and cause delamination.

Bonded lap joints between pultruded profiles may suffer from crack initiation in the adherent, followed by interlaminar shear failure [14]. Unlike the aerospace or automotive sectors, civil applications face additional constraints due to the specific geometry of pultruded profiles and the need for extended service life.

A key drawback of bonded joints is their sensitivity to environmental factors, including humidity and temperature, which influence adhesive curing and long-term behaviour. Appropriate surface treatment and curing protocols are essential, although durability under creep and fatigue still requires further investigation [23], [80].

### Hybrid Joints

To leverage the strengths of both techniques, hybrid joints combining bolts and adhesives have been proposed. These systems aim to mitigate the brittleness of purely bolted connections and the long-term uncertainty of adhesives [20], [79], [81].

The integration of internal gusset plates within GFRP truss joints has shown to significantly improve stiffness and shear resistance [20]. The combined use of bolts and adhesives enhances ductility, delays crack initiation, and improves load-sharing among components.

Hybrid joints used in space frame applications were able to withstand dynamic loading with minimal performance degradation [81]. In other studies, bonded joints supplemented with bolts achieved higher tensile resistance and enhanced redundancy [79].

A particularly promising hybrid solution is the pre-tightened tooth-based joint system, illustrated in Figure 2.22. This connection employs a steel sleeve with internal teeth inserted into a GFRP tube machined with matching teeth. Radial pressure is applied through high-strength bolts to achieve a tight mechanical interlock, enabling axial load transfer through shear along the interface without drilling through the GFRP tube [22].

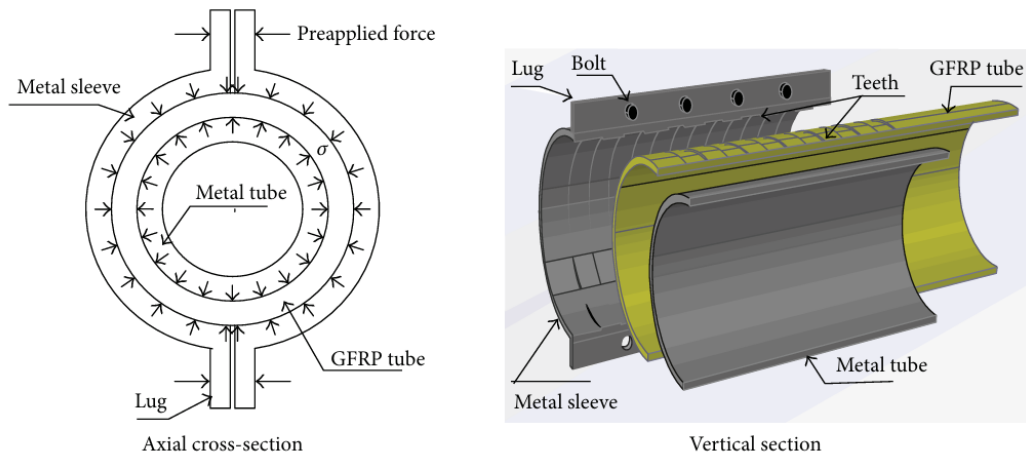


**Figure 2. 22:** Bonded connection and its failure mode, reproduced from [14]

The system demonstrated long-term stability, with no slippage or creep observed under sustained loads. It also provided improved interlaminar shear strength and effectively preserved the mechanical integrity of the composite material [22]. Based on these results, this pre-tightened hybrid joint has been selected as the preferred connection method for the FRP truss system proposed in this thesis, as it overcomes key limitations of traditional joints while ensuring high performance and durability.

### Challenges of joining FRP profiles

Although GFRP offers excellent mechanical properties, joining remains one of the main structural challenges. Bolted joints are easy to install but prone to damaging the composite material, while bonded joints offer mechanical and fatigue benefits but suffer from environmental sensitivity and require careful quality control. Hybrid systems provide a promising compromise, yet they are still being optimized for large-scale civil engineering applications.

Studies suggest the following best practices:

- Use closed profiles (e.g., tubes) instead of open I-beams to improve joint stiffness and reduce local failures [23], [82].
- Avoid drilling wherever possible to prevent fibre damage; if needed, increase edge distance and thickness [78]

- Control temperature and humidity during adhesive bonding to prevent long-term degradation [14], [80]
- Consider pre-tightened mechanical systems (e.g., toothed inserts) to improve interlaminar strength without drilling [22].

## 2.7. Design Actions and Verification Criteria

Several actions influence the structural behaviour of telecommunication towers, including permanent self-weight, wind actions, and frost actions. These actions, along with their combinations, were established according to relevant European standards and technical specifications, which have been adopted in this study. The selected standards provided the basis for calculating permanent and variable loads—such as dead load, wind pressure, and frost actions—as well as for defining load combinations and applying guidelines specific to FRP design.

The following standards and documents were used:

- **CEN/TS 19101** – *Design of Fibre-Polymer Composite Structures*
- **EN 1991-1-4** – *Eurocode 1: Actions on Structures – Wind Actions*
- **EN 1993-3-1** – *Eurocode 3: Towers, Masts, and Chimneys – Towers and Masts*
- **French National Annexes** to EN 1991-1-4 and EN 1993-3-1

### 2.7.1. Permanent Actions – Dead Load

Dead load refers to the permanent action resulting from the effect of gravity on the structure. For telecommunication towers, it includes the self-weight of the structural members as well as the weight of permanently installed equipment such as antennas, ladders, cables, and lighting systems. The dead load is typically calculated from the density of the materials and the dimensions of the components, while the weight of secondary equipment is often obtained directly from manufacturer or supplier specifications [46], [83].

### 2.7.2. Wind Actions

Wind loads are often the governing design action for telecommunication towers, as high wind speeds or extreme events such as hurricanes can cause significant structural damage, potentially leading to failure

[83]. The calculation of wind actions is prescribed by design standards and define procedures for determining wind pressures and their application to the structure.

The standards are based on simplified design methods, the overall wind load is sometimes obtained by summing the forces calculated separately for the tower and for the antennas, without considering aerodynamic interaction. Neglecting the shielding effect—where one component reduces the wind exposure of another—typically leads to conservative results, as the potential reduction in drag is omitted [83], [84].

Wind loads should be evaluated not only normal to the tower face but also for other incidence angles, depending on the tower geometry. The magnitude of the wind pressure is determined from the shape and size of the structural members and is applied as an equivalent pressure on the relevant reference areas. In general, three components of wind pressure are considered:

1. Peak velocity pressure,
2. Mean wind pressure, and
3. Gust-effect pressure.

The magnitude of the resulting wind pressure is influenced by multiple parameters, including the force coefficient ( $c_f$ ), structural factor ( $c_{scd}$ ), reference area ( $A_f$ ), wind turbulence intensity ( $I_v$ ), terrain roughness, orography coefficient ( $c_0$ ), and the reference height of the tower section [4]. Additional influences include air density, wind speed and direction, site altitude, and the overall structural geometry, all of which can significantly affect the intensity of wind actions [85].

### *2.7.3. Ice/Frost Actions*

Frost action refers to the accumulation of rain, freezing rain, or atmospheric moisture that solidifies on the structural elements, increasing both their effective cross-sectional dimensions and their mass. The enlargement of member profiles increases the wind-exposed surface area, thereby amplifying wind-induced forces, while the added ice weight increases the permanent load on the structure [83]. Design guidance for atmospheric icing is provided in EN 1993-3-1 Annex C, which classify ice types, based on their density and adhesion properties. This document or the National Annex also provide typical thicknesses and densities for use in design calculations.

#### *2.7.4. Operational Actions*

Operational loads refer to the variable forces and pressures that occur during the normal functioning and maintenance of a structure. In the context of telecommunication towers, these include the weight of maintenance personnel, equipment carried on platforms, and temporary tools. They are typically modelled as uniformly distributed or linear loads and differ from permanent actions like self-weight. Operational loads ensure the structure is safe and serviceable under routine use conditions [86].

#### *2.7.5. Ultimate Limit State (ULS)*

According to EN 1990:2002, ULS refers to conditions where the safety of people or the structure is at risk, including scenarios such as loss of equilibrium, excessive deformation leading to instability, rupture, fatigue, or other time-dependent effects. For telecommunication towers, the ULS represents the structural capacity of members and connections to resist critical load combinations that include factored actions. In steel design, verification often involves checking equivalent stresses, such as the von Mises criterion, under axial, shear, and bending conditions. In contrast, for fibre-reinforced polymer (FRP) towers—due to the anisotropic nature of the material—design checks should focus on axial stresses and force components in each principal direction, applying relevant FRP-specific criteria [83], [87].

#### *2.7.6. Serviceability Limit State (SLS)*

Per EN 1990:2002, SLS addresses the performance of the structure under normal service conditions, ensuring that functionality, user comfort, and appearance are maintained without excessive deflections, vibrations, or damage to non-structural elements. For telecommunication towers, the SLS is critical to guaranteeing proper antenna alignment and service performance under unfactored load combinations. This requires controlling tower deflections and rotations within allowable limits to prevent service degradation, especially in high-precision communication equipment [83], [87].

#### *2.7.7. Design Verification of Pultruded FRP Members*

In the design of pultruded FRP structural members, the maximum stress criterion is commonly adopted to ensure structural safety. This approach requires that the maximum stress in any principal material direction remains below the corresponding allowable strength of the material. The allowable strength is

obtained by dividing the characteristic strength by the appropriate partial safety factors and material factors and further reducing it using environmental reduction factors when relevant [88].

Due to the orthotropic behaviour of pultruded profiles, the verification must consider each principal direction separately—longitudinal and transverse—and distinguish between tension and compression, since the corresponding strengths differ. According to CEN/TS 19101:2022, the most unfavourable combination of axial, bending, and shear stresses acting in each principal direction must be compared against the adjusted allowable strength for that direction. Failure is deemed to occur when any single stress component exceeds its corresponding allowable limit [89].

In addition to stress checks, design verification requires ensuring that the design values of internal forces—axial force ( $N_d$ ), bending moment ( $M_d$ ), and shear force ( $V_d$ )—do not exceed their respective design resistances. These resistances are calculated from characteristic strengths, reduced by partial safety factors, material factors, and environmental reduction factors. Axial compression resistance must account for both global and local buckling phenomena; shear resistance must be verified in both the longitudinal–transverse and transverse–through-thickness planes; and bending resistance must be checked for both the major and minor principal axes [89].

## 3. METHODOLOGY

### 3.1. Introduction

This chapter begins by presenting the GAP analysis methodology used to identify the most suitable design approach, considering the initial constraint of similar stiffness between steel and FRP solutions. A pre-established 36-meter-high steel tower geometry was used as the reference model and compared against a version made from pultruded GFRP profiles, selected based on the outcomes of the GAP study. This comparative model retained the same geometry as the steel tower and was analysed using Finite Element Modelling (FEM) in Abaqus, with the only change being the substitution of material properties to those of GFRP.

Following this, two design loops were carried out. The first design loop maintained the original steel tower configuration, focusing on optimizing stiffness and weight using FRP materials. The second loop involved a complete redesign of the tower geometry to enhance structural stiffness and better exploit the anisotropic behaviour of FRP profiles. All models were assessed according to Serviceability Limit State (SLS) and Ultimate Limit State (ULS) criteria, including checks on maximum tip deflection, axial stress, and shear stress. Wind loads were determined based on Eurocode 1, Eurocode 3, and the relevant French National Annex.

### 3.2. Conceptual Design and Material Selection (GAP Methodology)

#### *3.2.1. Overview of the GAP Approach*

The GAP methodology provides a structured initial approach to addressing complex design problems. It is particularly useful for generating innovative solutions based on non-conventional materials such as Fibre Reinforced Polymers (FRP). When multiple design alternatives are available, the GAP methodology offers an effective framework for selecting an optimal starting point by considering a wide range of parameters, including geometry, structural architecture, and manufacturing processes. This approach is especially valuable when working with FRP materials, which offer greater flexibility in shaping and allow for the creation of structurally efficient yet manufacturable designs [90].

The methodology involves a comprehensive brainstorming phase to identify all feasible options, followed by a systematic comparison of these options against defined constraints—in the case of the composite

telecommunication tower, cost competitiveness and ease of fabrication. The outcome of the process is the identification of one or two promising design configurations, which are then further analysed to evaluate their mechanical performance and structural feasibility in fulfilling the intended functional requirements.

### *3.2.2. Design Alternatives Considered*

A wide range of composite joint configurations have been proposed and investigated to overcome the challenges associated with connecting FRP structural members. Table 3.1 presents a synthesis of various joint concepts compiled from the literature, categorized according to their mechanical behaviour and construction strategy.

The top-left configuration illustrates the classical bolted connection, widely used due to its simplicity, modularity, and ease of on-site assembly. However, as discussed earlier in Section 2.6.3, this joint type often leads to premature failures in composite members, including fibre tearing, delamination, and shear-out due to stress concentrations around the drilled holes.

The top-right image shows a bonded joint, where structural adhesives are used to connect the profiles without mechanical fasteners. This preserves fibre continuity and eliminates drilling but introduces concerns about durability, moisture resistance, and long-term creep behaviour, especially under temperature and humidity fluctuations.

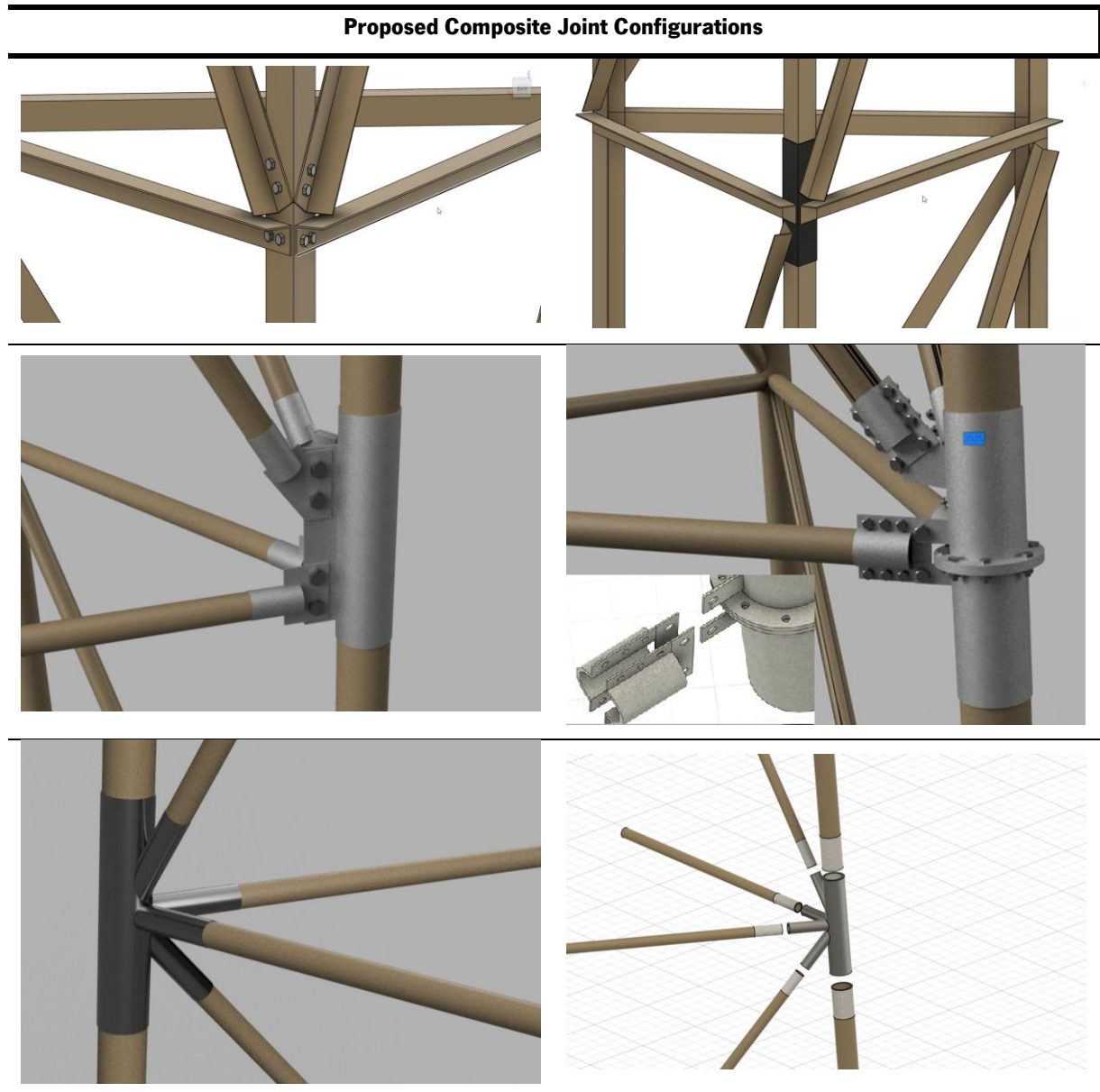
In the second row, left, a hybrid connection is presented. In this approach, each GFRP profile is first bonded to a metallic insert or node, and the metallic inserts are then connected using mechanical fasteners. This method shifts mechanical stress away from the composite-to-composite interface, improving structural performance by allowing the bolts to act exclusively on metallic components.

The second row right depicts the pre-tightened tooth-based joint developed by Liu et al. [22]. This system involves machining internal teeth on a steel sleeve and matching external teeth on the GFRP tube. High-strength bolts apply radial compression, producing tight mechanical interlocking without requiring through-holes. The connection successfully transfers axial forces via shear along the bonded interface and has shown exceptional performance under long-term loading, with no sliding or creep, making it a reliable and damage-tolerant solution for truss applications in infrastructure.

The bottom-left joint represents a more complex fully bonded system, where the GFRP profiles are adhesively connected to a central steel node without any mechanical fastening. This method aims to maximize stiffness and eliminate drilling, although it requires strict quality control and careful surface preparation to avoid premature cohesive or interfacial failures.

Lastly, the bottom-right joint shows a threaded insert connection, in which the FRP tubes are equipped with embedded metal threads that screw into an aluminium or steel connector. This concept of threaded connections increases joint stiffness and reduce deformation, offering a promising modular solution with simplified assembly and no need for adhesives or bolts [91]. Although still in development, this approach may be particularly useful in demountable or prefabricated FRP structures.

**Table 3. 1:** Proposed Composite Joint Configurations



### 3.2.3. GAP Results and Final Configuration Selection

Based on the insights gathered in the literature review, a comprehensive GAP Methodology analysis was developed to evaluate and compare various design strategies for composite telecommunication towers.

The results are summarized in Figure 3.1, which presents a decision-support framework that integrates three fundamental categories: Geometry, Architecture, and Process.

Under Geometry, aspects such as profile cross-sections, joint configurations, layup thickness, fibre volume fraction, resin properties, and ply orientations were explored. These parameters were essential in evaluating the feasibility of structural profiles like pultruded tubes, IsoTruss systems, and wrapped composites.

The Architecture section focused on structural configurations (e.g., lattice vs. sandwich structures), joint types (bolted, bonded, hybrid), load transfer mechanisms, and geometric constraints. It considered previous studies on nodal gusset plates, pre-tightened joints, and hybrid systems using steel inserts, helping identify structural layouts that improve stiffness, reduce stress concentrations, and facilitate modular construction.

The Process category evaluated manufacturing techniques such as pultrusion, filament winding, braiding, and robotic filament winding, as well as process parameters like curing temperatures, winding angles, and braiding densities. Pultruded profiles were selected for their competitive cost, repeatability, and availability, while filament winding was categorized as an optimum high-performance solution with higher initial manufacturing costs but enhanced load-bearing potential.

This GAP framework enabled a structured comparison of alternatives, supporting the selection of feasible combinations of material, geometry, joining methods, and manufacturing techniques for the design of FRP towers. Based on this analysis, pultruded profiles and pre-tightened connections were selected.

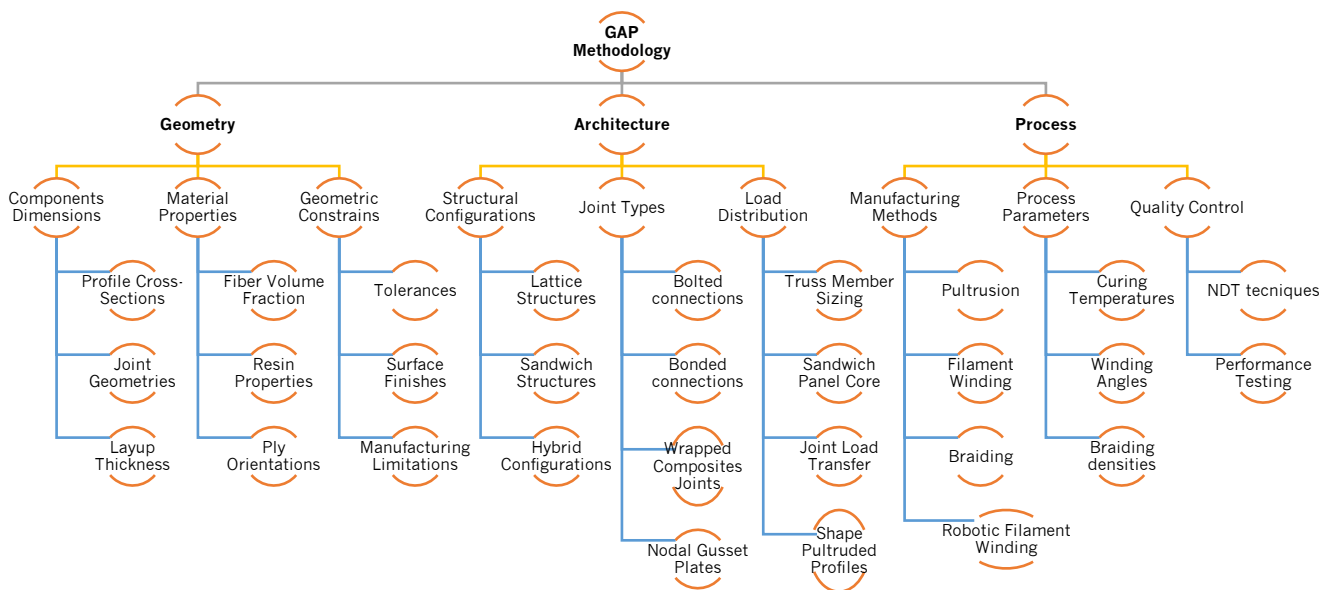


Figure 3. 1: Gap Methodology map

### 3.3. Load Definition

The load cases and combinations considered in the analysis of the telecommunication tower were defined in accordance with the relevant European standards and national annexes, namely EN 1990 (Basis of Structural Design), EN 1991-1-1 (Actions on structures – General actions), EN 1991-1-4 (Wind actions), EN 1993-3-1 (Towers, masts, and chimneys), and CEN/TS 19101 (Design of fibre-polymer composite structures). The loads account for both permanent actions and variable actions, ensuring compliance with serviceability and ultimate limit state requirements.

The following subsections describe in detail the determination of:

- Permanent actions (self-weight and permanent equipment)
- Wind actions
- Ice/frost actions
- Operational actions (platforms, guardrails, maintenance)

These loads form the basis for the finite element modelling and structural verification described in subsequent sections.

#### 3.3.1. Permanent actions

For both the reference steel tower and the GFRP pultruded profile towers, the densities adopted were  $7.85 \text{ g/cm}^3$  for structural steel S235 and  $1.80 \text{ g/cm}^3$  for GFRP. The dead load was calculated as the product of the profile volume ( $V$ ), material density ( $\rho$ ), and gravitational acceleration ( $g=9.81 \text{ m/s}^2$ ), as expressed in Eq. (3.1):

$$W = g \cdot \rho \cdot V \quad (3.1)$$

The total mass included not only the self-weight of the structural members but also the mass of the pylon equipment, which consists of the main ladder, cable tray supports, rail lifeline, lightning rod and its support, antenna supports, working platforms, and resting levels. Additionally, the masses of the cable tray and antennas were determined separately. The combined additional mass was later incorporated into the finite element model, as shown in Eq. (3.2):

$$\text{Additional mass} = \text{Tower equipment} + \text{Antennas mass} + \text{Cable tray mass} \quad (3.2)$$

#### 3.3.2. Wind Actions on Structure and Equipment

Wind actions were calculated separately for three categories:

1. Structure with linear equipment – including ladders, cable trays, and similar components.
2. Point equipment – including lightning rods, antenna supports, working ladders, and bay frames.
3. Antennas – considered as discrete aerodynamic elements.

For each category, three wind force types were determined in accordance with EN 1991-1-4 and EN 1993-3-1, the total wind force, mean wind force, and gust wind force.

These calculations were performed for two scenarios:

- Without frost – using the bare projected areas.
- With frost – where the projected areas were increased according to the frost thickness defined in the National Annex.

In all cases, the greatest of the three force types was taken as the governing wind action, in accordance with Eurocode provisions.

### Fundamental basic wind velocity

The mean wind velocity is defined as the average over a 10-minute period, with a 2 % probability of exceedance, corresponding to a 50-year return period. It is determined independently of wind direction and referenced at a height of 10 m above ground level, with terrain factors applied where relevant [84]. Here,  $v_{b,0}$  represents the fundamental value of the basic wind velocity, obtained from the National Annex as 26 m/s, by selecting Region 3 according to the French National Annex, as shown in Figure 3.2.

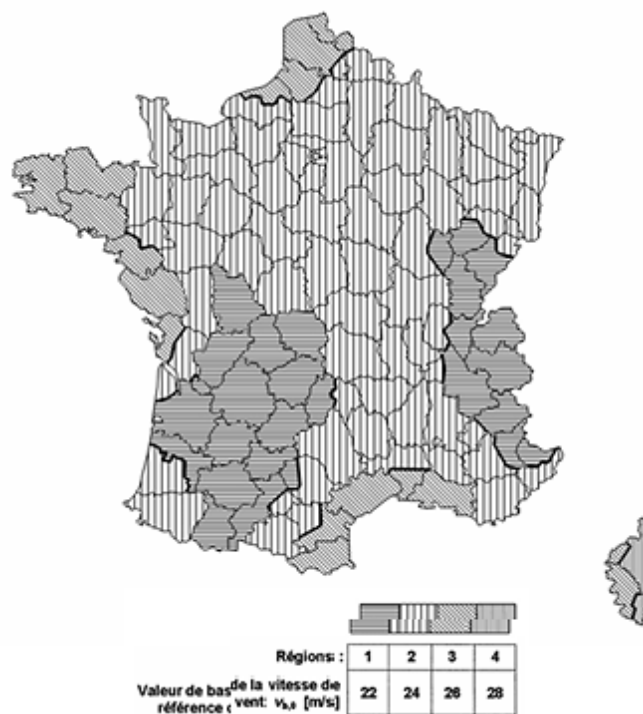


**Figure 3. 2:** Fundamental basic wind velocity map, obtained from [92]

### Basic wind velocity

The basic wind velocity is obtained by adjusting the fundamental value to account for the wind direction factor ( $c_{dir}$ ) and the season factor ( $c_{season}$ ), as defined in Eq. (3.3). For the present calculations, both  $c_{dir}$  and  $c_{season}$  were taken as 1.

$$V_b = C_{dir} \cdot C_{season} \cdot V_{b,0} \quad (3.3)$$

### Mean wind

The mean wind velocity is determined using the roughness factor  $c_r(z)$  and the orography coefficient  $c_0(z)$ , as specified in the National Annex. The mean wind velocity was calculated according to Eq. (3.4):

$$V_m = C_r(z) \cdot C_0(z) \cdot V_b \quad (3.4)$$

The roughness factor  $c_r(z)$  is determined from Eq. (3.5) according to the height  $z$ .

$$\begin{cases} C_r(z) = k_r \cdot \ln\left(\frac{z}{z_0}\right) & \text{for } z_{min} \leq z \leq z_{max} \\ C_r(z) = C_r \cdot (z_{min}) & \text{for } z \leq z_{min} \end{cases} \quad (3.5)$$

The terrain factor  $k_r$  is given by Eq. (3.6):

$$k_r = 0.19 \cdot \left(\frac{z_0}{z_{0,II}}\right)^{0.07} \quad (3.6)$$

Terrain Category II was adopted, corresponding to areas with low vegetation such as grass and isolated obstacles spaced at least 20 obstacle heights apart, with  $z_0$  of 0.05 meters and minimum height ( $z_{min}$ ) of 2 meters and maximum height ( $z_{max}$ ) of 200 meters.

### Turbulence Intensity

The turbulence intensity  $I_v(z)$  is defined in terms of the standard deviation of turbulence,  $\sigma_v$ , as shown in Eq. (3.7):

$$\sigma_v = k_r \cdot v_b \cdot k_l \quad (3.7)$$

Where  $k_r$  is the terrain factor and  $k_l$  is the turbulence factor. In this study,  $k_l$  was taken as 1. The turbulence intensity, which also depends on the orography coefficient  $c_0(z)$ , is then calculated using Eq. (3.8):

$$\begin{cases} I_v(z) = \frac{k_l}{c_0(z) \cdot \ln(z/z_0)} & \text{for } z_{min} \leq z \leq z_{max} \\ I_v(z) = I_v(z_{min}) & \text{for } z < z_{min} \end{cases} \quad (3.8)$$

### Peak velocity pressure

The peak velocity pressure was calculated for each tower section at 6 m intervals, in accordance with , which accounts for short-term velocity fluctuations. It is given by Eq. (3.9), where  $\rho$  is the air density, taken from the National Annex as 1.225 kg/m<sup>3</sup>.

$$q_p(z) = [1 + 7 \cdot I_v(z)] \cdot \frac{1}{2} \rho v_m^2(z) \quad (3.9)$$

### Structural factor ( $c_{scd}$ )

The structural factor was determined in accordance with Section 6 of EN 1991-1-4 [84], which defines it as the product of the size factor  $c_s$  and the dynamic factor  $c_d$ .

The size factor  $c_s$ , given by Eq. (3.10), accounts for the reduction in wind effects due to the non-simultaneity of peak pressures:

$$c_s = \frac{1 + 7 \cdot I_v(z_s) \cdot \sqrt{B^2}}{1 + 7 \cdot I_v(z_s)} \quad (3.10)$$

The dynamic factor  $c_d$ , expressed in Eq. (3.11), accounts for the increased wind effects due to turbulence-induced resonance:

$$c_d = \frac{1 + 2 \cdot k_p \cdot I_v(z_s) \cdot \sqrt{B^2 + R^2}}{1 + 7 \cdot I_v(z_s) \cdot \sqrt{B^2}} \quad (3.11)$$

Here,  $k_p$  is the peak factor,  $B^2$  is the background factor (correlation between pressure and surface), and  $R^2$  is the resonance response factor.

### Total force coefficient ( $\sum c_f$ )

The total force coefficient was obtained as the sum of the bare structure coefficient  $c_{f,s}$  and the linear equipment coefficient  $c_{f,A}$ , as shown in Eq. (3.12):

$$\sum c_f = c_{f,s} + c_{f,A} \quad (3.12)$$

The coefficient  $c_{f,s}$  is defined in Eq. (3.13) as:

$$c_{f,s} = K_\theta \cdot c_{f,s,0} \cdot \frac{A_s}{\sum A} \quad (3.13)$$

The geometry-dependent factor  $K_\theta$  is calculated differently for triangular and square towers:

- Triangular towers, Eq. (3.14):

$$K_\theta = \frac{A_c + A_{c,sup}}{A_s} + \frac{A_f}{A_s} (1 - 0.1 \sin^2 1.5\theta) \quad (3.14)$$

- Square towers, Eq. (3.15):

$$K_{\theta} = 1 + K_1 K_2 \sin^2 2\theta \quad (3.15)$$

In Eqs. (3.14)–(3.15),  $K_{\theta}$  is a geometry-dependent factor (triangular or square towers).  $A_f$  denotes the total projected area, normal to the wind, of sharp-edged members of the considered face;  $A_c$  is the total projected area of circular members in subcritical flow, and  $A_{c,sup}$  the corresponding area in supercritical flow;  $A_s$  is the total projected area of all elements of the face. The wind-incidence angle is  $\theta$ , and  $\phi$  is the filling (solidity) ratio, i.e., the ratio of the summed projected area of the elements in the face to the reference face area  $A_{ref}$ .

The flow regime is identified via the Reynolds number: subcritical for  $Re < 4 \times 10^5$  and supercritical for  $Re \geq 4 \times 10^5$ . All projected areas  $A_f$ ,  $A_c$ ,  $A_{c,sup}$ ,  $A_s$ , and  $A_{ref}$  were recalculated for frost conditions per the National Annex.

For wind acting perpendicular to a face, the overall force coefficient  $c_{f,S,0,j}$  for section  $j$  of a square or equilateral triangular cross-section, composed of both circular and sharp-edged members, is calculated as shown in Eq. (3.16).

$$c_{f,S,0,j} = c_{f,0,f} \cdot \frac{A_f}{A_s} + c_{f,0,c} \frac{A_c}{A_s} + c_{f,0,c,sup} \frac{A_{c,sup}}{A_s} \quad (3.16)$$

The individual terms of Eq. (3.16) are defined in Eqs. (3.17)–(3.19) where  $C_1$  is equal to 2.25 for square towers and 1.90 for triangular towers, and  $C_2$  is 1.50 for square towers and 1.40 for triangular towers.

$$c_{f,0,f} = 1.76C_1[1 - C_2\phi + \phi^2] \quad (3.17)$$

$$c_{f,0,c} = C_1(1 - C_2\phi) + (C_1 + 0.875)\phi^2 \quad (3.18)$$

$$c_{f,0,c,sup} = 1.9 - \sqrt{(1 - \phi)(2.8 - 1.14C_1 + \phi)} \quad (3.19)$$

Finally, the linear equipment coefficient  $c_{f,A}$  (e.g., for waveguides, power cables) is calculated using Eq. (3.20), where  $c_{f,A,0}$  is obtained from Table B.2.1 of EN 1991-1-4,  $K_A$  is the positional reduction factor (taken as 0.8 in this study),  $\psi$  is the angle of wind incidence, and  $A_A$  is the projected area of the equipment.

$$c_{f,A} = K_A \cdot c_{f,A,0} \cdot \sin^2 \psi \cdot \frac{A_A}{\sum A} \quad (3.20)$$

### Calculation of wind actions – equivalent static method

For the calculation of wind actions, the equivalent static method was applied. In this approach, the tower was divided into sections with identical panels. When determining the projected area of each section, the

contribution of truss members located in faces parallel to the wind direction, as well as horizontal or corner bracing, is excluded, in accordance with EN 1991-1-4, Section 5.3(2).

For symmetrical lattice towers braced with frames, with or without equipment, the wind loads are first calculated following the procedure in Annex B.2 of EN 1993-3-1. The maximum values are then determined according to Annex B.3.2.2.1 to B.3.2.2.5 of the same standard. The reference area  $A_{ref}$  corresponds to the projected area of the members included in the section, taken in the direction of the wind. The total wind force for a section is given in Eq. (3.21).

$$F_w = c_s c_d \cdot \sum c_f \cdot q_p(z_e) \cdot A_{ref} \quad (3.21)$$

The mean wind load was calculated using Eq. (3.22):

$$F_{m,W(z)} = \frac{q_p}{1 + 7I_v(z_e)} \sum c_f A_{ref} \quad (3.22)$$

The gust wind load is given by Eq. (3.23):

$$F_{T,W(z)} = F_{m,W(z)} \left[ 1 + (1 + 0.2 \left( \frac{z_m}{h} \right)^2) \cdot \frac{[1 + 7I_v(z_e) c_s c_d - 1]}{c_0(z_m)} \right] \quad (3.23)$$

For each height (z), the governing wind action was taken as the maximum among Eqs. (3.21)–(3.23), for both frost and non-frost conditions.

### Considered wind directions

Wind directions were evaluated according to Figure 3.3, which specifies perpendicular and diagonal wind incidence for triangular and square section towers.

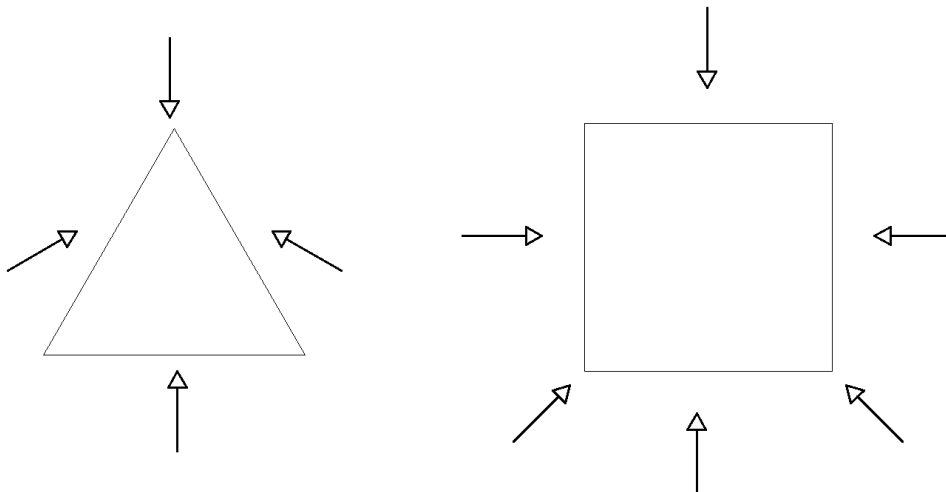


**Figure 3. 3:** Considered wind directions

### 3.3.3. Wind Actions on Antennas

The wind actions on antennas were calculated following the same methodology described in Section 3.3.2 – Wind Actions on Structure and Equipment, with adaptations to account for the specific installation heights and aerodynamic properties of the antennas. Parameters such as the basic wind velocity, mean wind velocity, and turbulence intensity were computed using the same formulations, but with reference heights corresponding to the antenna positions.

The calculation procedure considered the three wind force types defined in EN 1991-1-4 and EN 1993-3-1—total wind force, mean wind force, and gust wind force—with the governing wind action taken as the maximum of these three, for both frost and non-frost conditions.

The reduction coefficient  $K_A$  was taken as 1.0, and the drag coefficient  $c_{f,A,0}$  for point equipment was provided according to the applicable wind direction and speed. The general expression for the force coefficient of point equipment is given in Eq. (3.24):

$$c_{f,A} = K_A \cdot c_{f,A,0} \quad (3.24)$$

In compliance with the project requirements, the total projected antenna area was set to 24 m<sup>2</sup> distributed over the upper 12 meters of the tower as follows:

- 9.0 m<sup>2</sup> at 33 m height
- 9.0 m<sup>2</sup> at 27 m height
- 6.0 m<sup>2</sup> at 21 m height

These projected areas, along with the associated aerodynamic coefficients, were used in the calculation of the wind loads on antennas, ensuring consistency with the Eurocode provisions and the specific structural configuration of the tower.

### 3.3.4. Operational actions

The operational loads considered in the design include a uniformly distributed load of 2.0 kN/m<sup>2</sup> on the platform surface and a linear load of 0.5 kN/m on the horizontal guardrails. The diagram of the working platform is shown in Figure 3.4

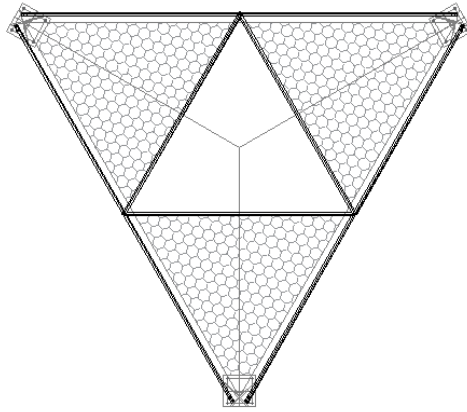


**Figure 3. 4:** Working platform

### 3.3.5. Ice Frost Actions

For the frost action, it was assumed that the structural profiles were covered with an ice layer of 40 mm thickness, as illustrated in Figure 3.5. The additional weight due to frost was calculated by multiplying the ice volume by the frost density specified in the National Annex, taken as 0.9 g/cm<sup>3</sup>.

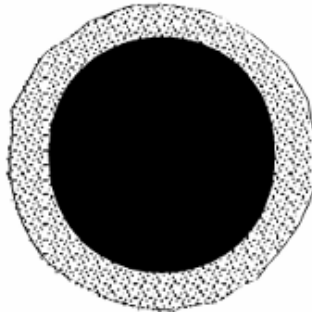


**Figure 3. 5:** Ice frost on the structural elements

### 3.3.6. Load Combinations

#### Ultimate Limit State (ULS)

According to EN 1990, the ULS combination for persistent or transient design situations is given by Eq. (3.25), where  $G_k$  is the characteristic value of permanent actions,  $Q_k$  is the characteristic value of variable actions,  $\gamma_G$  is the partial factor for permanent actions and  $\gamma_Q$  is the partial factor for variable actions.

$$ULS = \gamma_G \cdot G_k + \gamma_Q \cdot Q_k \quad (3.25)$$

The Ultimate Limit State (ULS) combinations of actions for pylons and guyed masts are determined in accordance with EN 1993-3-1, Table A.2, which specifies the partial factor values based on the reliability class of the structure.

The reliability class was taken as Class 2, corresponding to pylons located outside urban areas but not in uninhabited or rural open areas; which specifies that for unfavourable effects, the permanent actions must be multiplied by a factor of  $\gamma_G=1.10$  and the variable actions by  $\gamma_Q=1.40$ . For favourable effects, the factors are  $\gamma_G=1.00$  and  $\gamma_Q=0.00$ .

The combinations considered in this study include the presence or absence of frost, different wind directions ( $X+$ ,  $X-$ ,  $Y+$ ,  $Y-$ ), and both unfavourable and favourable scenarios for the vertical load effect in the Z-axis.

### Serviceability Limit State (SLS)

According to EN 1993-3-1 [93], serviceability criteria for telecommunication towers include controlling deflections, rotations, and vibrations that could impair the efficient use of the structure or the proper functioning of antennas and associated equipment. These criteria aim to prevent:

- Signal loss due to oscillations, out-of-plumb conditions, or excessive sway.
- Damage to non-structural components caused by deformations or deflections.

For composite structures, a partial material factor  $\gamma_M$  of 1.0, is recommended in serviceability checks; however, it should be noted that the mechanical properties of composites may vary due to environmental effects, which can influence long-term performance.

The maximum allowable deflections and rotations are evaluated at the top of the structure, using combinations of characteristic actions acting simultaneously on the structure and its equipment.

In this study, the SLS load combination was taken as shown in Eq. (3.26), where  $G_k$  is the permanent load,  $Q_{k,1}$  is the wind load (structure, linear equipment and antennas without frost), and  $Q_{k,2}$  is the operational load.

$$SLS = G_k + Q_{k,i} + 0.7 \cdot \sum_{i>1}^i Q_{k,i} \quad (3.26)$$

## 3.4. FRP Design Considerations

### 3.4.1. Design Value of Resistance

The design value of resistance of FRP pultruded profiles was obtained by reducing the characteristic resistance through partial and reduction factors that account for uncertainties and influencing effects.

These include:

- Model uncertainties, such as deviations in the resistance model or geometrical tolerances,
- Environmental effects, including temperature, moisture, and ageing,
- Material variability, accounting for deviations in the properties of the manufactured product.

The design resistance was derived from the characteristic resistance of the profile and is calculated using Eq. (3.27). In this expression:

- $\gamma_{Rd}$  is the partial factor for the resistance model, according to the considered failure mode,
- $\gamma_m$  is the partial material factor, accounting for deviations in the product's material properties, determined from the coefficient of variation of the material,
- $X_{k,i}$  is the characteristic value of the relevant material property,
- $\eta_{c,i}$  is the conversion factor for environmental effects,
- $a_d$  represents the design values of geometrical parameters, and
- $F_{Ed}$  is the design value of actions used to assess the design effect of actions.

$$R_d = \frac{1}{\gamma_{Rd} \cdot \gamma_m} R\{\eta_{c,i} \cdot X_{k,i}; a_d; \sum F_{Ed}\} \quad (3.27)$$

The resulting design resistance was then compared against the effects of actions for the Ultimate Limit State (ULS) verification.

### 3.4.2. Partial Factors for Materials ( $\gamma_m$ )

The partial material  $\gamma_m$  is related to the coefficient of variation of the product,  $V_x$ , which is determined through testing. The corresponding value of  $\gamma_m$  was taken from the Table 3.2.

**Table 3. 2:** Material partial factors

<b>V<sub>x</sub></b>	0.05	0.10	0.15	0.20	0.25	0.30	0.35	0.40	0.45
<b>γ<sub>m</sub></b>	1.07	1.15	1.23	1.32	1.41	1.51	1.61	1.71	1.82

The value of  $V_x$  depends on the number of available test results and was obtained from Eq. (3.28). For 1000 specimens,  $fV_x$  is taken as 1, according to the Table 4.2 of the FprCEN/TS 19101:2022 guideline. In the present study, a value of  $fV_x=1.70$  was used for five test specimens.

$$V_x = V_{x,exp} \cdot fV_x \quad (3.28)$$

3.4.3. Partial Factors for Resistance Models ( $\gamma_{Rd}$ )

The partial factor for resistance models,  $\gamma_{Rd}$ , is defined according to the governing failure mode of the profile or laminate. The recommended values from FprCEN/TS 19101:2022 are given below in Table 3.3 [89].

**Table 3. 3:** Resistance models partial factors ( $\gamma_{Rd}$ )

Material failure	Global buckling			Local buckling
	Flexural	Lateral-torsional	Flexural-torsional	
1.40	1.30	1.30	1.55	1.30

3.4.4. Conversion factor ( $\eta_c$ )

The overall conversion factor,  $\eta_c$ , is calculated as the product of the temperature effect conversion factor ( $\eta_{ct}$ ) and the moisture effect conversion factor ( $\eta_{cm}$ ), as expressed in Eq. (3.29):

$$\eta_c = \eta_{ct} \cdot \eta_{cm} \tag{3. 29}$$

The temperature effect conversion factor,  $\eta_{ct}$ , accounts for changes in material properties due to service temperature variations. For pultruded FRP profiles, Eurocode-based guidelines define the applicable range as  $-40^\circ\text{C} < T_s < T_g - 20^\circ\text{C}$ , where  $T_s$  is the service temperature and  $T_g$  is the glass transition temperature. In this study,  $\eta_{ct}$  was taken as 1.0.

The moisture effect conversion factor,  $\eta_{cm}$ , depends on the exposure class. For telecommunication towers, the adopted class was Exposure Class II—characterized by outdoor service conditions with exposure to water, UV radiation, and freeze–thaw cycles. For this exposure class, the recommended value is  $\eta_{cm}=0.85$ .

3.4.5. Long-term effects – Creep

The reduction in stiffness of FRP materials over time due to creep can be expressed by Eq. (3.30), where the initial mean modulus  $X_m(0)$  is reduced using the creep coefficient  $\varphi(t)$  to obtain the long-term modulus  $X(t)$ :

$$X(t) = \frac{X_m(0)}{1 + \varphi(t)} \tag{3. 30}$$

Creep effects, already discussed in the literature review (Section 2.5.3), are an essential consideration in FRP design because they can progressively reduce strength and increase deformations over the

structure’s service life. For deformations, serviceability criteria impose deflection limits, and stiffness is adjusted using the elastic modulus and shear modulus affected by the creep coefficient.

According to FprCEN/TS 19101:2022, creep coefficients are tabulated for  $t=50$  years under service temperatures  $\leq 25$  °C and relative humidity  $\leq 65\%$ . The values of the creep coefficient for pultruded composite profiles are:

- $E_{x,full}$  (full section modulus): 0.70
- $G_{xy,full}$  (shear modulus): 2.09

### 3.5. Finite Element Modelling in Abaqus

#### 3.5.1. Initial Geometry

The initial tower geometry was provided by Retis Solutions, based on an existing steel tower design. The structure has a total height of 36 m, divided into six sections of 6 m each. The base is triangular with a width of 4 m at ground level, tapering progressively to 2.4 m at a height of 24 m. From this point to the top, the cross-section remains constant from 24 m, as shown in Figure 3.6.

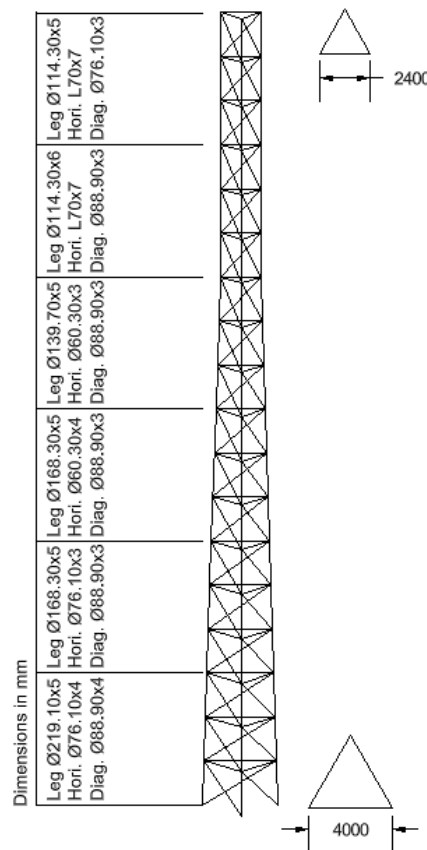


Figure 3. 6: Diagram of the tower geometry

Each 6 m section is subdivided into two 3 m subsections with a Z-diagonal bracing configuration, where only one diagonal brace is placed every 3 m. Two sides of the tower have diagonals oriented in the same direction, while the third side has them in the opposite direction.

The initial member cross-sections matched those of the reference steel design. Detailed section sizes are presented in Section 4 (First Design Loop).

### 3.5.2. FEM Setup

#### Element Type and Modelling Approach

The finite element analysis was performed using spatial beam elements; in Abaqus, these are defined as B31 elements (2-node linear beams in space). Each node has six degrees of freedom: three translational (U1, U2, U3) and three rotational (UR1, UR2, UR3). All member connections were modelled as fully rigid, representing the stiffness contribution of the proposed pre-tightened hybrid tooth-based sleeve joints, which ensure high mechanical interlock and negligible joint deformation under service and ultimate loads. This assumption reflects the expected behaviour based on the experimental performance of the joint system described in Section 3.2.2. Figure 3.7 (a) illustrates the element type, and (b) presents the 3D model of the telecommunication tower.

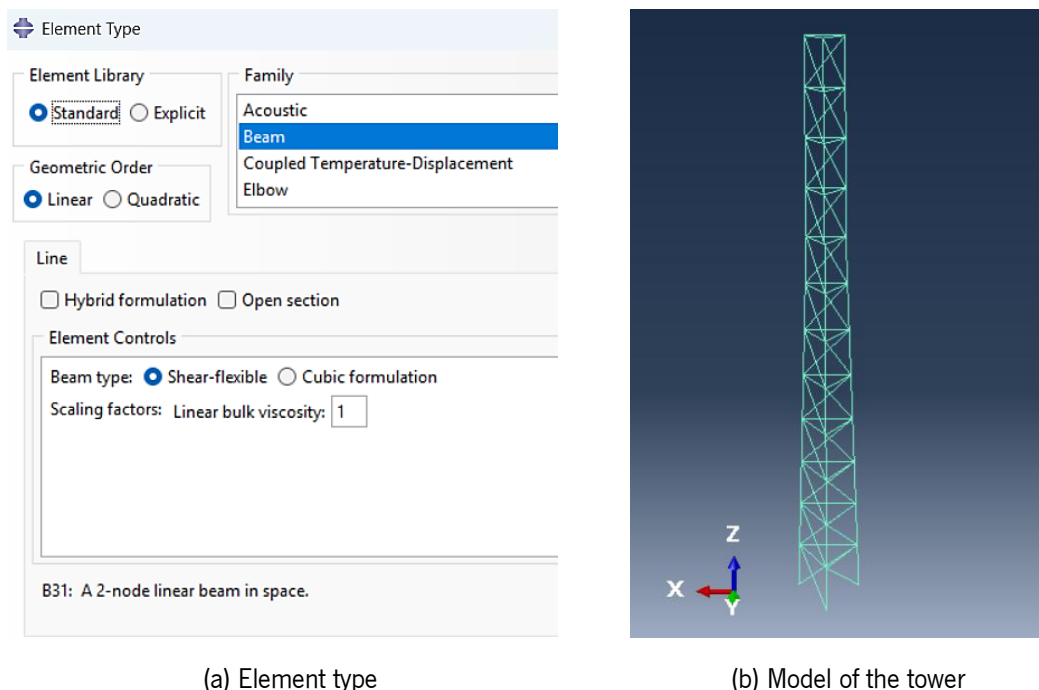
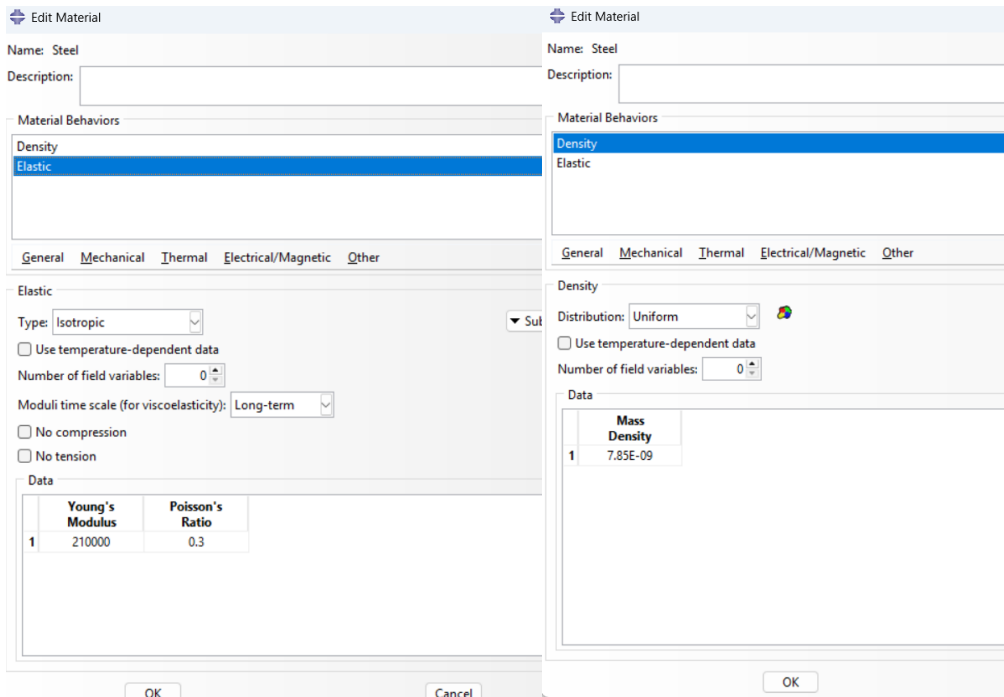


**Figure 3. 7:** Schematic of the tower geometry and element type

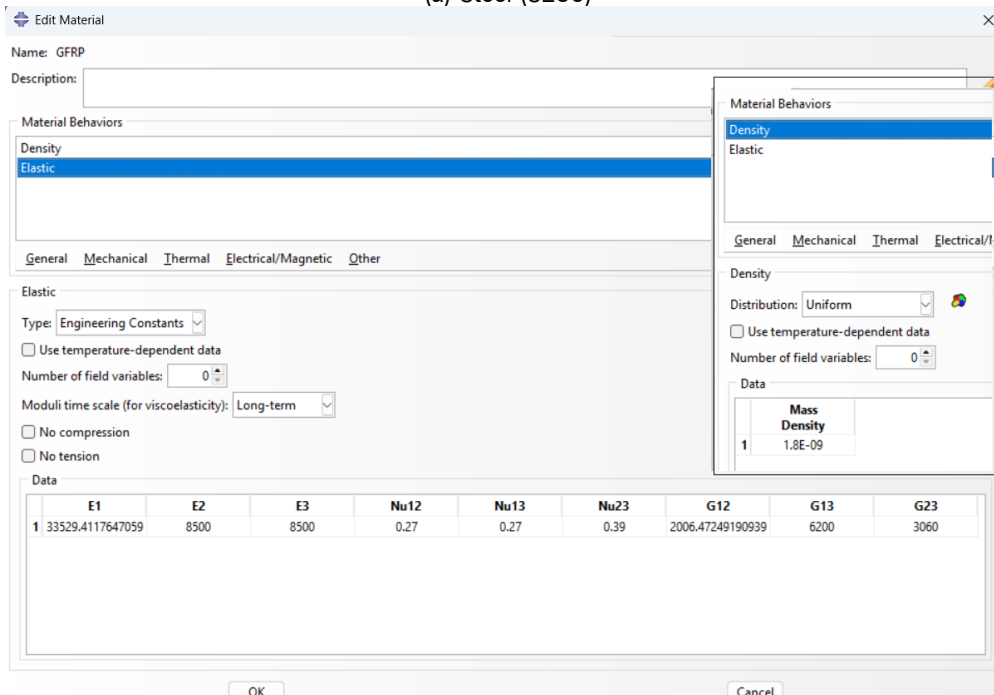
The units considered for the finite element model were millimetres (mm) for geometry, newtons (N) for forces, megapascals (MPa) for stresses, and tonnes (t) for mass.

### Material Properties

Material definitions included isotropic elastic properties and density for the steel baseline model (S235), as shown in Figure 3.8(a), and orthotropic properties for the GFRP pultruded profiles, defined using engineering constants, as shown in Figure 3.8(b).



(a) Steel (S235)



(b) M2/Elium-Glass (GFRP)

Figure 3. 8: Mechanical properties of materials

For the FRP case, environmental reduction factors and partial safety factors were applied in accordance with Section 3.4.5 to evaluate SLS conditions. The mechanical properties of the M2/Elium Glass pultruded profiles were provided by [94] and are presented in Table 3.4, which highlights the differences between SLS and ULS values, with SLS properties reduced to account for long-term effects and environmental exposure.

**Table 3. 4:** M2/Elium Glass Mechanical Properties (GFRP)

Properties		Units	Value without long-term coefficient	Value with long-term coefficient
Longitudinal tensile modulus	E11-t	MPa	57000.00	33529.41
Longitudinal compressive modulus	E11-c	MPa	54450.00	32029.41
Transverse tensile modulus	E22-t	MPa	8500.00	8500.00
Transverse compressive modulus	E22-c	MPa	15000.00	15000.00
Through-thickness tensile modulus	E33-t	MPa	8500.00	8500.00
Through-thickness compressive modulus	E33-c	MPa	15000.00	15000.00
Longitudinal tensile strength	f11,t	MPa	1050.00	1050.00
Longitudinal compressive strength	f11,c	MPa	765.00	765.00
Transverse tensile strength	f22,t	MPa	9.00	9.00
Transverse compressive strength	f22,c	MPa	110.00	110.00
Major Poisson's ratio	v12	-	0.27	0.27
Poisson's ratio	v23	-	0.39	0.39
In-plane shear strength	f12	MPa	25.00	25.00
In-plane shear modulus	G12	MPa	6200.00	2006.47
Shear strength in the 1–3 plane	f13	MPa	25.00	25.00
Shear modulus in the 1–3 plane	G13	MPa	6200.00	2006.47
Shear strength in the 2–3 plane	f23	MPa	12.00	12.00
Shear modulus in the 2–3	G23	MPa	3060.00	3060.00

### Sections and material orientation

The cross-sectional dimensions of the tower members were predefined, with larger sections at the base and progressively smaller sections toward the top. Initially, a direct comparison was conducted between the steel tower (S235 steel) and the GFRP tower (pultruded profiles). In this first step, the geometry and cross-sectional dimensions were kept identical. Modifications to the section sizes were introduced later during the first design loop to optimize the FRP structure.

In the FEM model, the beam element cross-sections were created in Profile Manager using section types pipe and L. Subsequently, Beam Sections were defined, specifying the material properties and section type. Using the Section Assignment Manager, each profile was assigned to the corresponding members of the tower model as shown in Figure 3.9.

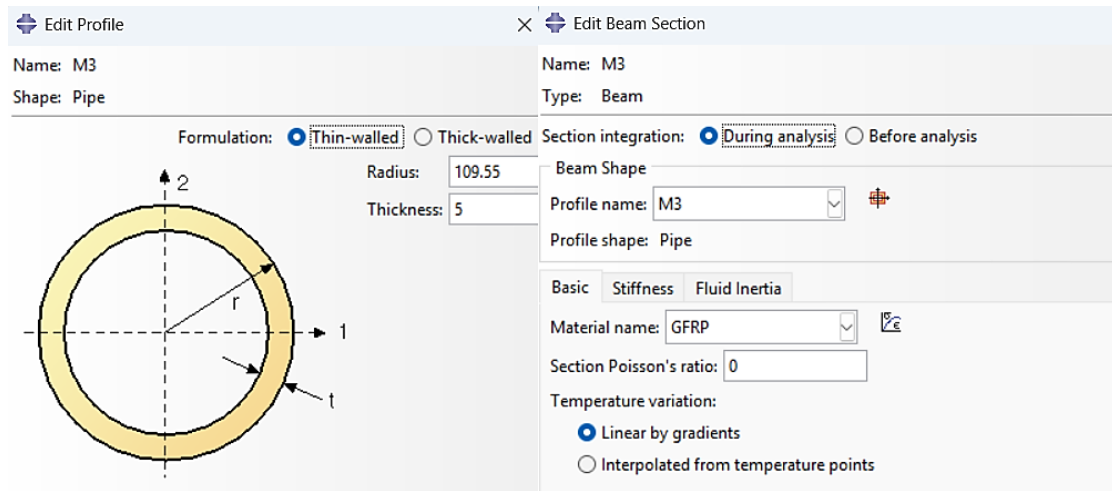


**Figure 3. 9:** Beam section and profiles

For the steel model, only beam orientations were defined, which control the rotation of the cross-section relative to the element axis. In contrast, for the GFRP pultruded profiles, both beam orientation and material orientation had to be specified. Beam orientation defines how the cross-section is rotated around the element's axis; on the other hand, material orientation was defined to indicate the primary fibre direction in the pultruded profiles. Different material orientations were assigned for horizontal members, main vertical members, and diagonal members, using a discrete definition approach. The assigned orientations are illustrated in Figure 3.10.

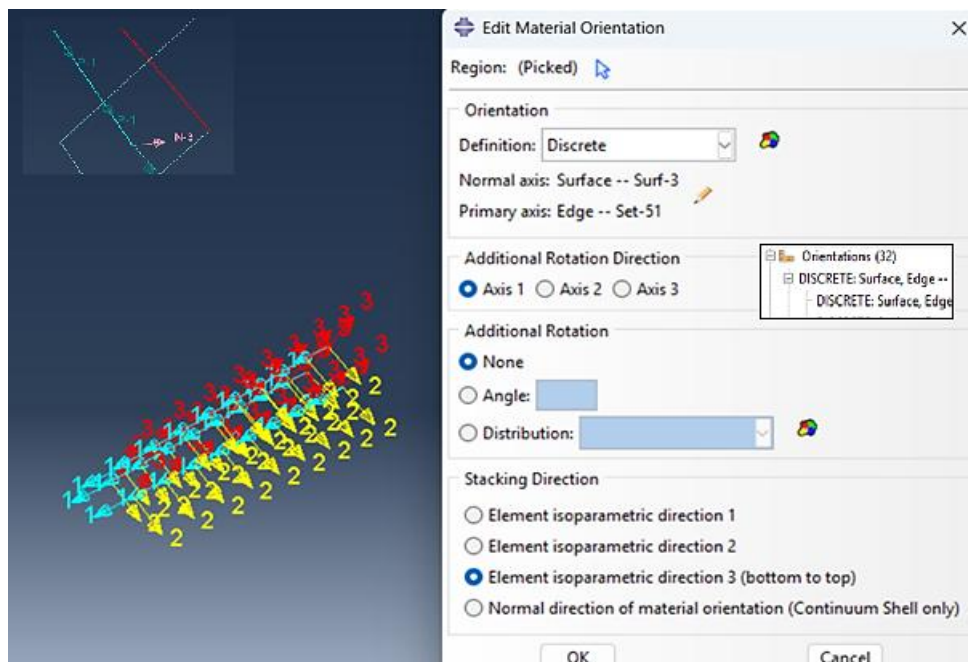


**Figure 3. 10:** Material orientation definition

## Boundary Conditions

Figure 3.11 shows the boundary conditions applied at the tower base. The base of each leg was modelled as clamped, restraining all translational degrees of freedom (U1, U2, U3) while leaving all rotational degrees of freedom (UR1, UR2, UR3) free. This configuration reproduces the real behaviour of the tower–foundation connection, where anchor bolts and base plates allow some rotation while preventing vertical and horizontal translation.

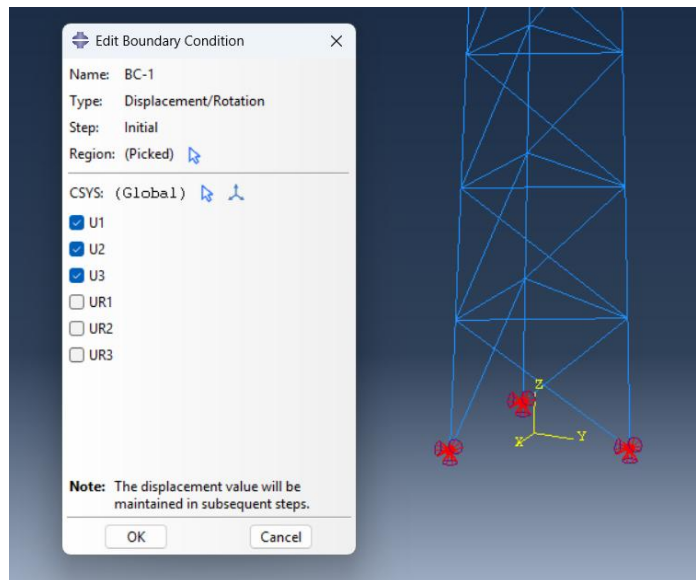


**Figure 3. 11:** Boundary condition of the tower

## Load Definition

Wind loads, self-weight, and equipment loads were applied as concentrated forces at nodes in the corresponding tower sections.

- ULS and SLS combinations were modelled as separate load cases, with partial safety factors applied directly to the load magnitudes in accordance with the relevant Eurocode provisions.
- Self-weight was included as a gravitational load in the global Z-direction.
- Wind loads were applied as equivalent nodal forces at each tower level in Y direction. These forces were obtained as mentioned in Section 3.4. The total force at each level was then distributed to the nodes of the tower.
- Frost effects were considered in the ULS combination by accounting for their influence on wind load incidence and by adding the corresponding increase in dead load due to ice accumulation.

The different load applications are illustrated in Figure 3.12.

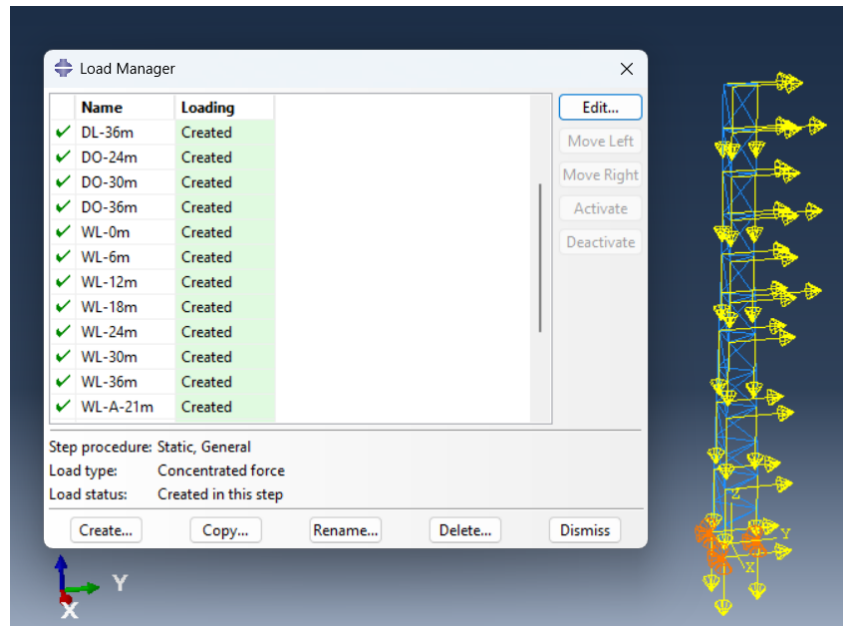


**Figure 3. 12:** Definition of Dead Load and Wind Load Cases in the FEM Model

### Step Definition

In the FEM model, a single Static, General analysis step was defined to apply the load combinations. Geometric nonlinearity (Nlgeom) was deactivated, meaning the analysis was performed under linear-geometric assumptions without accounting for second-order effects, as shown in Figure 3.13.

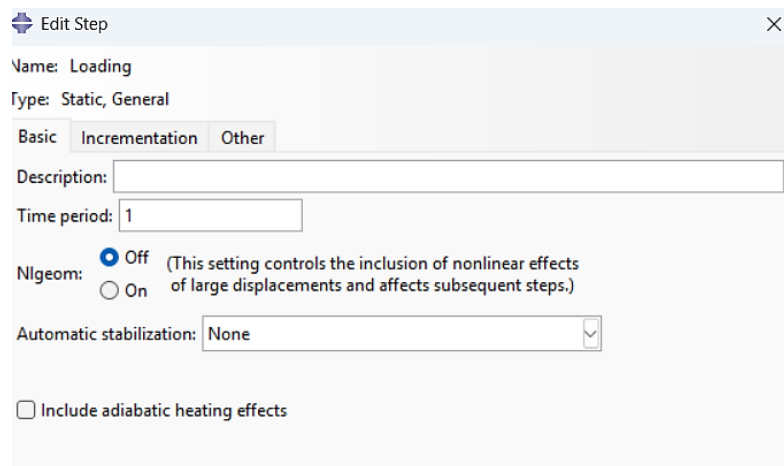


**Figure 3. 13:** Static analysis step

### Mesh

The tower geometry was meshed using linear beam elements (B31), which are suitable for modelling slender members subject to axial, bending, and torsional effects. A global element size of 100 mm was assigned, with curvature control activated to ensure accurate representation of member geometry. Minimum element size control was set to 10% of the global size to avoid excessively small elements. The final mesh consisted of 3,555 nodes and 3,624 elements, all of type B31, as shown in Figure 3.14.

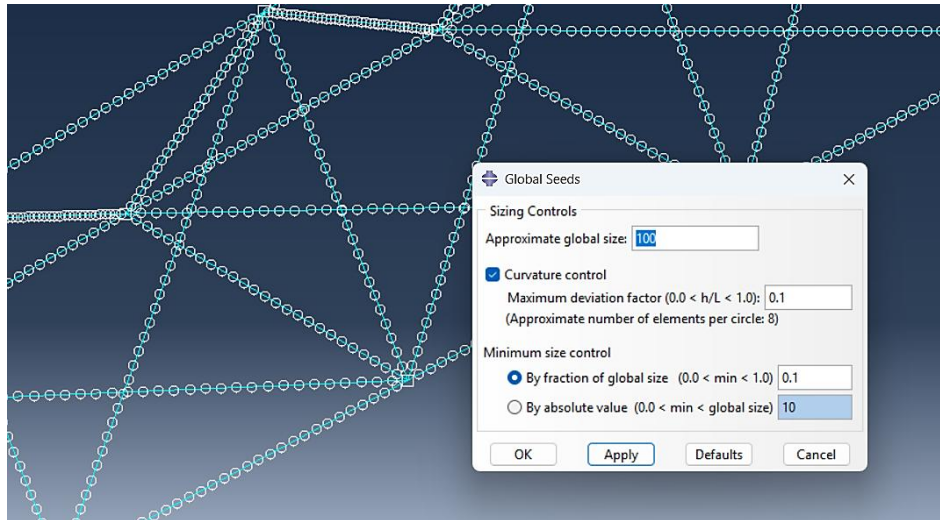


**Figure 3. 14:** Mesh definition

### 3.6. Structural Evaluation Criteria

The models were verified at SLS and ULS in accordance with EN 1990, EN 1993-3-1, and CEN/TS 19101. At SLS, performance was checked using characteristic actions (Eq. 3.26) with creep-reduced moduli per FprCEN/TS 19101 for long-term effects. It was required that the tip deflection within the project limit not exceeds the maximum tilt angle of  $0.66^\circ$ .

At ULS, member capacities were verified against factored actions (Eq. 3.25). For pultruded FRP members, the maximum-stress criterion was applied in each principal direction (tension/compression and shear), comparing the most unfavourable stress combination with the design strengths derived using the resistance model (Eq. 3.27) with the applicable  $\gamma_m$ ,  $\gamma_{Rd}$ , and  $\eta_c$  factors.

As a final check, the members were verified for bending, shear, tension and compression, in accordance with CEN/TS 19101.

#### 3.6.1. Axial tension

The design tensile resistance of the cross-section,  $N_{t,Rd}$ —computed from Eq. (3.31) using the cross-sectional area  $A$  and the characteristic tensile strength  $f_{x,t,k}$ —was checked against the design tensile action  $N_{t,Ed}$  obtained from Abaqus. Compliance is verified by ensuring  $N_{t,Ed} \leq N_{t,Rd}$  [89].

$$N_{t,Rd} = \frac{\eta_c}{\gamma_m \gamma_{Rd}} \cdot A \cdot f_{x,t,k} \quad (3.31)$$

### 3.6.2. Axial compression

Verification was performed by checking that the design compressive action from the FEM model,  $N_{c,Ed}$ , does not exceed the design compressive resistance,  $N_{c,Rd}$ . In accordance with Eq. (3.32).

$$N_{c,Rd} = \min(N_{c,Rd1}; N_{c,Rd2}) \quad (3.32)$$

Where  $N_{c,Rd1}$  is the cross-section crushing/local-buckling resistance given by Eq. (3.33)] based on the longitudinal characteristic compressive strength  $f_{x,c,k}$  and  $N_{c,Rd2}$  is the member (global) buckling resistance (Eq. (3.34)), which incorporates the reduction factor  $\chi_E$  to account for the interaction between local and flexural buckling [89]. Finally, the requirement is satisfied when  $N_{c,Ed} \leq N_{c,Rd}$  [89].

$$N_{c,Rd1} = \frac{\eta_c}{\gamma_m \cdot \gamma_{Rd}} \cdot A \cdot f_{x,c,k} \quad (3.33)$$

$$N_{c,Rd2} = \chi_E \cdot N_{cr,Rd} \quad (3.34)$$

### 3.6.3. Bending

To check bending in the design, verify that the design bending moment about the relevant principal axis  $M_{Ed}$  does not exceed the design bending resistance  $M_{Rd}$ , given by Eq. (3.35).

$$M_{Rd} = \min(M_{Rd1}; M_{Rd2}) \quad (3.35)$$

The cross-section (material) resistance is:

$$M_{Rd1} = W \cdot \min \left\{ \frac{\eta_c}{\gamma_m \cdot \gamma_{Rd}} \cdot f_{x,t,k}; \frac{\eta_c}{\gamma_m \cdot \gamma_{Rd}} \cdot f_{x,c,k} \right\} \quad (3.36)$$

Where  $W$  is the elastic section modulus of the cross-section about the relevant principal axis;  $f_{x,t,k}$  and  $f_{x,c,k}$  are the characteristic longitudinal tensile and compressive strengths; and  $\eta_c$ ,  $\gamma_m$ ,  $\gamma_{Rd}$  are the conversion and partial safety factors [89].

The member buckling resistance is given by Eq. (3.37) where  $\chi_{LT}$  is the reduction factor accounting for interaction between local and lateral-torsional buckling, and  $M_{cr,Rd}$  is the design resistance to local buckling of the cross-section.

$$M_{Rd2} = \chi_{LT} \cdot M_{cr,Rd} \quad (3.37)$$

## 3.6.4. Shear

To verify shear, it's necessary to confirm that the design shear action at each critical cross-section from the FEM model,  $V_{Ed}$ , does not exceed the design shear resistance  $V_{Rd}$ .

The design shear resistance to material failure of the cross-section is defined in Eq. (3.38):

$$V_{Rd} = \frac{\eta_c}{\gamma_m \cdot \gamma_{Rd}} \cdot A_v \cdot f_{xy,v,k} \quad (3.38)$$

where:

- $A_v$  is the shear area of the cross-section (computed per the expression shown in Figure 3.15 for the relevant section type and shear direction);
- $f_{xy,v,k}$  is the characteristic in-plane shear strength of the material in the  $xy$  plane;
- $\eta_c$  is the conversion factor for environmental/conditioning effects;
- $\gamma_m$  and  $\gamma_{Rd}$  are the partial safety factors for material and resistance, respectively.

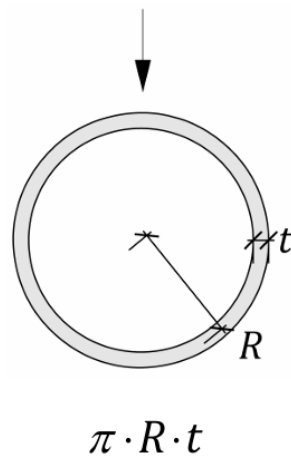


**Figure 3. 15:** Shear area formula, adapted from [89].

THIS PAGE WAS INTENTIONALLY

## 4. FIRST DESIGN LOOP

The first design loop aimed to evaluate the performance of a GFRP-based telecommunication tower while maintaining the geometry of the existing 36 m steel reference model. The objective was to determine whether replacing the steel members with pultruded GFRP profiles could meet serviceability and ultimate limit state requirements without altering the structural configuration. In this stage, displacements and stresses were compared between the steel and GFRP models, along with the total weight of the profiles. The results indicated that increasing the cross-sectional dimensions of the GFRP members was necessary to achieve satisfactory performance.

### 4.1. Model Description

The numerical model for the first design loop maintained the same lattice configuration, overall dimensions, and member layout as the steel reference tower described in Chapter 3. The only changes involved replacing the steel members with pultruded GFRP circular profiles and applying the corresponding orthotropic material properties. Connection modelling, boundary conditions, and loading cases were consistent with those previously defined in the methodology.

The cross-sectional dimensions of the GFRP profiles were predefined, with larger sections at the base and progressively smaller sections toward the top to reflect the variation in axial load demand along the tower height (Table 4.1). The distribution of the member sizes along the structure is illustrated in Figure 4.1.

**Table 4. 1:** Member Profiles and Dimensions

Section	Leg	Crossmember	Diagonal
1 (0m – 6m)	Φ219.10mm x 5mm	Φ76.10mm x 4mm	Φ88.90mm x 4mm
2 (6m – 12m)	Φ168.30mm x 5mm	Φ76.10mm x 3mm	Φ88.90mm x 3mm
3 (12m – 18m)	Φ168.30mm x 5mm	Φ60.30mm x 4mm	Φ88.90mm x 3mm
4 (18m – 24m)	Φ139.70mm x 5mm	Φ60.30mm x 3mm	Φ88.90mm x 3mm
5 (24m – 30m)	Φ114.30mm x 6mm	L70mm x 7mm	Φ88.90mm x 3mm
6 (30m – 36m)	Φ114.30mm x 5mm	L60mm x 6mm	Φ76.10mm x 3mm

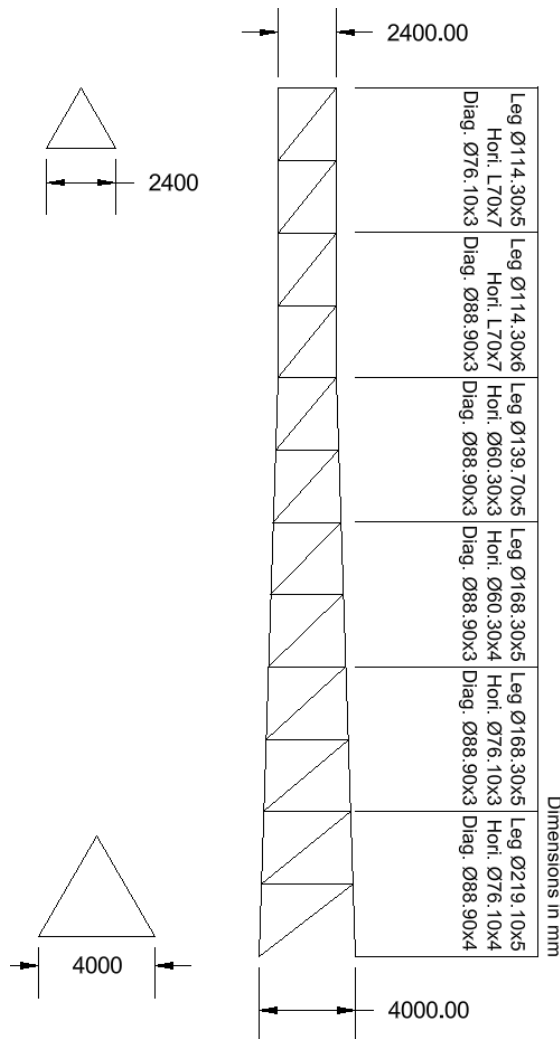


Figure 4. 1: Cross-section distribution along the tower

## 4.2. Material Properties

The GFRP members were modelled as orthotropic material using the engineering constants of M2/Elium Glass pultruded profiles, as detailed in Table 3.4 of Chapter 3. Environmental reduction factors and partial safety factors were applied in accordance with Section 3.4. No additional modifications to the material properties were made for this design loop.

## 4.3. Results of Load Calculation

The load cases and combinations defined in Chapter 3 were evaluated to obtain the actions used in the FEM analyses. Detailed calculations (per section, with/without frost, linear and point equipment, and antenna levels) are provided in Annex A. This section presents the governing load values common to the steel and GFRP analyses.

The parameters used to calculate wind actions – such as reference and average wind speeds, turbulence intensity, peak dynamic pressure, total force coefficients, and reference areas – are listed in Table 4.2 for each tower section, considering both with- and without-frost scenarios.

**Table 4. 2:** Parameters for wind action calculations for each tower section (with and without frost)

Parameter	Unit	Sym- bol	Section 1	Section 2	Section 3	Section 4	Section 5	Section 6	Base 6
Height	m	H	36-30	30-24	24-18	18-12	12-6	6-0	0
Reference wind speed	m/s	$V_b$	26	26	26	26	26	26	26
Height above ground	m	Z	36.25	30.25	24.25	18.25	12.25	6.25	0.25
Average wind speed	m/s	$V_m(z)$	32.54	31.64	30.55	29.15	27.18	23.85	18.20
Turbulence intensity	-	$I_v(z)$	0.15	0.16	0.16	0.17	0.18	0.21	0.27
Peak dynamic pressure	Pa	$q_p(z)$	1337.49	1283.42	1218.69	1137.60	1027.96	853.65	586.34
Reference area structure without frost	m <sup>2</sup>	$A_{ref}$	5.18	5.33	5.58	6.01	6.21	6.91	0.27
Total force coefficient without frost	-	$C_f$	1.35	1.35	1.25	1.29	1.31	1.32	1.37
Reference area structure with frost	m <sup>2</sup>	$A_{ref}$	6.29	6.43	6.69	7.16	7.40	8.14	0.35
Total force coefficient with frost	-	$C_f$	1.37	1.37	1.26	1.28	1.29	1.30	1.36

Wind loads from point equipment were calculated based on antenna dimensions, installation heights, and aerodynamic coefficients. The relevant data are summarised in Table 4.3, which includes the projected areas for each section and the corresponding force coefficients.

**Table 4. 3:** Antenna geometry and aerodynamic coefficients for wind action calculations

Antenna Details			Without frost			With frost		
Parameter	Unit	Sym- bol	Section 1	Section 2	Section 3	Section 1	Section 2	Section 3
Level (HMA)	m	-	33	27	21	33	27	21
Projected antenna area	m <sup>2</sup>	AA	9	9	6	10.4	10.4	6.9
Drag coefficient of point equipment	m <sup>2</sup>	$C_{f,A,0}$	1	1	1	1	1	1
Reduction coefficient	-	KA	1	1	1	1	1	1
Force coefficient of point equipment	-	$C_{f,A}$	1	1	1	1	1	1

To obtain the governing values for each component, the wind force, average wind force, and gust wind force were calculated for the structure, linear equipment, and antennas. The highest value in each case was adopted for subsequent load combinations. These results, for both frost and no-frost conditions, are presented in Table 4.4.

**Table 4. 4:** Calculated wind forces for structure, linear equipment, and antennas by section

Details	Description		Section1	Section2	Section3	Section4	Section5	Section6	
<b>Structure</b>	Wind force (N)	NF <sup>1</sup>	F <sub>w</sub>	8764.7	8659.9	7920.0	8243.7	7799.4	7273.4
		WF <sup>2</sup>		12496.8	12302.4	11162.7	11302.4	10715.3	9848.5
	Wind force (average) (N)	NF	F <sub>m,w(z)</sub>	4544.2	4425.5	3973.2	4032.5	3670.8	3175.4
		WF		5568.1	5402.8	4812.5	4751.2	4333.9	3695.0
	Wind force (gusts) (N)	NF	F <sub>T,w(z)</sub>	9608.8	9249.6	8273.3	8457.2	7893.7	7297.8
		WF		13882.5	13263.3	11731.0	11634.5	10861.0	9885.0
<b>Linear Equipment</b>	Wind force (N)	NF	F <sub>w,LE</sub>	1752.8	1555.2	1476.8	0.0	0.0	199.2
		WF		3129.2	2681.0	2545.8	0.0	0.0	499.3
	Wind force (average) (N)	NF	F <sub>m,w,LE(z)</sub>	908.8	794.8	740.8	0.0	0.0	87.0
		WF		1394.3	1177.4	1097.5	0.0	0.0	187.3
	Wind force (gusts) (N)	NF	F <sub>T,w,LE(z)</sub>	1921.6	1661.1	1542.6	0.0	0.0	199.9
		WF		3476.2	2890.4	2675.4	0.0	0.0	501.2
<b>Point equipment (antenna)</b>	Wind force (N)	NF	F <sub>w,A</sub>	11255.0	10800.0	6836.8	0.0	0.0	0.0
		WF		15134.0	14522.2	9148.9	0.0	0.0	0.0
	Wind force (average) (N)	NF	F <sub>m,w,A(z)</sub>	5835.4	5519.1	3429.8	0.0	0.0	0.0
		WF		6743.1	6377.7	3944.3	0.0	0.0	0.0
	Wind force (gusts) (N)	NF	F <sub>T,w,A(z)</sub>	12338.9	11535.5	7141.8	0.0	0.0	0.0
		WF		16812.1	15656.5	9614.8	0.0	0.0	0.0

1:NF- No frost considered, 2:WF- With frost

Permanent and variable loads applied to the reference tower – in both the steel and GFRP pultruded profile configurations – are summarised in Table 4.5. Permanent loads include the self-weight of the structure and equipment, while variable loads account for frost mass, operational loads, and wind actions.

**Table 4. 5:** Summary of permanent and variable loads applied to the reference tower

Summary of loads	Units		Section 1	Section 2	Section 3	Section 4	Section 5	Section 6	Base 6
Section height	m	-	6	6	6	6	6	6	0.25
<b>Permanent load</b>									
Tower mass (structure and equipment)	kg	-	2275.0	2380.3	2140.2	944.7	1000.7	1421.5	165.7
<b>Variable loads</b>									
Frost mass (structure and equipment)	kg	-	1357.2	1425.5	1332.0	600.2	647.5	827.3	18.5
Operating load	N	-	9960.0	9960.0	9960.0	0.0	0.0	0.0	0.0
Snow load	N	-	0.0	0.0	0.0	0.0	0.0	0.0	0.0
Temperature load	N	-	0.0	0.0	0.0	0.0	0.0	0.0	0.0
Wind without frost (structure)	N	-	9608.8	9249.6	8273.3	8457.2	7893.7	7297.8	207.9
Wind without frost (equipment)	N	-	1921.6	1661.1	1542.6	0.0	0.0	199.9	0.0
Wind without frost (antennas)	N	-	12338.9	11535.5	7141.8	0.0	0.0	0.0	0.0
Antenna level	m	-	33.0	27.0	21.0	0.0	0.0	0.0	0.0

Wind with frost (structure)	N	-	13882.5	13263.3	11731.0	11634.5	10861.0	9885.0	301.0
Wind with icing (equipment)	N	-	3476.2	2890.4	2675.4	0.0	0.0	501.2	0.0
Wind with icing (antennas)	N	-	16812.1	15656.5	9614.8	0.0	0.0	0.0	0.0
Antenna level	m	-	33.0	27.0	21.0	0.0	0.0	0.0	0.0

The governing load combinations for the Serviceability Limit State (SLS) and Ultimate Limit State (ULS) were determined in accordance with EN 1990, EN 1991-1-4, and EN 1993-3-1, considering wind as the dominant variable action. Only wind forces acting perpendicular (90°) to one tower face, oriented in the Y direction, were considered for these cases, as this direction produced the highest response in preliminary checks.

For the SLS combination, it incorporates permanent loads, wind loads (without frost) from the structure, linear equipment, and antennas, as well as 70% of the operational load.

For the ULS, two combinations were assessed:

- ULS Combination 1 (no frost): Factored permanent loads, wind loads (without frost) from all components, and the full operational load.
- ULS Combination 2 (with frost): Factored permanent loads, wind loads (with frost factors applied) from all components, and the additional weight of frost.

Table 4.6 summarizes the distributed loads per tower section for each of these governing combinations, which were applied identically to both the steel and GFRP FEM models.

**Table 4. 6:** Load combinations (SLS and ULS)

SLS COMBINATIONS							
Type	Section 1	Section 2	Section 3	Section 4	Section 5	Section 6	Base 6
Additional dead load	17611.3	17634.7	15522.0	2650.4	2974.8	4617.7	1370.1
Wind load structure (without frost)	9608.8	9249.6	8273.3	8457.2	7893.7	7297.8	207.9
Wind loads linear equipment (without frost)	1921.6	1661.1	1542.6	0.0	0.0	199.9	0.0
Wind antennas equipment (without frost)	12338.9	11535.5	7141.8	0.0	0.0	0.0	0.0
0.7*operational load	9960.0	9960.0	9960.0	0.0	0.0	0.0	0.0
ULS COMBINATION 1							
Type	Section 1	Section 2	Section 3	Section 4	Section 5	Section 6	Base 6
Additional dead load	19372.5	19398.2	17074.2	2915.4	3272.3	5079.4	1507.1
Wind load structure (without frost)	13452.3	12949.5	11582.6	11840.1	11051.1	10216.9	291.0
Wind loads linear equipment (without frost)	2690.2	2325.5	2159.7	0.0	0.0	279.8	0.0
Wind antennas equipment (without frost)	17274.4	16149.6	9998.5	0.0	0.0	0.0	0.0
Operational load	10458.0	10458.0	10458.0	0.0	0.0	0.0	0.0

ULS COMBINATION 2							
Type	Section 1	Section 2	Section 3	Section 4	Section 5	Section 6	Base 6
Additional dead load	19372.5	19398.2	17074.2	2915.4	3272.3	5079.4	1507.1
Wind load structure (without frost)	12494.3	11937.0	10557.9	10471.1	9774.9	8896.5	270.9
Wind loads linear equipment (without frost)	3128.6	2601.4	2407.9	0.0	0.0	451.0	0.0
Wind antennas equipment (without frost)	15130.9	14090.8	8653.3	0.0	0.0	0.0	0.0
Weight of frost	11184.2	11746.5	10975.8	4945.8	5336.0	6817.0	152.2

#### 4.4. Comparison of results (Steel vs GFRP)

Two finite element models were created to evaluate the Serviceability Limit State (SLS) deformations for both the steel and GFRP towers, and four additional models were used to assess the Ultimate Limit State (ULS) under the load combinations. In all cases, the same loads, geometry, and cross-sectional dimensions were applied to ensure a consistent comparison between materials.

##### 4.4.1. Maximum lateral displacement in Steel and GFRP Towers

As shown in Figure 4.2, the maximum lateral displacement at the top of the steel tower was 252.40 mm, whereas Figure 4.3(b) shows the GFRP tower exhibiting a maximum displacement of 1582 mm, which is approximately 6.27 times greater. This significant increase in deflection is attributed to the lower elastic modulus of GFRP compared to steel, as discussed further in Section 4.4.3.

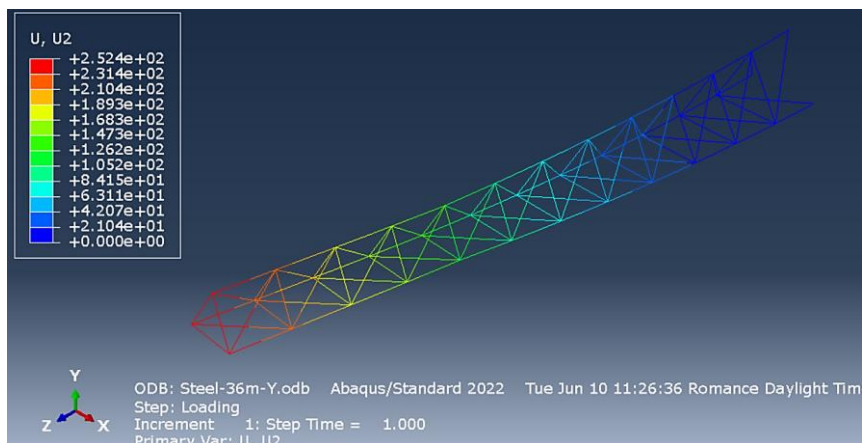
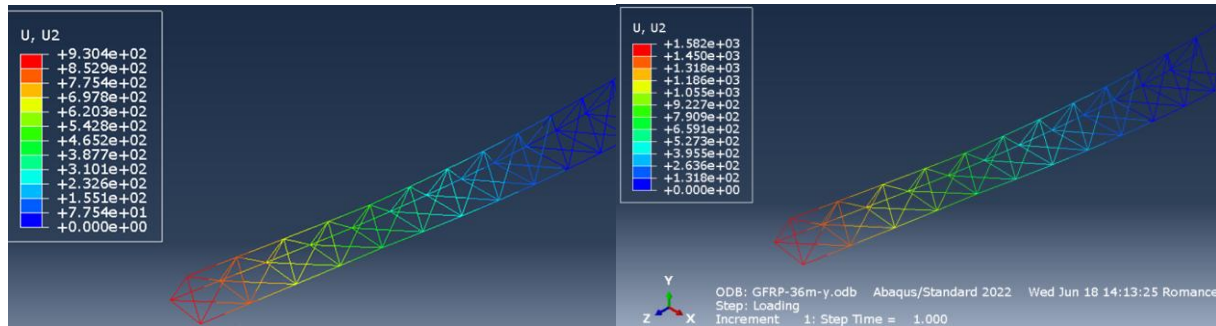


**Figure 4. 2:** Maximum displacement U2 of the steel tower

To evaluate the long-term effects and the impact of creep, which reduces the mechanical properties of GFRP, the tower was modelled using both unreduced and reduced material properties. Figure 4.3 compares the results of these two scenarios. In Figure 4.3(a), the model without the creep coefficient

shows a maximum displacement of 930.40 mm, whereas Figure 4.3(b), with reduced properties accounting for long-term effects, shows a displacement of 1582 mm – an increase of approximately 70%.



(a) Unreduced mechanical properties

(b) With long-term coefficients

**Figure 4. 3:** Maximum displacement U2 of the GFRP tower

#### 4.4.2. Maximum Stress in Steel and GFRP Towers

Under ULS loading, the reference steel tower exhibits a maximum compressive stress of 203.02 MPa, evaluated using the Von Mises criterion, as shown in Figure 4.4.

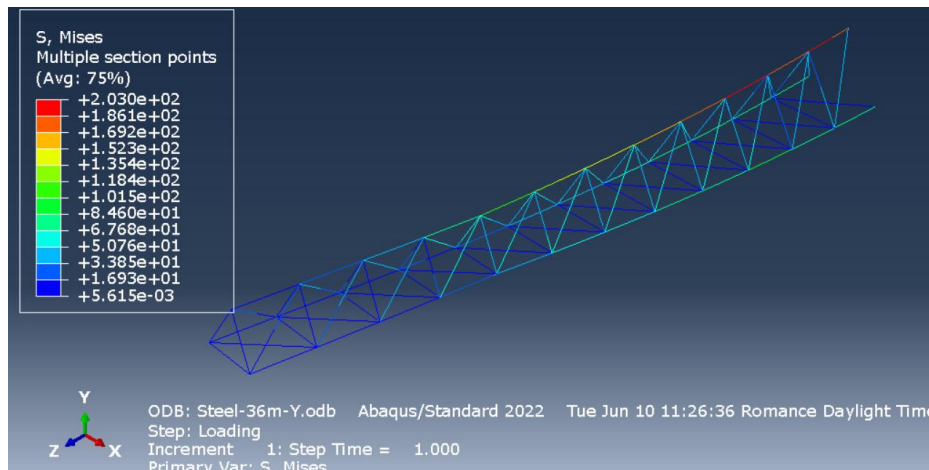


**Figure 4. 4:** Maximum stress (Von Mises) of the steel tower

For the GFRP tower, the evaluation focused on axial stress (S11) due to the orthotropic nature of the material. Figure 4.5(a) corresponds to ULS Combination 1, showing maximum values of 129.70 MPa in tension and 281.70 MPa in compression. Figure 4.5(b) corresponds to ULS Combination 2, with maximum values of 90.40 MPa in tension and 203.00 MPa in compression.

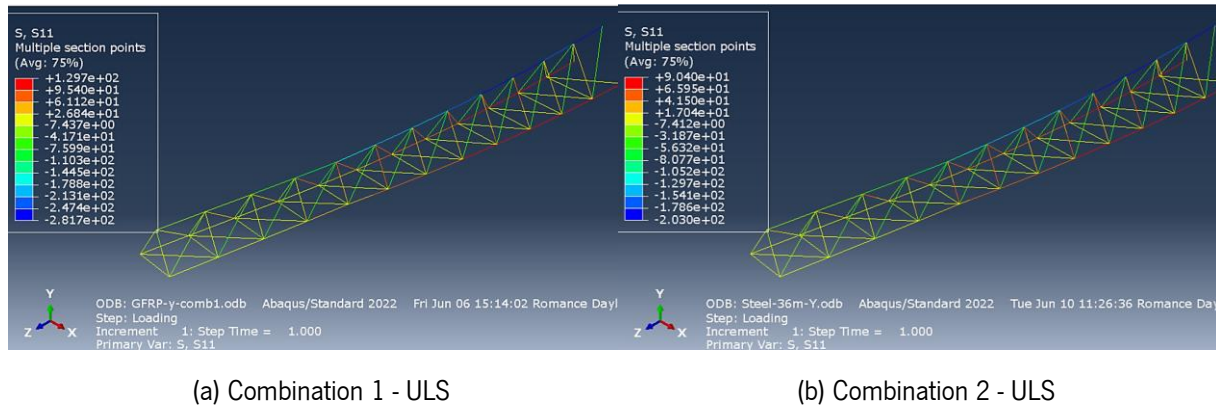


**Figure 4. 5:** Maximum axial stress (S11) of GFRP tower

The most critical values observed under Combination 1. The envelope of these stresses will later be compared with the design resistance to verify compliance with strength requirements.

#### 4.4.3. Summary of results and verification

The verification of the maximum displacement was carried out based on the allowable tilt angle requirement of  $0.66^\circ$ . The tilt angle,  $\theta$ , was calculated using Eq. (4.1), where  $\Delta$  represents the maximum lateral displacement at the antenna level and  $H_a$  is the antenna mounting height (also referred to as the effective height)

$$\theta = \arctan\left(\frac{\Delta}{H_a}\right) \tag{4. 1}$$

The results are presented in Table 4.7. As shown, the GFRP pultruded profile tower exceeds the maximum allowable tilt angle by approximately 1.98 times, whereas the steel tower satisfies the deformation requirement under the Serviceability Limit State (SLS) combination.

**Table 4. 7:** Strength Verification of GFRP Pultruded Profiles under Maximum Stresses

Tower	Displacement (mm)	Tilt angle	Maximum tilt angle	Verification $\theta < \theta_{max}$
Steel	252.4	0.55	0.66	OK
GFRP	1582	1.31	0.66	Exceeds limit

The verification of the maximum stress was also performed, as presented in Table 4.8. The maximum tensile and compressive stress obtained under the Ultimate Limit State (ULS) combinations were compared against the corresponding design resistance values. The procedure for determining the design resistance values has been described in Section 3.4.1 of the methodology, where the mean values are

reduced to characteristic values and then adjusted by partial safety factors and environmental reduction coefficients.

The results indicate that for both tensile ( $f_{11,t}$ ) and compressive ( $f_{11,c}$ ) directions, the design effect of actions is lower than the design resistance values, confirming compliance with the strength requirements.

**Table 4. 8:** Strength Verification of GFRP Pultruded Profiles under Maximum Stresses

Properties	Units	Mean Value	Characteristic Value	$\gamma_m$	$\eta_c$	$\gamma_{Rd}$	Design Resistance Values	Design Effect of actions	Verification $Ed < R_d$
$f_{11,t}$	MPa	1050	889.98	1.23	0.85	1.4	439.31	129.7	OK
$f_{11,c}$	MPa	765	612.45	1.32	0.85	1.4	291.73	281.7	OK

**Conclusion of comparison:** The comparative analysis shows that the GFRP tower experiences significantly higher tip displacements than the steel tower, primarily due to its lower modulus of elasticity. This increased deformation results in the exceedance of the serviceability limit for allowable tilt angle, making stiffness enhancement a primary design priority. Nevertheless, under Ultimate Limit State (ULS) loading, the maximum tensile and compressive stresses in the GFRP pultruded profiles remain below the corresponding design resistance values, indicating no immediate risk of material failure.

Based on these findings, a first design iteration will be undertaken with the objective of reducing deformations and improving the overall stiffness of the GFRP structure. Subsequent structural verifications will address axial compression, axial tension, shear, and bending performance to ensure compliance with all relevant design criteria.

## 4.5. Redesign for Stiffness Improvement

### 4.5.1. Objective

The results in Section 4.4 showed that the baseline GFRP tower significantly exceeded the allowable tilt angle due to its lower modulus of elasticity, despite satisfying ULS strength checks. The objective of the first design loop was to reduce displacements while controlling the total tower mass to remain comparable with the steel reference tower which has a mass of 3.77 t.

Several strategies were explored, including:

- Increasing cross-section diameter and wall thickness of members.
- Modifying the bracing configuration (from Z-diagonals to X-diagonals).

- Introducing hybrid designs combining CFRP and GFRP.
- Using a full CFRP configuration for further stiffness-to-weight improvement.

All configurations were analysed under the SLS load scenarios presented in Table 4.10 to evaluate the tip displacement.

#### 4.5.2. Wind Load Scenarios and Geometric Properties

Each configuration in the first design loop was modelled with its corresponding member dimensions described in Table 4.9 and analysed under the governing SLS wind load scenario from Table 4.10 to determine tip displacement, tilt angle, weight and axial stress.

The main modifications between iterations are summarized below:

- **Iteration 1:** GFRP members with cross-sectional areas four times larger than those of the reference steel tower, combined with increased wall thickness.
- **Iteration 2:** GFRP members with cross-sectional areas three times larger than those of the reference steel tower and increase wall thickness, to reduce mass while maintaining stiffness.
- **Iteration 3:** GFRP tower with X-bracing replacing Z-bracing for improved lateral stiffness.
- **Iteration 4:** Hybrid configuration with CFRP legs and GFRP bracing, same dimensions as the steel reference tower.
- **Iteration 5:** Hybrid configuration with CFRP legs, GFRP bracing, and increased diameter and thickness.
- **Iteration 6:** Full CFRP tower with same dimensions as steel reference.
- **Iteration 7:** Full CFRP tower with increased diameter and thickness for stiffness improvement.

#### Member Dimensions for Modified Configurations

The geometric properties for each tower section in the modified configurations are summarised in Table 4.9. These dimensions directly define the FEM models and reflect the specific design changes implemented in each iteration, while Iterations 4 and 6 retain the same geometry as the reference steel tower.

**Table 4. 9:** Member Dimensions for Modified Tower Configurations

Iteration	Section	Leg	Crossmember	Diagonal
<b>1 – ×4 CS &amp; t (GFRP)</b>	1 (0m – 6m)	Φ876.4mm x 15mm	Φ304.4mm x 12mm	Φ355.6mm x 12mm
	2 (6m – 12m)	Φ673.2mm x 15mm	Φ304.4mm x 9mm	Φ355.6mm x 9mm

	3 (12m – 18m)	Φ673.2mm x 15mm	Φ241.2mm x 12mm	Φ355.6mm x 9mm
	4 (18m – 24m)	Φ588.8mm x 15mm	Φ241.2mm x 9mm	Φ355.6mm x 9mm
	5 (24m – 30m)	Φ457.2mm x 18mm	Φ241.2mm x 9mm	Φ355.6mm x 9mm
	6 (30m – 36m)	Φ457.2mm x 15mm	Φ241.2mm x 9mm	Φ304.4mm x 9mm
<b>2 – ×3 CS &amp; t (GFRP)</b>	1 (0m – 6m)	Φ700mm x 14mm	Φ240mm x 8mm	Φ300mm x 10mm
	2 (6m – 12m)	Φ600mm x 12mm	Φ240mm x 6mm	Φ300mm x 8mm
	3 (12m – 18m)	Φ600mm x 12mm	Φ200mm x 8mm	Φ300mm x 8mm
	4 (18m – 24m)	Φ480mm x 12mm	Φ200mm x 8mm	Φ300mm x 8mm
	5 (24m – 30m)	Φ400mm x 10mm	Φ200mm x 8mm	Φ300mm x 8mm
	6 (30m – 36m)	Φ400mm x 10mm	Φ200mm x 8mm	Φ240mm x 8mm
<b>3 – X-bracing (GFRP)</b>	1 (0m – 6m)	Φ426.13mm x 16mm	Φ120mm x 8mm	Φ150mm x 8mm
	2 (6m – 12m)	Φ328.71mm x 14mm	Φ120mm x 7mm	Φ150mm x 8mm
	3 (12m – 18m)	Φ328.71mm x 14mm	Φ100mm x 6mm	Φ150mm x 8mm
	4 (18m – 24m)	Φ272.85mm x 14mm	Φ100mm x 6mm	Φ150mm x 8mm
	5 (24m – 30m)	Φ248.2mm x 14mm	Φ100mm x 6mm	Φ150mm x 8mm
	6 (30m – 36m)	Φ248.2mm x 12mm	Φ100mm x 6mm	Φ120mm x 8mm
<b>4 – Hybrid CFRP+GFRP</b>	1 (0m – 6m)	Φ438.2mm x 7mm	Φ152.2mm x 6mm	Φ177.8mm x 6mm
	2 (6m – 12m)	Φ336.6mm x 7mm	Φ152.2mm x 5mm	Φ177.8mm x 5mm
	3 (12m – 18m)	Φ336.6mm x 7mm	Φ120.6mm x 6mm	Φ177.8mm x 5mm
	4 (18m – 24m)	Φ279.4mm x 7mm	Φ120.6mm x 5mm	Φ177.8mm x 5mm
	5 (24m – 30m)	Φ228.6mm x 8mm	Φ120.6mm x 5mm	Φ177.8mm x 5mm
	6 (30m – 36m)	Φ228.6mm x 7mm	Φ120.6mm x 5mm	Φ152.2mm x 5mm
<b>5 – Full CFRP</b>	1 (0m – 6m)	Φ383.42mm x 8mm	Φ133.17mm x 7mm	Φ155.57mm x 7mm
	2 (6m – 12m)	Φ294.52mm x 8mm	Φ133.17mm x 6mm	Φ155.57mm x 6mm
	3 (12m – 18m)	Φ294.52mm x 8mm	Φ105.52mm x 7mm	Φ155.57mm x 6mm
	4 (18m – 24m)	Φ244.47mm x 8mm	Φ105.52mm x 6mm	Φ155.57mm x 6mm
	5 (24m – 30m)	Φ200.02mm x 9mm	Φ105.52mm x 6mm	Φ155.57mm x 6mm
	6 (30m – 36m)	Φ200.02mm x 8mm	Φ105.52mm x 6mm	Φ133.17mm x 6mm

### Summary of Governing SLS Loads

Table 4.10 summarises the total SLS forces per section for each iteration in the modified configurations. These values were used as input for the FEM analyses presented in the subsequent section. For Iterations 4 and 6, the applied loads were identical to those of the reference steel tower, allowing direct comparison of the results. The operational load remained constant for all cases, with 9960.0 N applied to Sections 6, 5, and 4 of the towers.

**Table 4. 10:** Governing SLS Loads per Tower Section for Modified Configurations

Iteration	Section	Additional Dead Load [N]	Wind Load Structure (no frost) [N]	Wind Load Linear Equip. [N]	Wind Load Antennas [N]
<b>1 – ×4 CS &amp; t</b>	6 (30-36m)	18733.7	17727.1	1921.6	12338.9
	5 (24-30m)	18827.1	17069.8	1661.1	11535.5
	4 (18-24m)	17183.4	17222.0	1542.6	7141.8
	3 (12-18m)	5318.2	20156.7	0.0	0.0
	2 (6-12m)	5788.2	18709.3	0.0	0.0
	1 (0–6 m)	9237.4	18091.4	199.9	0.0
<b>2 – ×3 CS &amp; t</b>	6 (30-36m)	19138.2	16228.8	1939.6	12454.5
	5 (24-30m)	19483.4	16295.6	1676.3	11640.8
	4 (18-24m)	18026.6	16197.6	1556.4	7205.5
	3 (12-18m)	7026.7	18988.6	0.0	0.0
	2 (6-12m)	7686.5	17558.2	0.0	0.0
	1 (0–6 m)	11159.4	15905.8	201.6	0.0
<b>3 – X-bracing</b>	6 (30-36m)	17543.6	11468.2	1917.0	12309.2
	5 (24-30m)	17484.1	10956.2	1657.2	11508.5
	4 (18-24m)	15396.7	10578.1	1539.1	7125.4
	3 (12-18m)	2526.3	11586.0	0.0	0.0
	2 (6-12m)	2681.3	10816.6	0.0	0.0
	1 (0–6 m)	4733.4	10214.1	199.4	0.0
<b>4 – Hybrid CFRP+GFRP</b>	6 (30-36m)	17950.3	11875.7	1910.7	12268.7
	5 (24-30m)	17945.1	11113.5	1651.9	11471.5
	4 (18-24m)	16009.8	11024.1	1534.3	7103.1
	3 (12-18m)	3619.2	12111.3	0.0	0.0
	2 (6-12m)	3900.8	11376.9	0.0	0.0
	1 (0–6 m)	6666.3	10722.7	198.8	0.0
<b>5 – Full CFRP</b>	6 (30-36m)	17806.6	11119.5	1908.7	12256.5
	5 (24-30m)	17819.6	10724.5	1650.3	11460.4
	4 (18-24m)	15819.4	10586.8	1532.8	7096.3
	3 (12-18m)	3299.5	11494.2	0.0	0.0
	2 (6-12m)	3540.4	10790.0	0.0	0.0
	1 (0–6 m)	6051.3	10105.8	198.7	0.0

4.5.3. Iterative Design Modifications – Performance under SLS Combination

The results of the seven iterations are presented in this section, analysing displacement, tilt angle, stress, and total weight. Seven different FEM models were evaluated, considering both short-term properties and

long-term creep-reduced properties to assess their influence on tower performance. The resulting weights were compared against the steel reference tower weight of 3.77 t.

**Iteration 1 – GFRP ×4 Cross-Section and Thickness**

To increase global stiffness, the cross-sectional area and wall thickness of all primary members were scaled by a factor of four (Table 4.9). The governing SLS wind load was applied as summarised in Table 4.10. FEM analysis results for tip displacement are shown in Figure 4.6 with a value of 190.5 mm.

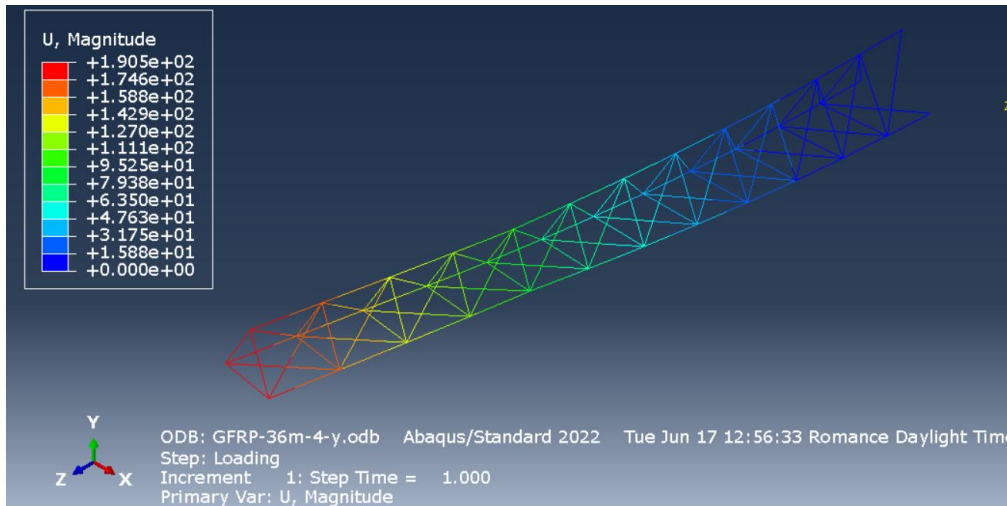


**Figure 4. 6:** Maximum tip displacement – iteration 1

Table 4.11 summarizes the main outcomes of Iteration 1. While the tilt angle requirement was satisfied, the total mass reached 9.94 t, which is approximately 2.64 times greater than the steel reference tower (3.77 t). This substantial increase in mass makes the configuration inefficient in terms of weight and cost, prompting the need for optimization in Iteration 2 to reduce excessive weight.

Both short-term (unreduced) and long-term (creep-reduced) material properties were analysed to assess the influence of creep on displacement and weight. While creep increased deflection, the overall conclusions remained unchanged.

**Table 4. 11:** Results from iteration 1

With long-term coefficient applied	Tip displacement (mm)	Tilt angle (°)	Axial Stress S11 (MPa)	Weight (T)
Yes	190.50	0.43	26.03	9.94
No	245.00	0.53	53.91	4.61

**Iteration 2 – GFRP ×3 Cross-Section and Thickness**

In this iteration, the cross-sectional area and wall thickness of all primary members were reduced from Iteration 1 to approximately three times the baseline GFRP dimensions.

Figure 4.7 shows the maximum tip displacement from the FEM analysis. Compared to Iteration 1, the total mass was reduced from 9.94 t to 6.64 t, while the tilt angle increased slightly but remained below the allowable  $0.66^\circ$  with a maximum displacement of 255.60 mm.

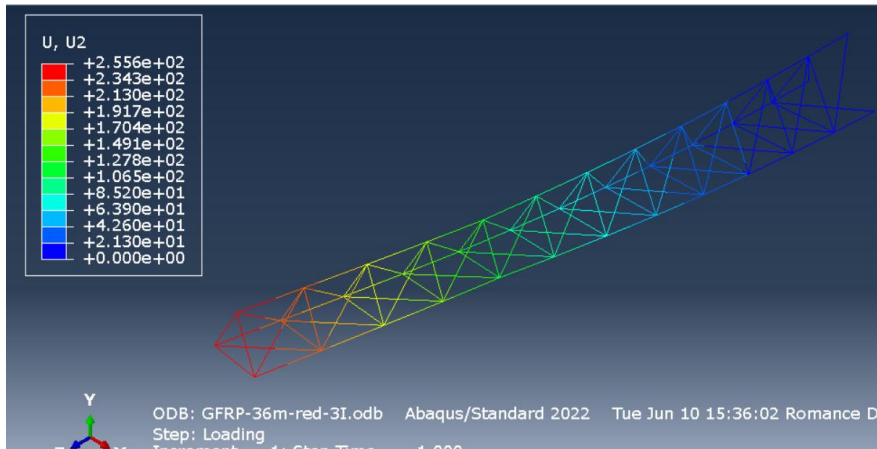


**Figure 4. 7:** Maximum tip displacement – iteration 2

Table 4.12 summarizes the results. Although mass was reduced by 33%, it remains significantly higher than the steel reference tower (3.77 t). Therefore, further optimization is required.

**Table 4. 12:** Results from iteration 2

With long-term coefficient applied	Tip displacement (mm)	Tilt angle (°)	Axial Stress S11 (MPa)	Weight (T)
Yes	255.6	0.55	42.8	6.64
No	245	0.53	32.63	5.09

### Iteration 3 – X-Bracing

In this iteration, the global stiffness of the tower was improved by introducing X-bracing with two diagonals per panel, replacing the single-diagonal configuration of the baseline GFRP model. Figure 4.8 shows the FEM displacement results under SLS loading with the long-term coefficient applied. The addition of double diagonals significantly improved lateral stiffness compared to the original GFRP design.

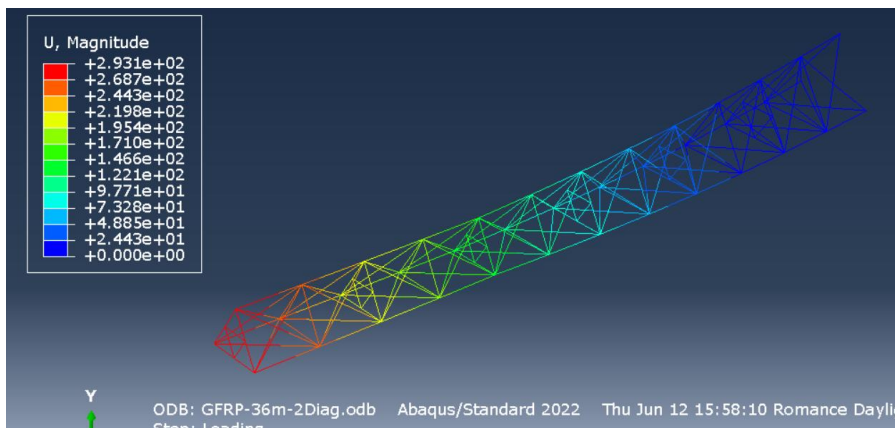


**Figure 4. 8:** Maximum tip displacement – iteration 3

Table 4.13 summarizes the results. The tilt angle was reduced to  $0.62^\circ$ , remaining below the  $0.66^\circ$  limit, and the total weight was 3.00 t – around 20 % lighter than the steel reference tower (3.77 t). Compared to Iteration 2, this modification increased stiffness without increasing weight, demonstrating the structural efficiency of optimised bracing patterns in GFRP lattice towers.

**Table 4. 13:** Results from iteration 3

With long-term coefficient applied	Tip displacement (mm)	Tilt angle ( $^\circ$ )	Axial Stress S11 (MPa)	Weight (T)
Yes	293.1	0.62	41.02	3.00

**Iteration 4 – Hybrid CFRP + GFRP Legs (Comparison with Steel Tower)**

This iteration maintained the same geometry and load conditions as the reference steel tower but replaced all leg members with CFRP while retaining GFRP for bracing and secondary members. The aim was to evaluate potential stiffness gains without modifying the structural layout.

Figure 4.9 shows the FEM displacement results under the SLS load case with the long-term coefficient applied.

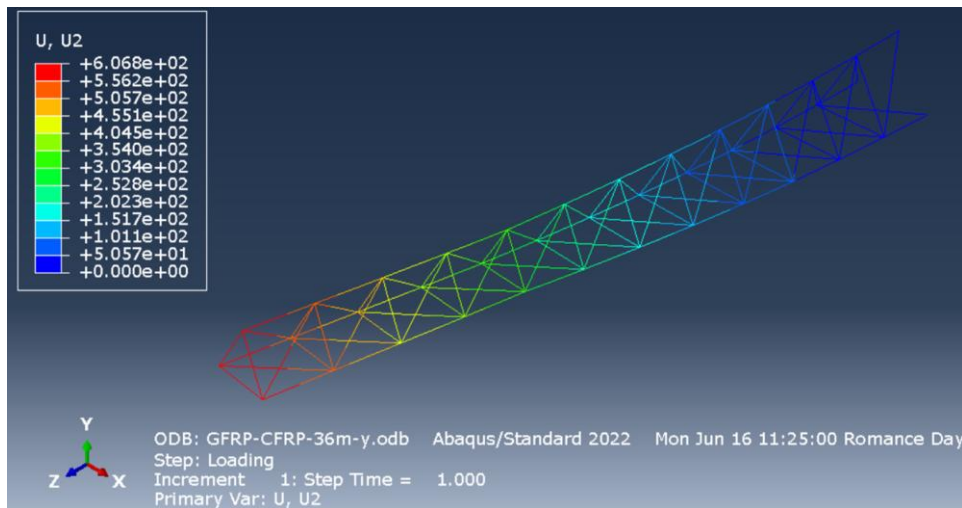


**Figure 4. 9:** Maximum tip displacement – iteration 4

As shown in Table 4.14, the hybrid configuration reduced the total weight to 0.813 t – nearly 80 % lighter than the steel reference. However, the tip displacement reached 606.8 mm, corresponding to a tilt angle of  $0.97^\circ$ , which exceeds the  $0.66^\circ$  serviceability limit.

**Table 4. 14:** Results from iteration 4

With long-term coefficient applied	Tip displacement (mm)	Tilt angle ( $^\circ$ )	Axial Stress S11 (MPa)	Weight (T)
Yes	293.1	0.62	41.02	3.00

### Iteration 5 – Hybrid Tower with CFRP Legs

In this iteration, the tower geometry was kept identical to the previous hybrid configuration, with an increased cross-section to meet the tilt angle requirements. The GFRP legs were replaced with CFRP, aiming to take advantage of its higher stiffness and strength in the main load-carrying members to reduce tip displacement and enhance the tower’s global stiffness, while keeping the weight within acceptable limits.

The mechanical properties of CFRP used in the FEM model are presented in Table 4.15. These were defined using engineering constants to account for the anisotropic nature of the composite material.

**Table 4. 15:** M1/Elium Carbon Mechanical Properties (CFRP) [94]

Properties		Units	Value without long-term coefficient	Value with long-term coefficient
Longitudinal tensile modulus	E11-t	MPa	154000.00	90588.24
Longitudinal compressive modulus	E11-c	MPa	142000.00	83529.41
Transverse tensile modulus	E22-t	MPa	7800.00	7800.00
Transverse compressive modulus	E22-c	MPa	9700.00	9700.00
Through-thickness tensile modulus	E33-t	MPa	7800.00	7800.00
Through-thickness compressive modulus	E33-c	MPa	9700.00	9700.00
Longitudinal tensile strength	f11,t	MPa	1060.00	1060.00
Longitudinal compressive strength	f11,c	MPa	795.00	795.00
Transverse tensile strength	f22,t	MPa	26.00	26.00
Transverse compressive strength	f22,c	MPa	115.00	115.00
Major Poisson’s ratio	v12	-	0.38	0.38
Poisson’s ratio	v23	-	0.39	0.39
In-plane shear strength	f12	MPa	42.00	42.00
In-plane shear modulus	G12	MPa	5500.00	1779.93
Shear strength in the 1–3 plane	f13	MPa	42.00	42.00
Shear modulus in the 1–3 plane	G13	MPa	5500.00	5500.00
Shear strength in the 2–3 plane	f23	MPa	21.00	21.00
Shear modulus in the 2–3	G23	MPa	2830.00	2830.00

The results from the FEM analysis, including the tip displacement distribution, are shown in Figure 4.10, with a tip displacement of 240.70 mm.

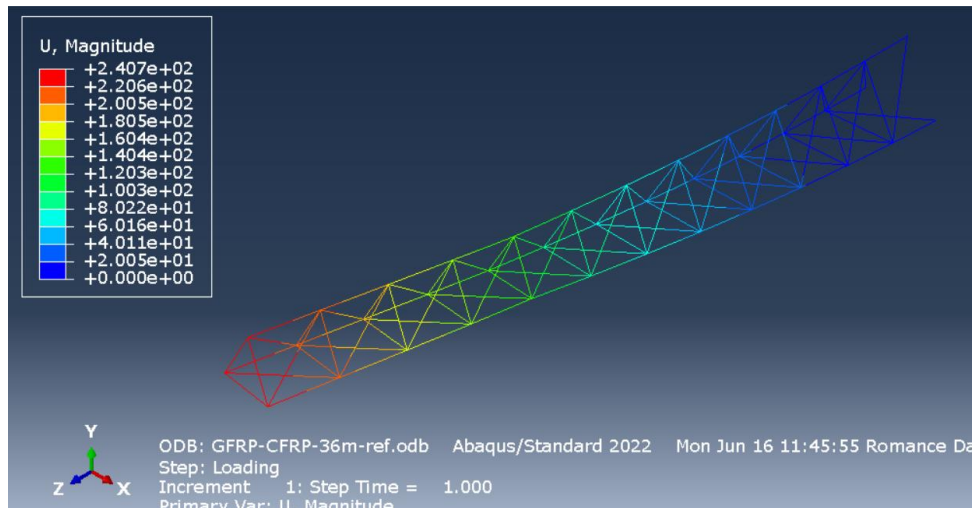


**Figure 4. 10:** Maximum tip displacement – iteration 4

As shown in Table 4.15 , replacing the legs with CFRP reduced tip displacement compared to the previous hybrid iteration and brought the tilt angle within serviceability limits. The tower weight was significantly reduced to 2.23 t, which is approximately 40% lighter than the steel reference (3.77 t). This iteration demonstrates that selective use of CFRP can effectively enhance stiffness without excessive weight penalty, although the cost implications of CFRP must be considered in later stages.

**Table 4. 16:** Results from iteration 5

With long-term coefficient applied	Tip displacement (mm)	Tilt angle (°)	Axial Stress S11 (MPa)	Weight (T)
Yes	240.70	0.53	438.20	2.23

**Iteration 6 – Full CFRP Configuration (Comparison with Steel Tower)**

In this iteration, the geometry and applied loads were identical to the reference steel tower; however, all members were modelled in CFRP. This step evaluated a full CFRP tower under identical conditions, aiming to maximise stiffness-to-weight ratio while greatly reducing mass.

The FEM analysis results are shown in Figure 4.11, with the corresponding numerical values summarized in Table 4.17. Compared to the steel reference, the full CFRP tower achieved a substantial weight reduction (0.768 t vs. 3.77 t) but exhibited increased tip displacement and tilt angle, indicating a trade-off between mass savings and global stiffness.

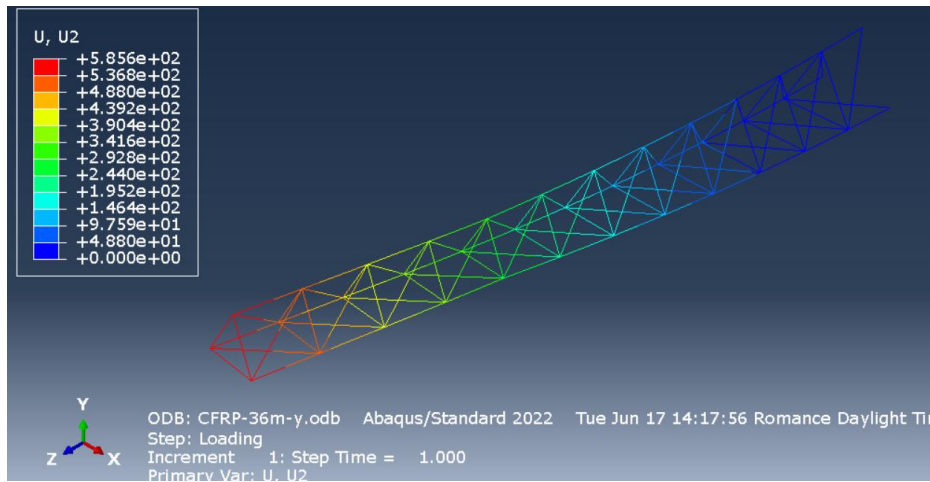


Figure 4. 11: Maximum tip displacement – iteration 6

Table 4. 17: Results from iteration 6

With long-term coefficient applied	Tip displacement (mm)	Tilt angle (°)	Axial Stress S11 (MPa)	Weight (T)
Yes	585.9	0.96	219.10	0.768
No	344.4	0.69	219.10	0.768

### Iteration 7 – Full CFRP Configuration

In the final iteration, the tower was simulated entirely from CFRP, with the cross-sectional dimensions of the primary members increased to meet stiffness requirements. This modification leveraged CFRP’s high stiffness-to-weight ratio, with the leg members—being the primary load-carrying elements—providing most of the global stiffness improvement. Compared to the previous hybrid tower, this configuration achieved a 44 % reduction in mass while also lowering axial stresses and satisfying the tilt angle limit.

Figure 4.12 presents the maximum tip displacement obtained from the FEM analysis under the governing SLS load scenario, while Table 4.18 summarizes the main results.

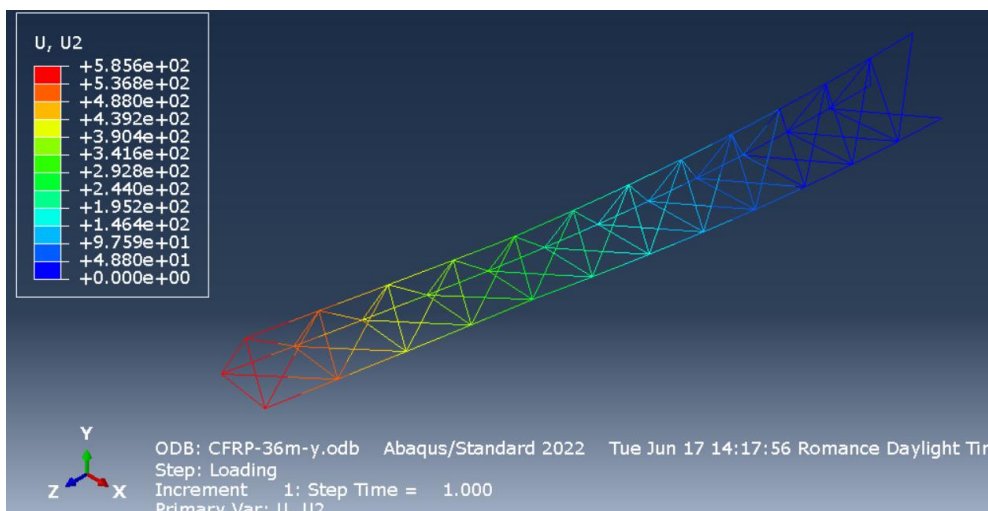


Figure 4. 12: Maximum tip displacement – iteration 7

**Table 4. 18:** Results from iteration 7

With long-term coefficient applied	Tip displacement (mm)	Tilt angle (°)	Axial Stress S11 (MPa)	Weight (T)
Yes	227.3	0.50	79.54	2.12

This configuration proved to be the most weight-efficient among all iterations, combining compliance with serviceability requirements and substantial mass savings compared to both the reference steel tower and the hybrid CFRP–GFRP design.

4.5.4. Comparative Summary and Conclusion

To conclude the first design loop, the performance of all seven iterations is presented in Table 4.19. The table summarizes the results presented in Section 4.5.3, enabling direct comparison of maximum tip displacement, tilt angle, axial stress, and total mass under the governing SLS load scenario (long-term coefficient applied).

**Table 4. 19:** Performance Summary of First Design Loop (SLS with Long-Term Coefficient Applied)

Iteration	Configuration	Tip Displacement (mm)	Tilt Angle (°)	Axial Stress S11 (MPa)	Weight (t)	Mass Reduction vs. Steel (%)
1	GFRP ×4 CS & t	190.5	0.43	26.03	9.94	–164% (heavier)
2	GFRP ×3 CS & t	255.6	0.55	42.8	6.64	–76% (heavier)
3	GFRP X-bracing	293.1	0.62	41.02	3	20% lighter
4	Hybrid CFRP legs + GFRP bracing	606.8	0.97	293.10*	0.813	78% lighter
5	Hybrid CFRP legs + GFRP bracing (increased dia./t)	240.7	0.53	438.2	2.23	41% lighter
6	Full CFRP (steel geometry)	585.9	0.96	219.1	0.768	80% lighter
7	Full CFRP (increased dia./t)	227.3	0.5	79.54	2.12	44% lighter

From the first design loop, the following conclusions can be drawn:

- **Pure GFRP designs (Iterations 1–2):** Although stiffness can be improved by increasing cross-section size or modifying bracing patterns, achieving steel-like serviceability performance results in excessive mass, well above the steel reference (3.77 t).
- **X-bracing (Iteration 3):** Provided a notable stiffness gain without a significant mass penalty, highlighting the efficiency of bracing optimization.

- **Hybrid designs (Iterations 4–5):** Introducing CFRP into critical load-carrying members significantly improves stiffness-to-weight ratio. Increasing member sizes in the hybrid design (Iteration 5) achieved tilt angle compliance with a 40% weight reduction compared to steel.
- **Full CFRP designs (Iterations 6–7):** The same geometry as steel (Iteration 6) produced very low mass but excessive deflections. Increasing cross-sections (Iteration 7) reduced displacement below the steel reference, lowered axial stresses, and achieved the highest stiffness-to-weight efficiency, with a 44% mass reduction relative to steel.

The results indicate that achieving serviceability compliance using GFRP pipes alone is challenging without incurring a significant weight penalty. Reconfiguring the tower to increase the number of diagonals can improve stiffness, but the most effective approach identified in this study was the strategic use of CFRP—either in hybrid or full configurations—to meet stiffness requirements while reducing mass.

The most balanced design was Iteration 7, a full CFRP tower with increased cross-sections, which satisfied tilt angle limits, reduced axial stresses, and achieved substantial mass savings. However, the high cost of CFRP remains a critical factor for practical implementation.

For this reason, the second design loop will focus on reconfiguring the tower geometry—exploring different shapes and diagonal arrangements—to better exploit the mechanical properties of GFRP in the fibre direction.

## 5. SECOND DESIGN LOOP

### 5.1. Objective

The second design loop aimed to explore the influence of base geometry and bracing configuration on the stiffness efficiency of FRP lattice towers before committing to full-scale modelling. A parametric comparative study was performed using small-scale prototype models, enabling rapid evaluation of geometric alternatives while limiting computational and modelling complexity.

Three base geometries were considered: triangular, square, and hexagonal trusses. For each geometry, multiple bracing configurations were analysed, progressively increasing the number of structural elements to assess their impact on stiffness. Initial configurations consisted of a single diagonal per section, followed by two diagonals, horizontal members, and finally internal diagonals.

### 5.2. Setup

#### 5.2.1. Geometry

The first step involved designing small-scale trusses (3 m height) with bases circumscribed in a 2 m diameter circle. For each geometry, bracing density was increased in stages:

1. Single diagonal per face.
2. Multiple diagonals per face.
3. Addition of horizontal bracing at 1.5 m intervals.
4. Inclusion of internal diagonals within each panel.

Figure 5.1 illustrates the progressive bracing schemes for the triangular, square, and hexagonal bases.

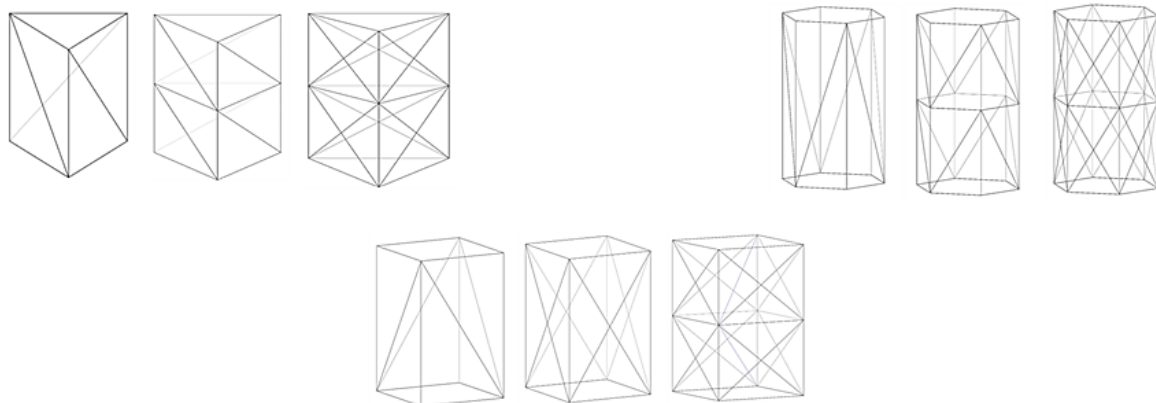


**Figure 5. 1:** Bracing configurations for triangular, square, and hexagonal prototypes

All members in the prototype models were GFRP circular hollow sections with the same material properties described in Table 3.4. Member dimensions were as follows:

- Legs:  $\text{Ø}140 \times 8 \text{ mm}$
- Horizontal members:  $\text{Ø}120 \times 8 \text{ mm}$
- Diagonals:  $\text{Ø}70 \times 8 \text{ mm}$

### 5.2.2. Load Cases and Boundary Conditions

For all small-scale prototypes, the base was modelled as clamped, restricting all translational degrees of freedom while allowing rotation. The applied load cases were derived from a section of the 36 m reference tower, with the following magnitudes:

- Dead load: 17,611 N applied in the  $-Z$  direction.
- Operational load: 9,960 N applied in the  $-Z$  direction.
- Total wind load: 23,869.4 N applied in the  $+Y$  direction.

All loads were applied to a reference point located at the geometric centre of the tower plan (i.e., the centre of the inscribed circle). This approach ensured a consistent and comparable load introduction across all geometries, avoiding variations in load distribution caused by differences in member arrangement. It also facilitated direct measurement of global structural response (displacement and stress) for performance comparison. Figure 5.2 illustrates the load application scheme.

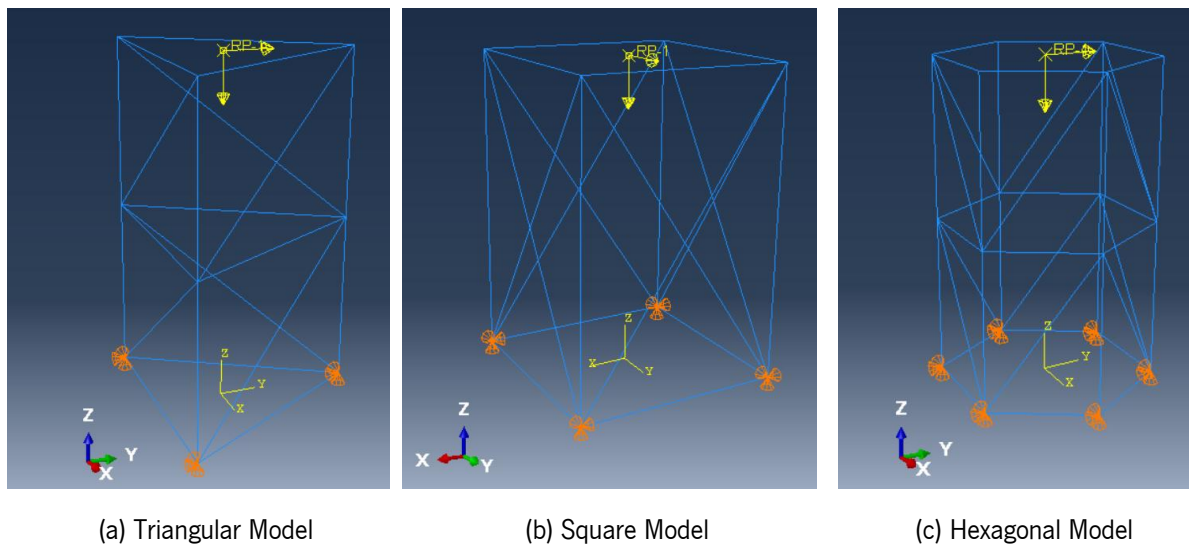


**Figure 5. 2:** Load application setup in prototype models (reference point)

### 5.3. Results and Selection of Small-Scale Prototypes

In total, 20 models were generated. For each configuration, the following results were recorded: maximum axial stress ( $S_{11}$ ), maximum tip displacement ( $U_2$ ), and total weight. From these values, the specific displacement (mm/t) and specific strength (MPa/t) were calculated. The complete results are presented in Table 5.1.

**Table 5. 1:** Summary of Prototype-Scale Tower Models and Performance Metrics

Model	Base Type	# Diagonals	# Divisions	# Diagonals /section	Max $S_{11}$ (MPa)	Max $\delta$ (mm)	Weight (Ton)	Specific displacement (mm/Ton)	Specific strength MPa/Ton
1	T <sup>1</sup>	3	1	0	16.5	5.0	0.1	34.6	113.6
2	T	6	1	0	12.0	3.8	0.2	20.6	64.3
3	T	3	2	3	12.4	3.5	0.2	15.4	54.7
4	T	3	2	0	12.0	3.8	0.2	16.2	51.0
5	T	6	2	0	11.3	2.0	0.2	8.9	49.3
1	H <sup>2</sup>	6	1	0	15.8	4.8	0.2	21.8	71.3
2	H	12	2	0	9.1	2.3	0.3	8.8	35.2
3	H	24	2	0	5.8	1.3	0.3	4.1	18.0
4	H	12	1	0	9.4	2.6	0.3	9.5	34.2
5	H	12	1	3	7.0	1.7	0.3	5.6	22.8
6	H	24	2	1	5.3	1.2	0.3	3.5	15.6
7	H	24	2	2	5.1	1.1	0.3	3.1	14.7
8	H	24	2	3	4.7	1.1	0.4	3.0	13.0
1	S <sup>3</sup>	4	1	0	14.6	3.3	0.2	17.1	75.4
2	S	4	1	0	14.2	3.2	0.2	16.5	73.5
3	S	8	1	0	7.8	1.6	0.2	6.9	33.2
4	S	8	2	0	9.8	2.4	0.2	9.7	39.2
5	S	16	2	0	6.3	1.3	0.3	4.2	20.6
6	S	16	2	1	5.9	1.2	0.3	3.7	18.2
7	S	16	2	2	6.4	1.1	0.3	3.3	18.7

1: T-Triangular, 2: H-Hexagonal, 3: S-Square

To facilitate interpretation, the results were plotted by base geometry. Figure 5.3 shows the specific displacement for the triangular geometry configurations. In this case, Model 5, with a specific displacement of 8.861 mm/t, featuring X-bracing and horizontal divisions every 1,500 mm, was selected for subsequent scaling to the 36 m tower.

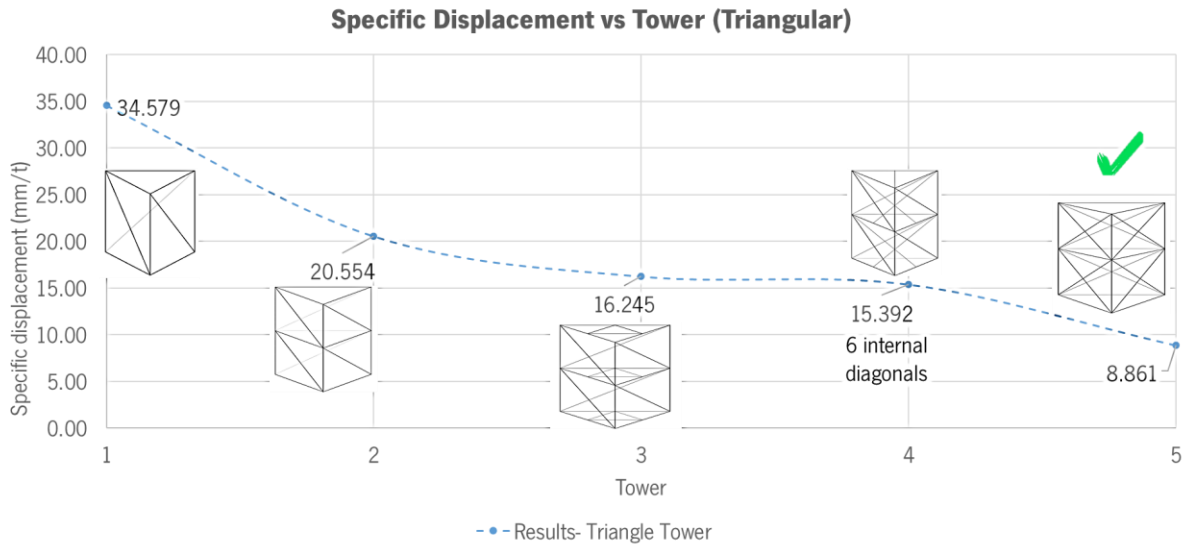


**Figure 5. 3:** Specific displacement results for triangular geometry models

For the square geometry, Figure 5.4 presents the specific displacement results. Two configurations were selected for scaling: Model 5, with a specific displacement of 4.227 mm/t, and Model 7, with a value of 3.304 mm/t. Model 5 features X-bracing with horizontal members every 1,500 mm, while Model 7 incorporates four internal diagonals per section. Although the square geometry generally provides greater stiffness than the triangular configuration, it requires a higher material volume, which increases total weight.

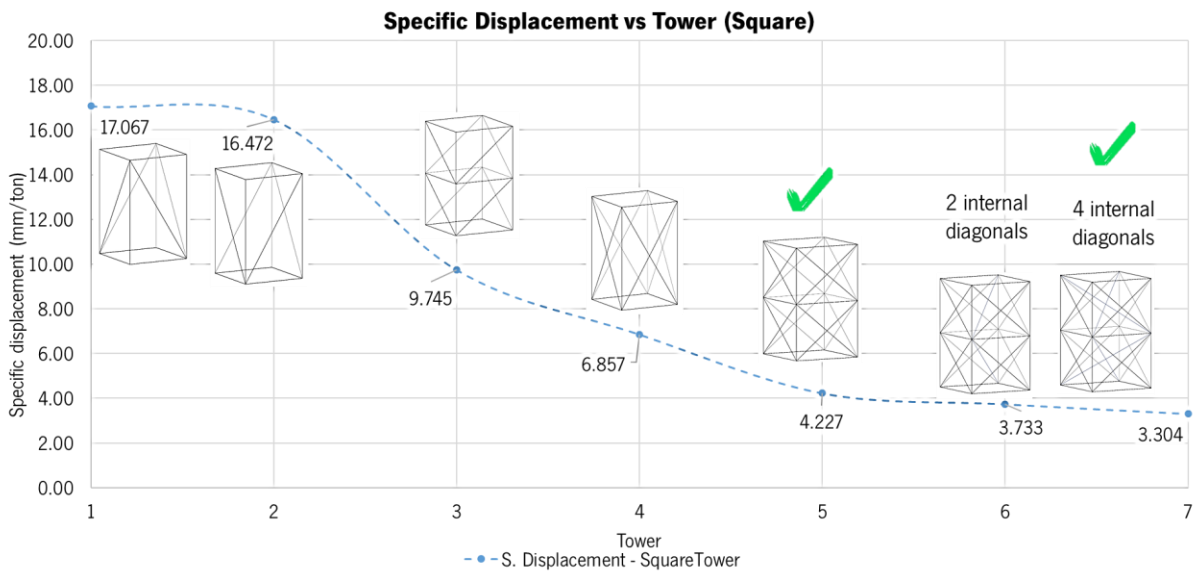


**Figure 5. 4:** Specific displacement results for square geometry models

For the hexagonal geometry, Figure 5.5 shows the specific displacement ranking. Three configurations were selected: Model 5 (4.080 mm/t), Model 7 (3.103 mm/t), and Model 8 (2.983 mm/t). Model 5 has X-bracing with horizontals at 1.5 m spacing, Model 7 includes four internal diagonals, and Model 8 features six internal diagonals per section.

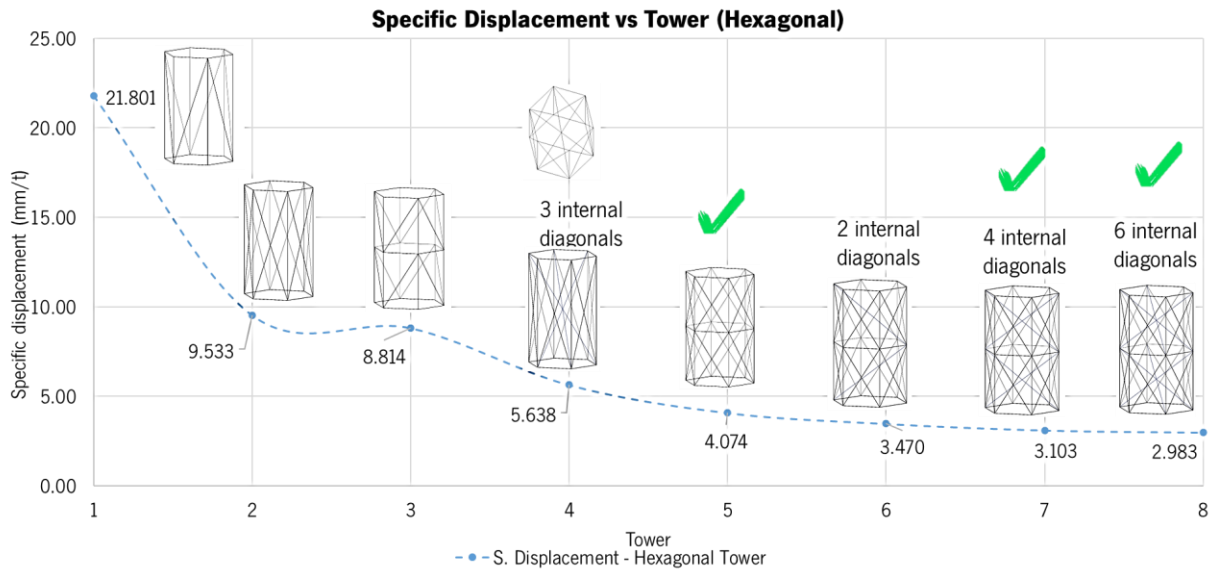


**Figure 5. 5:** Specific displacement results for hexagonal geometry models

The comparative plots for triangular, square, and hexagonal geometries clearly show that increasing bracing density and horizontal divisions improves stiffness-to-weight efficiency. Based on the lowest specific displacement values for each geometry, the selected models were advanced to the scaling phase for full 36 m tower modelling

#### 5.4. Scaling to 36 m Tower

The five selected prototypes were scaled to a full 36 m-high tower made from GFRP pultruded profiles, divided into six sections, with braces and horizontal members spaced every 1,500 mm. Two structural layouts were analysed in this stage: non-tapered, with a constant cross-section along the full height, and tapered, with a reduced and constant base dimension in the last two sections.

##### *Non-Tapered Towers*

Each selected configuration was scaled to a 36 m tower, subdivided into six 6 m sections. The five selected configurations were modelled in the FEM analysis with a base dimension of 3 m (circumscribed diameter). All members were represented as GFRP circular hollow sections, using the same material properties defined earlier: legs with  $\text{Ø}140 \times 8$  mm pipes, horizontals with  $\text{Ø}120 \times 8$  mm pipes, and diagonals with  $\text{Ø}70 \times 8$  mm pipes. Three of these models are shown in Figure 5.6

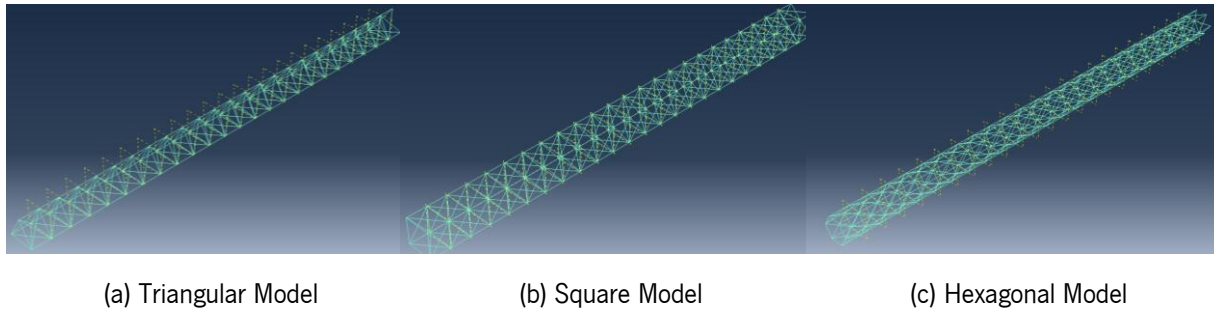


**Figure 5. 6:** Non-Tapered 36 m Tower Configuration

Loads were determined following the same procedure described in Section 3.3 (Load Definition – Methodology), accounting for self-weight, wind loads on the structure and equipment, and operational loads, combined according to the adopted load cases. Wind incidence angles were set at  $90^\circ$  to one face for the triangular model,  $90^\circ$  and  $45^\circ$  for the square model, and  $90^\circ$  (three-face impact) for the hexagonal model, as shown in Figure 5.7. Detailed per-section load magnitudes are provided in Annex B.

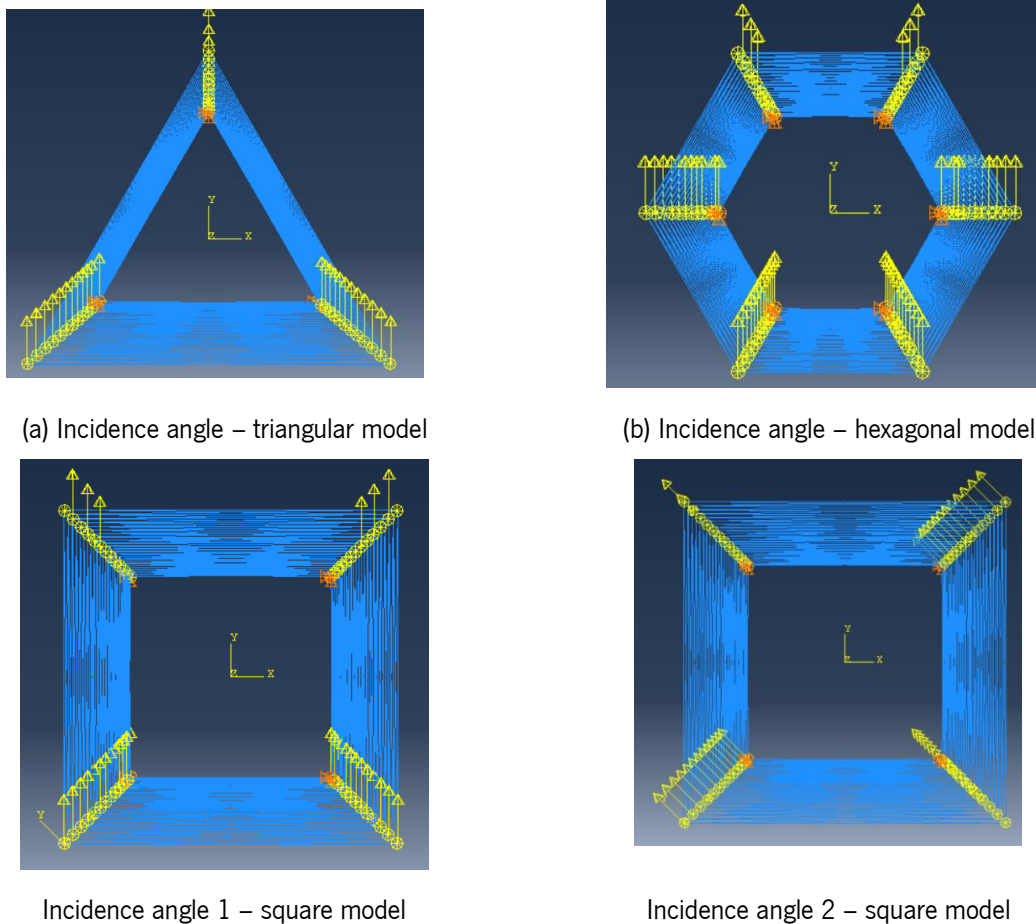


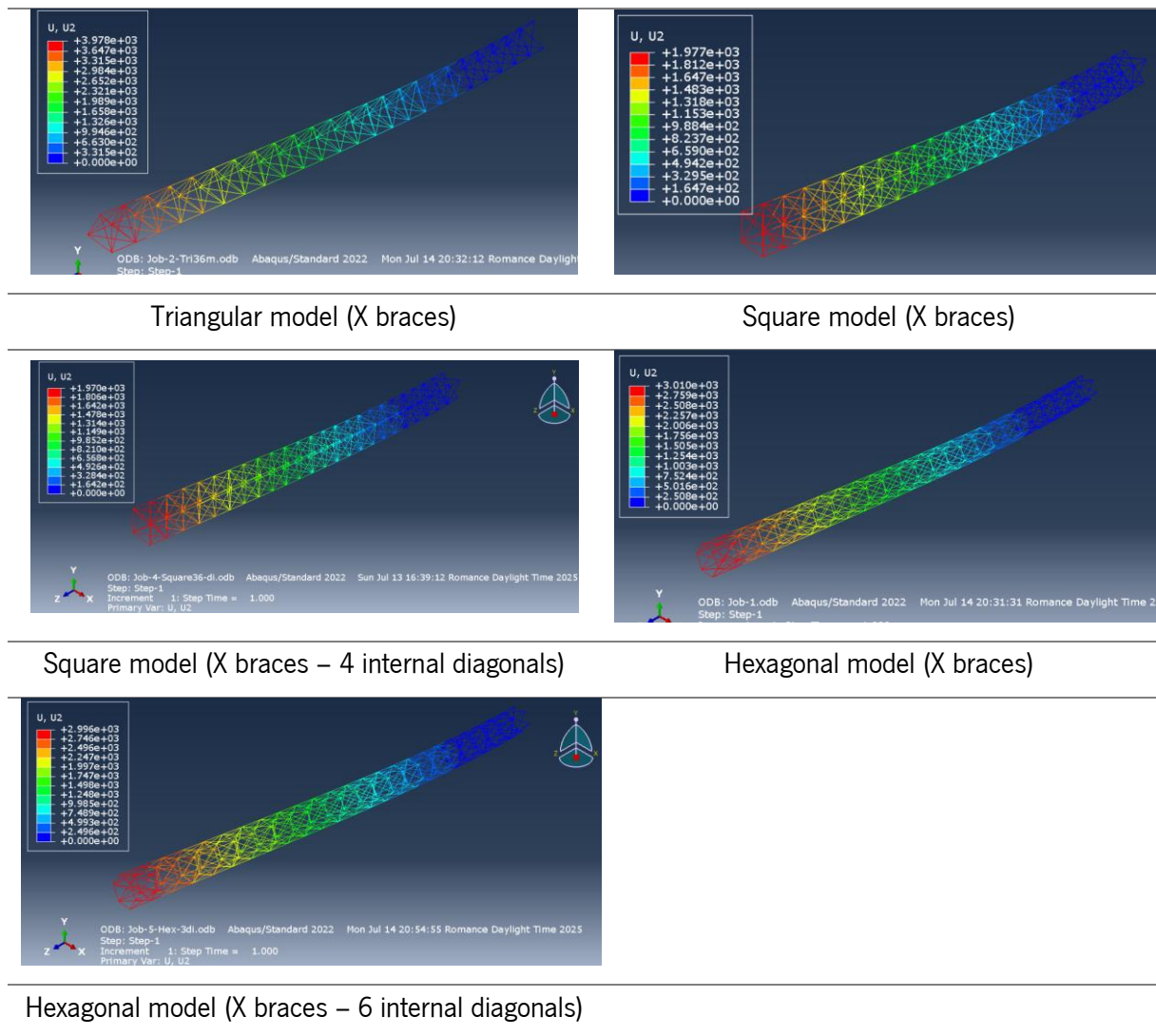
**Figure 5. 7:** Loads and wind incidence angles

**Results – Non-Tapered Towers**

The displacements obtained from the models are presented in Table 5.2. The triangular tower exhibited the highest tip displacement at 3978 mm, while the square tower showed the lowest displacements—1977 mm without internal diagonals and 1970 mm with internal diagonals—indicating a superior stiffness-to-weight ratio. The hexagonal tower recorded 3010 mm without internal diagonals and 2996 mm with internal diagonals, which may be attributed to the larger projected area subjected to wind load (three faces).

**Table 5. 2:** Non-tapered 36 m tower displacement results for selected geometries.

**Displacement (U2) of the non-tapered towers**



The displacement, stress, weight, and specific displacement results for the non-tapered configurations are summarized in Table 5.3. While the square models achieved the lowest specific displacement values (621.89 mm/t and 545.70 mm/t with and without internal diagonals), the triangular tower recorded the

highest (1668.44 mm/t), highlighting its comparatively poor stiffness-to-weight performance. The hexagonal models fell in between, with moderate displacements and specific displacement values (866.01–752.65 mm/t), though slightly higher weights due to their geometry. Given these results, the triangular geometry was excluded from further study, and only square and hexagonal configurations—both with and without internal diagonals—were selected for tapered tower analysis.

**Table 5. 3:** Structural performance of non-tapered 36 m tower configurations

<b>N</b>	<b>Type</b>	<b>Displacement U2 (mm)</b>	<b>Tilt angle</b>	<b>Stress S11(MPa)</b>	<b>Weight (t)</b>	<b>Specific displacement (mm/t)</b>
1	Triangular	3978	1.47	403.3	2.384	1668.44
2	Hexagonal	3010	1.43	238.5	3.475	866.01
3	Hexagonal internal diagonals	2996	1.43	242.5	3.980	752.65
4	Square	1977	1.36	189.2	3.179	621.89
5	Square internal diagonals	1970	1.36	190.9	3.610	545.7

### 5.5. Scaling to 36 m – Tapered Designs

Following the non-tapered tower analysis, the square and hexagonal configurations—both with and without internal diagonals—were selected for further study in tapered form. In the hexagonal models, the base dimension was maintained at 3 m for the lower four sections, while the upper two sections had a reduced base of 1.2 m. For the square models, two variants were considered:

- Base 3 m for the lower four sections, reduced to 1.2 m in the upper two.
- Base 4 m for the lower four sections, reduced to 2 m in the upper two.

This reduced base dimension (tapered configuration) aimed to improve stiffness-to-weight performance and reduce the wind-exposed area.

All members were modelled as GFRP circular hollow sections, using the same material properties defined earlier. A schematic of the tapered tower geometry and member arrangement is presented in Figure 5.8.

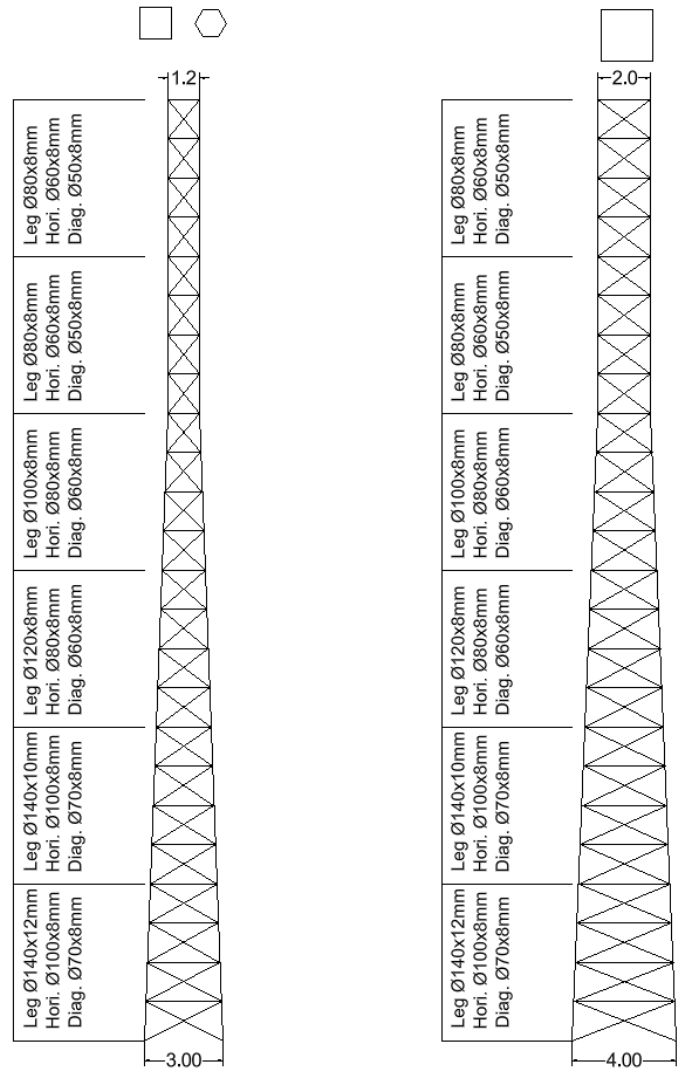


Figure 5. 8: Tapered tower geometry

Loads were determined following the same methodology as in Section 3.3 (Load Definition – Methodology), with wind incidence angles matching those used in the non-tapered analysis. Full per-section load magnitudes are provided in Annex B.

**Results – Tapered Towers**

The five models were analysed in Abaqus, and the tip displacement—used as a measure of stiffness—was computed for each case. Results are presented in Table 5.4, where the square model with a 4 m to 2 m tapered base achieved the lowest tip displacement at 655.8 mm. It can also be observed that the inclusion of internal diagonals consistently produced only minimal reductions in displacement.

**Table 5. 4:** Tapered 36 m tower displacement results for selected geometries.

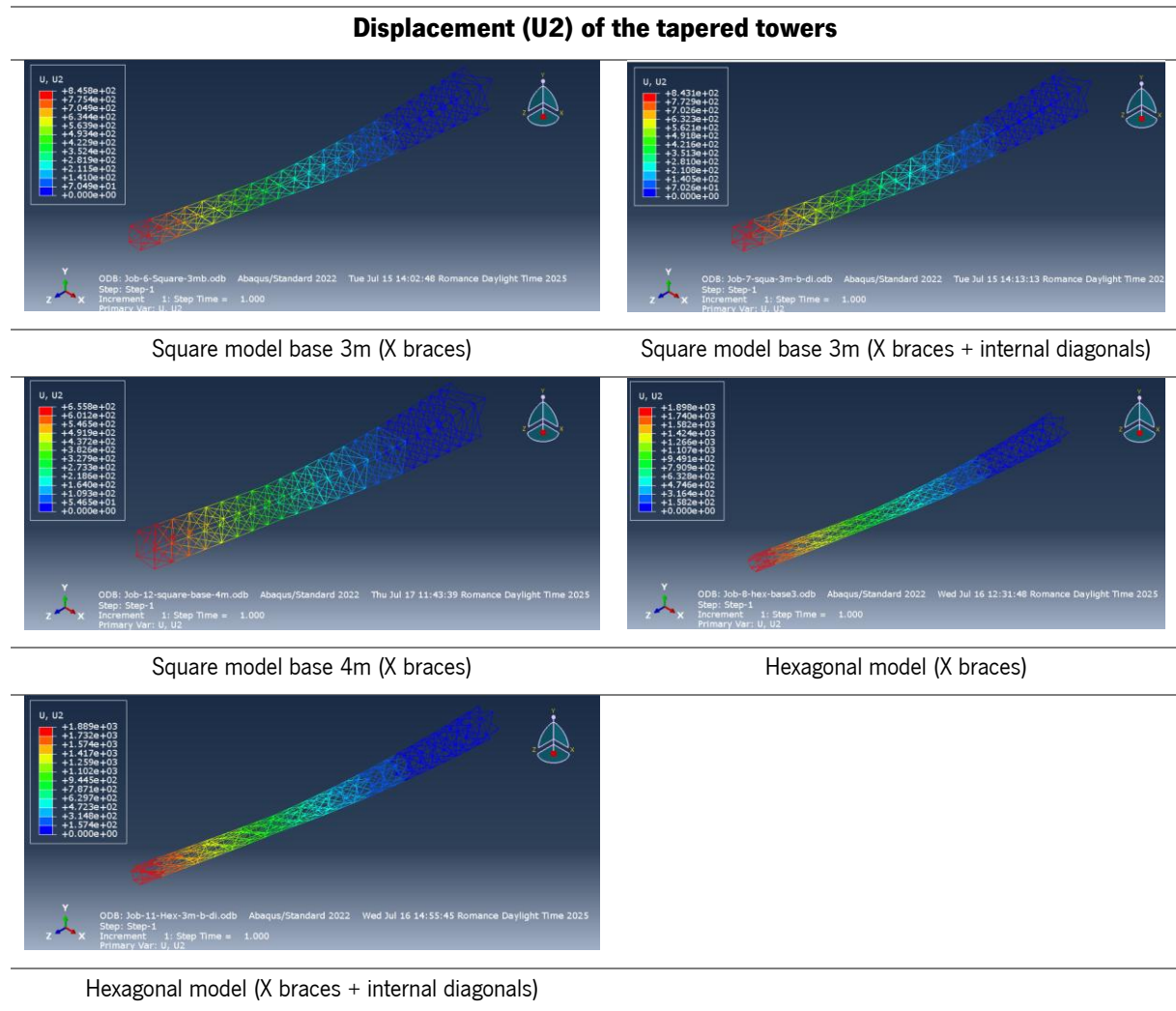


Table 5.5 presents the FEM results for the five tapered tower models, including tip displacement ( $u_2$ ), tilt angle, maximum axial stress ( $S_{11}$ ), total weight, and specific displacement. Compared to their non-tapered counterparts, these designs achieved displacement reductions exceeding 50% in some cases, primarily due to the decreased projected area exposed to wind loads.

**Table 5. 5:** Structural performance of tapered 36 m tower configurations

N	Type	Deformation $u_2$ (mm)	Tilt angle	Stress $S_{11}$ (MPa)	Weight (Ton)	Specific deformation (mm/Ton)
1	Hexagon model 3m-1.2m	1898	1.36	111.3	2.799	678.01
2	Hexagon model 3m-1.2m with internal diagonals	1889	1.35	112.3	3.275	576.65

3	Square 3 m -1.2 m base	845.8	1.12	57.52	2.585	327.08
4	Square 3 m -1.2 m base with internal diagonals	843.1	1.11	57.93	3.315	254.31
5	Square 4 m -2 m base	655.8	1.01	69.39	2.941	222.91

The square model with a 4 m to 2 m tapered base achieved the lowest tip displacement at 655.8 mm and a specific displacement of 222.91 mm/t, confirming its superior stiffness-to-weight performance among all configurations. The square 3 m to 1.2 m model also demonstrated good stiffness, with displacements of approximately 845 mm. In contrast, the hexagonal models exhibited higher displacements, around 1890 mm, although these still represented substantial improvements over their non-tapered counterparts due to the reduced projected area.

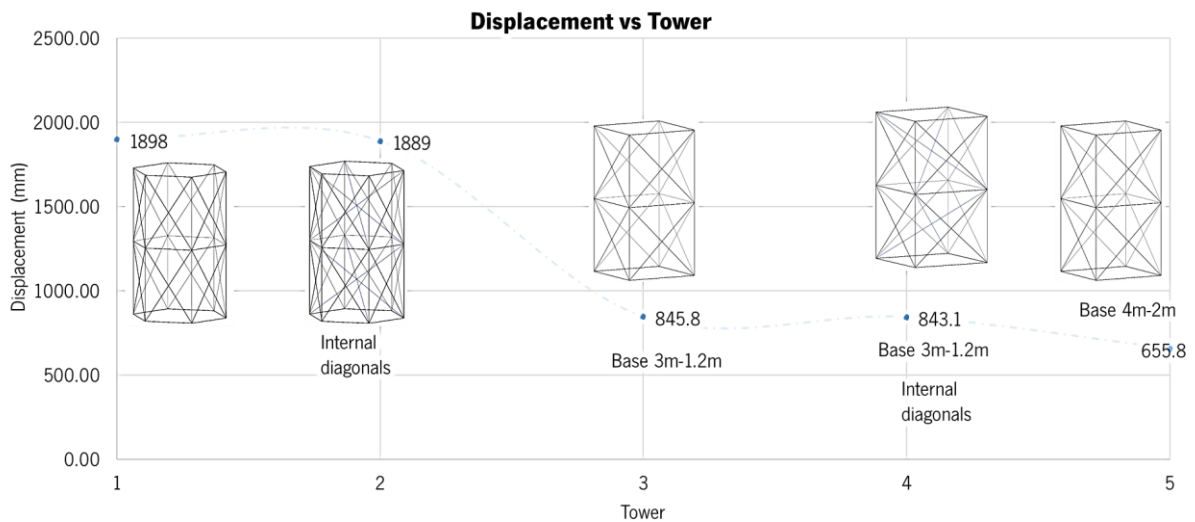


**Figure 5. 9:** Results of the tapered geometry

Figure 5.9 provides a visual comparison of all tapered tower designs, clearly illustrating the performance gap between geometries. The square configurations consistently outperformed the hexagonal ones, while the effect of internal diagonals on stiffness was minimal. This reinforces the conclusion that base dimension and overall geometry have a more significant impact on structural performance than additional internal bracing in these designs.

## 5.6. Discussion and Design Implications

The second design loop explored the influence of geometry, bracing configuration, and tapering on the stiffness-to-weight performance of GFRP telecommunication towers. Prototype-scale analyses allowed to explore other configurations, which were subsequently scaled to full 36 m tower models for both non-tapered and tapered geometries. Results clearly showed that base dimension and overall geometry had a stronger influence on displacement performance than additional internal bracing. While internal diagonals provided minimum stiffness gains, the associated weight increase reduced specific performance, making their inclusion less advantageous in most cases.

For non-tapered towers, the square geometry consistently outperformed both hexagonal and triangular arrangements in terms of displacement and specific stiffness. The triangular model recorded the highest tip displacement (3978 mm), making it unsuitable for further tapered optimisation. Hexagonal configurations, while performing better than triangular ones, still exhibited significantly larger displacements than square models, likely due to the greater projected area exposed to wind loads.

The tapered designs demonstrated the potential of geometric optimisation to improve structural efficiency. By reducing the top section dimensions, the wind-exposed area was decreased, leading to displacement reductions exceeding 50% in some cases compared to non-tapered equivalents. Among all tapered models, the square 4 m to 2 m base configuration achieved the lowest displacement (655.8 mm) and best specific stiffness (222.91 mm/t), confirming its superior geometry for stiffness-to-weight optimisation.

Despite these geometric improvements, none of the tapered GFRP configurations met the serviceability limit state (SLS) displacement and tilt angle requirements under the current load assumptions. This highlights a fundamental limitation in relying solely on geometry modifications when using GFRP for tall self-supporting towers. Two potential strategies could address this:

1. Material optimisation, particularly substituting GFRP with CFRP, which offers significantly higher stiffness and strength while maintaining low weight.
2. Load reduction measures, such as lighter antenna equipment or aerodynamic shielding to lower wind forces, thereby reducing service loads.
3. Re-evaluating allowable deformation limits for specific applications where serviceability criteria can be relaxed without compromising operational performance or safety.

However, heavily braced configurations—especially those with internal diagonals—introduce manufacturing complexity and cost escalation due to intricate joint designs, especially for pultruded profiles designs. This raises concerns about economic feasibility, particularly for large-scale production

and installation. Therefore, the most promising pathway appears to be a combined strategy of moderate geometric optimisation with material substitution, rather than pursuing increasingly complex bracing patterns.

The relevance of the first design loop results becomes apparent in this context. CFRP Z-bracing achieved a displacement of 227.3 mm at a total weight of 2.12 t (44% lighter than steel), while GFRP X-bracing recorded 293.1 mm at 3.0 t (20% lighter than steel). These configurations suggest that targeted material changes can yield substantial performance gains without the drawbacks of excessive geometric complexity.

### 5.7. ULS Verification

ULS Verification was carried out for the first design loop GFRP X-bracing tower, selected as the most critical configuration due to its lower mechanical properties compared to the CFRP alternative. The characteristic mechanical properties were first determined, and following the procedure outlined in Section 3.6 of the methodology, the following verifications were performed:

- Axial tension
- Axial compression
- Bending
- Shear

The design actions for each check were obtained from the Abaqus model by analysing the most critical cross-section in each tower segment. The verification results for the main members are summarised in Table 5.6.

**Table 5. 6:** Structural verification of main members – legs, X-bracing GFRP tower

Parameter	Units		Section 1	Section 2	Section 3	Section 4	Section 5	Section 6
<b>Axial Tension</b>								
Design value tensile strength	$f_{x,t,d}$	MPa	439.3	439.3	439.3	439.3	439.3	439.3
Area - cross section	A	mm <sup>2</sup>	8904.5	10300.7	11384.8	13841.7	13841.7	20615.4
Design value of tensile resistance	$N_{t,Rd}$	kN	3911.8	4525.1	5001.4	6080.7	6080.7	9056.5
Design action tensile	$N_{t,Ed}$	kN	16.6	80.9	166.1	282.3	347.4	427.4
Verification $N_{t,Ed} < N_{t,Rd}$	-	-	Ok	Ok	Ok	Ok	Ok	Ok
<b>Axial Compression</b>								
Design value of the compressive resistance to crushing	$N_{c,Rd1}$	kN	2412.1	2790.3	3084.0	3749.6	3749.6	5584.5
Char. value of the critical stress associated to local buckling	$f_{x,cr,k}$	MPa	346.0	407.1	368.4	303.0	303.0	265.7
Design value of the compressive resistance to local buckling	$N_{cr,Rd}$	kN	1209.3	1645.9	1645.9	1645.9	1645.9	2149.8

## Chapter 5 | Second Design Loop

Characteristic value of the critical flexural buckling stress	f <sub>E,cr,k</sub>	MPa	77.0	75.8	92.5	136.6	136.6	231.9
Design value of the flexural buckling	NE,Rd	kN	410.7	467.8	626.4	1102.2	1102.2	2671.8
Reduction factor - flexural buckling	XE	-	0.3	0.3	0.3	0.5	0.5	0.7
Design value of the compressive resistance to global buckling of the cross section	N <sub>c,Rd2</sub>	kN	358.0	418.0	535.8	818.7	818.7	1490.9
Design value of compressive resistance - cross section	N <sub>c,Rd</sub>	kN	358.0	418.0	535.8	818.7	818.7	1490.9
Design action compression	N <sub>t,Ed</sub>	kN	56.8	209.7	405.2	646.0	778.8	944.1
<b>Verification N<sub>c,Ed</sub>&lt;N<sub>t,Rd</sub></b>			Ok	Ok	Ok	Ok	Ok	Ok
<b>Bending</b>								
Bending moment resistance	MR <sub>d,1</sub>	kNm	135.9	154.7	189.9	283.0	283.0	551.9
Char. value of the critical stress - local buckling of the profile in bending	f <sub>x,b,cr,k</sub>	MPa	519.0	610.7	552.6	454.5	454.5	398.6
Bending moment resistance to local buckling	M <sub>cr,Rd</sub>	kNm	102.2	136.9	152.0	186.3	186.3	318.7
Char. Value of the lateral-torsional buckling resistance	FL <sub>T,cr,k</sub>	MPa	1.5	1.5	1.7	2.0	2.0	2.6
Design value of the bending moment resistance to lateral-torsional buckling	ML <sub>T,Rd</sub>	kNm	0.5	0.5	0.7	1.3	1.3	3.3
Design value of the bending moment - global buckling	MR <sub>d,2</sub>	kNm	1.0	1.1	1.5	2.6	2.6	6.6
Design action bending moment	M <sub>Ed</sub>	kNm	0.1	0.4	0.7	0.7	1.7	3.4
<b>Verification M<sub>Ed</sub>&lt;M<sub>Rd</sub></b>			Ok	Ok	Ok	Ok	Ok	Ok
<b>Shear</b>								
Characteristic Value of the in-plane shear strength	f <sub>xy,v,k</sub>	MPa	4889.8	4889.8	4889.8	4889.8	4889.8	4889.8
Shear area	A <sub>v</sub>	mm <sup>2</sup>	4565.4	5304.3	5846.3	7074.8	7074.8	10508.8
Design value of the shear resistance to material failure	V <sub>Rd,1</sub>	kN	11019.3	12802.7	14111.1	17076.2	17076.2	25364.7
Design action shear	V <sub>Ed</sub>	kN	0.0	0.1	0.2	0.3	0.2	0.7
<b>Verification V<sub>Ed</sub>&lt;V<sub>Rd</sub></b>			Ok	Ok	Ok	Ok	Ok	Ok

All main members of the GFRP X-bracing tower satisfied the ULS verification requirements for axial, bending, and shear actions across all sections. The most critical checks were observed in compression, particularly in Sections 3–5, but still remained within the allowable design limits. Bending and shear demands were significantly lower than the corresponding resistances, indicating that the structural performance is governed primarily by axial compression rather than flexural or shear capacity.

Following the same verification procedure, the secondary members – specifically the horizontal and diagonal elements – were checked for Ultimate Limit State (ULS) compliance. Table 5.7 presents the summary of results for the diagonal members of the GFRP X-bracing tower.

**Table 5. 7:** Structural verification of diagonals – X-bracing GFRP tower

	Units	Section 1	Section 2	Section 3	Section 4	Section 5	Section 6
<b>Axial Tension Verification</b>							
Design tensile resistance, $N_{t,Rd}$	kN	1236.6	1567.8	1567.8	1567.8	1567.8	1567.8
Design action, $N_{t,Ed}$	kN	12.8	21.9	21.5	22.4	25.9	34.7
Verification $N_{t,Ed} < N_{t,Rd}$	-	Ok	Ok	Ok	Ok	Ok	Ok
<b>Axial Compression Verification</b>							
Governing compressive resistance, $N_{c,Rd}$	kN	79.7	149.4	151.3	140.5	125.9	118.7
Design action, $N_{c,Ed}$	kN	20.5	42.6	47.3	49.0	49.4	54.2
Verification $N_{c,Ed} < N_{c,Rd}$	-	Ok	Ok	Ok	Ok	Ok	Ok
<b>Bending Verification</b>							
Bending moment resistance, $M_{Rd}$	kNm	20.0	32.6	32.6	32.6	32.6	32.6
Design action, $M_{Ed}$	kNm	0.1	0.4	0.7	0.7	1.7	3.4
Verification $M_{Ed} < M_{Rd}$	-	Ok	Ok	Ok	Ok	Ok	Ok
<b>Shear Verification</b>							
Shear resistance, $V_{Rd}$	kN	3518.4	4428.3	4428.3	4428.3	4428.3	4428.3
Design action, $V_{Ed}$	kN	0.04	0.2	0.3	0.2	0.3	0.3
Verification $V_{Ed} < V_{Rd}$	-	Ok	Ok	Ok	Ok	Ok	Ok

All diagonal members satisfied the ULS requirements for axial tension, axial compression, bending, and shear across all sections. The most critical verifications were in compression, particularly in Sections 3–6, where design actions approached a higher proportion of the available resistance. However, adequate safety margins were maintained in all cases and bending and shear demands were negligible compared to their respective resistances, confirming that axial loading is the governing design factor for these members.

Finally, the ULS verification results for the horizontal members of the GFRP tower are presented in Table 5.8.

**Table 5. 8:** Structural verification of horizontals – X-bracing GFRP tower

	Units	Section 1	Section 2	Section 3	Section 4	Section 5	Section 6
<b>Axial Tension Verification</b>							
Design tensile resistance, $N_{t,Rd}$	kN	778.4	778.4	778.4	778.4	1091.7	1236.6
Design action, $N_{t,Ed}$	kN	4.8	9.3	17.8	20.1	22.9	26.5
Verification $N_{t,Ed} < N_{t,Rd}$	-	Ok	Ok	Ok	Ok	Ok	Ok
<b>Axial Compression Verification</b>							
Governing compressive resistance, $N_{c,Rd}$	kN	106.1	110.4	88.1	125.5	125.7	118.7
Design action, $N_{c,Ed}$	kN	9.2	22.8	29.7	36.0	43.0	54.2
Verification $N_{c,Ed} < N_{c,Rd}$	-	Ok	Ok	Ok	Ok	Ok	Ok

<b>Bending Verification</b>							
Bending moment resistance, $MR_d$	kNm	10.6	10.6	10.6	10.6	18.0	20.0
Design action, $ME_d$	kNm	0.02	0.03	0.03	0.4	0.1	0.0
Verification $ME_d < MR_d$	-	Ok	Ok	Ok	Ok	Ok	Ok
<b>Shear Verification</b>							
Shear resistance, $VR_d$	kN	2206.6	2206.6	2206.6	2206.6	3091.9	3518.4
Design action, $VE_d$	kN	0.01	0.03	0.04	0.03	0.04	0.03
Verification $VE_d < VR_d$	-	Ok	Ok	Ok	Ok	Ok	Ok

All horizontal members satisfied the ULS requirements for axial tension, axial compression, bending, and shear across all sections. The highest demand-to-capacity ratios occurred in compression, particularly in Sections 5 and 6, where the applied loads were closer to the available capacity, yet still met the verification criteria. In all cases, the calculated design actions were lower than the corresponding design resistances, confirming that the entire GFRP tower satisfies the ULS verification requirements with adequate safety margins.

## 6. RESULTS AND DISCUSSION

### 6.1. First Design Loop Overview

In the first design loop, the steel reference tower was compared with a GFRP pultruded profile tower using the same loads calculated according to Eurocode EN 1991-1-4 and EN 1993-3-1. The cross-sectional dimensions were kept identical. Under serviceability checks, the GFRP tower exceeded the tilt limit of  $0.66^\circ$ , reaching  $1.31^\circ$  with a tip displacement of 1582 mm, whereas the steel tower had  $0.55^\circ$  and 252.4 mm, respectively.

Under ULS verification for axial stresses, the maximum stress in the GFRP tower was 281.70 MPa, below the design resistance of 291.73 MPa, confirming that the main issue was stiffness rather than strength. To improve stiffness, seven design iterations were analysed, with loads recalculated for each case. Among them, Iteration 3 (X-bracing) and Iteration 7 (full CFRP) gave the most favourable results. Iteration 3 replaced Z-bracing with X-bracing, increasing the number of diagonals; this produced a weight of 3.0 t, tilt angle of  $0.62^\circ$ , and displacement of 293.1 mm. Iteration 7 replaced all elements with CFRP pultruded profiles, achieving a 44 % mass reduction (2.12 t) compared to steel, a tilt angle of  $0.50^\circ$ , and a displacement of 227.3 mm – the optimal performance among all designs.

The most relevant numerical values for interpretation are presented in Table 6.1, highlighting that achieving serviceability compliance using GFRP alone is challenging without incurring a significant weight penalty. Reconfiguring the bracing improves stiffness, but the most effective approach was the strategic use of CFRP, either in hybrid or full configurations, to meet displacement limits while reducing mass.

**Table 6. 1:** Key results from the first design loop used for interpretation

Tower	Displacement (mm)	Tilt angle	Maximum tilt angle	Verification $\theta < \theta_{max}$	Weight (t)	S11 (MPa)
Steel	252.4	0.55	0.66	OK	3.77	-
GFRP	1582	1.31	0.66	Exceeds limit	0.864	203.7
I3 (X-bracing)	293.1	0.62	0.66	Ok	3.00	41.02
I7(CFRP)	227.3	0.5	0.66	Ok	2.12	79.54

Figure 6.1 compares the mass and tip displacement of the different first-loop tower configurations as a function of the main leg diameter. The plot uses the left axis for mass and the right axis for displacement, with dashed lines showing the maximum allowable displacement (350 mm) and the reference steel tower

mass. The steel tower (black) has a mass above 3.7 t with a displacement slightly over 250 mm. The hybrid GFRP–CFRP design (green) is significantly lighter and remains well below the displacement limit. Iteration 3 (blue, X-bracing) reduces displacement to approximately 293 mm but increases the mass to nearly 3 t. Iteration 7 (red, CFRP) achieves both a low mass (2.12 t) and a low displacement ( $\sim 227$  mm), outperforming all other configurations. Hybrid designs show intermediate performance, providing improved stiffness compared to full GFRP but with a slightly higher mass than full CFRP. Overall, these results confirm CFRP, whether in full or hybrid form, as the most balanced solution in terms of stiffness-to-weight performance during the first design loop.

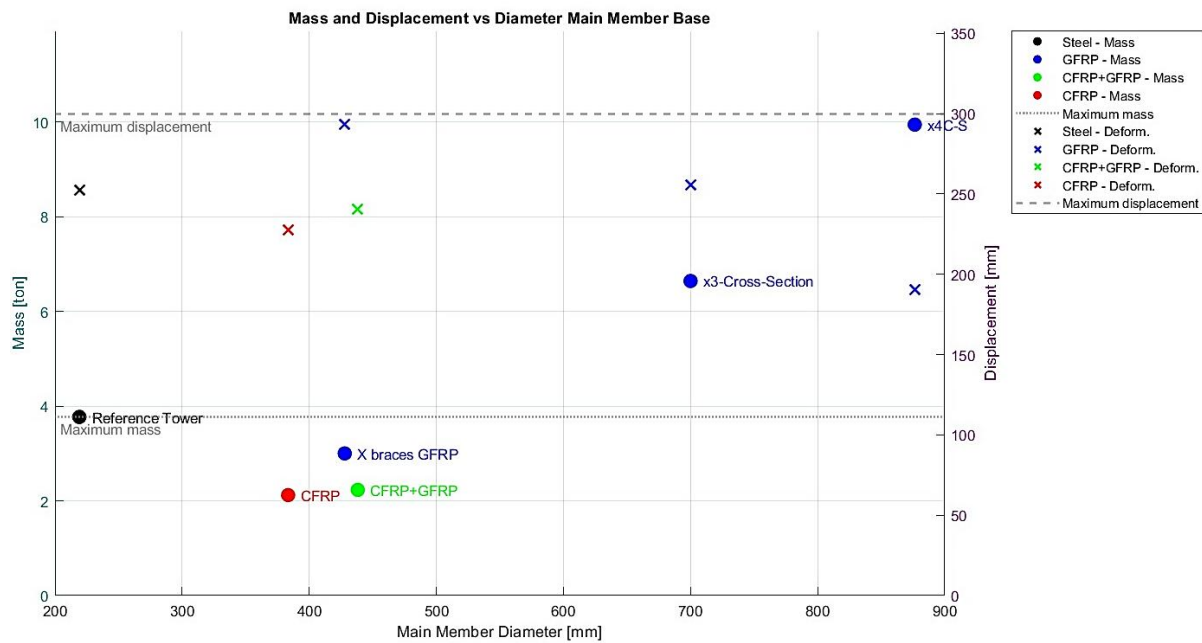
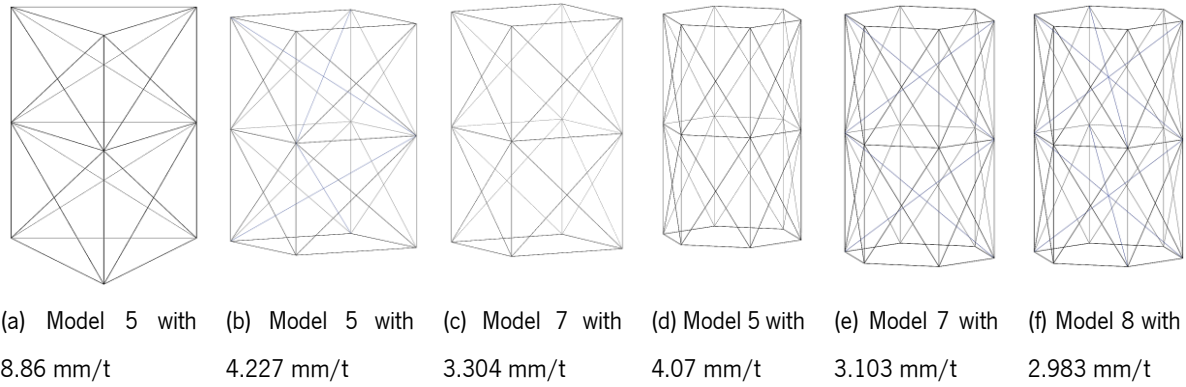


Figure 6. 1: Mass and tip displacement vs main member base diameter

## 6.2. Second Design Loop Overview

The second design loop explored different tower geometries, focusing on triangular, square, and hexagonal base layouts. Initial screening was performed using small-scale prototypes with identical loads, boundary conditions, profiles, and base dimensions (inscribed in a circle). From 20 initial models, six were selected based on their specific displacement (mm/t), as shown in Figure 6.2. These models had a base width of 2 m (inscribed in a circle) and horizontal divisions every 1500 mm.



**Figure 6. 2:** Prototype models selected based on specific displacement performance.

From these prototypes, both tapered and non-tapered versions were scaled to full 36 m height. Table 6.2 presents the key results for non-tapered configurations. All exhibited large tip displacements well above SLS limits, making them unsuitable. The triangular model showed the poorest performance, with a specific displacement of 1668.4 mm/t, and was therefore excluded from further tapered analysis.

**Table 6. 2:** Key results from the second design loop – non-tapered towers

<b>N</b>	<b>Type</b>	<b>Displacement u2 (mm)</b>	<b>Tilt angle</b>	<b>Stress S11(MPa)</b>	<b>Weight (t)</b>	<b>Specific displacement (mm/t)</b>
1	Triangular	3978	1.47	403.3	2.38427	1668.44
2	Hexagonal	3010	1.43	238.5	3.47572	866.01
3	Hexagonal internal diagonals	2996	1.43	242.5	3.98059	752.65
4	Square	1977	1.36	189.2	3.17903	621.89
5	Square internal diagonals	1970	1.36	190.9	3.61006	545.70

For the tapered models, two square and two hexagonal configurations were considered. The square towers used bases of 4 m tapering to 2 m up to 24 m height (constant above), and 3 m tapering to 1.2 m, the latter also tested with internal diagonals. The hexagonal towers tapered from 3 m to 1.2 m up to 24 m, remaining constant to the top, tested both with and without diagonals. Loads were recalculated for each case, and cross-sections were varied from larger at the base to smaller at the tip.

Table 6.3 presents the results. Diagonals had negligible influence on stiffness but increased tower weight, while wider bases provided better stiffness. Hexagonal towers consistently showed higher tip displacements than square equivalents due to greater projected wind area. Although all tapered designs were lighter than the steel tower (3.77 t), none met the SLS tilt or displacement limits.

**Table 6. 3:** Key results from the second design loop – tapered towers.

<b>N</b>	<b>Type</b>	<b>Deformation u<sub>2</sub>(mm)</b>	<b>Tilt angle</b>	<b>Stress S<sub>11</sub>(MPa)</b>	<b>Weight (t)</b>	<b>Specific deformation (mm/t)</b>
1	Hexagon model 3m-1.2m	1898	1.36	111.3	2.799	678.01
2	Hexagon model 3m-1.2m with internal diagonals	1889	1.35	112.3	3.275	576.65
3	Square 3 m -1.2 m base	845.8	1.12	57.52	2.585	327.08
4	Square 3 m -1.2 m base with internal diagonals	843.1	1.11	57.93	3.315	254.31
5	Square 4 m -2 m base	655.8	1.01	69.39	2.941	222.91

Despite geometric improvements, none of the tapered GFRP configurations satisfied SLS displacement or tilt angle requirements under the applied load cases. This reinforces a fundamental limitation in relying solely on geometry modifications when using GFRP for tall self-supporting towers. The results suggest that moderate geometric optimisation combined with material substitution – as highlighted in the first design loop – is a more effective strategy than pursuing increasingly complex bracing patterns.

### 6.3. Discussion

FRP offers outstanding mechanical properties for diverse structural applications. Literature shows that CFRP trusses manufactured through filament winding have already been applied in the telecommunication sector, reducing tower weight, improving sustainability, eliminating corrosion concerns, and even lowering lifecycle costs. However, filament winding requires high initial investment, and carbon fibres remain more expensive than glass fibres.

This study focused on the applicability of GFRP pultruded profiles for telecommunication towers because these profiles are cost-competitive with steel, widely available, and offer corrosion resistance. Their repeatable manufacturing process makes them attractive for large-scale deployment, but two challenges emerged: insufficient stiffness compared to steel and the difficulty of creating reliable joints. Unlike filament-wound structures where joints are minimised, pultruded towers require numerous connections. Bolted joints can cause fibre tearing, while bonded joints face durability concerns, highlighting the need for improved joint technologies. In this study, a pre-tightened bolted connection was suggested because

it reduces the risk of fibre crushing by distributing the clamping force more evenly, improves slip resistance under cyclic loading, and allows for disassembly during maintenance – offering a more practical balance between strength, durability, and inspectability compared to conventional bolted or bonded joints.

The results of this investigation confirm that FRP can replace steel in telecommunication towers, although further research is needed. The CFRP tapered tower achieved a 44% mass reduction while meeting both ULS and SLS requirements. GFRP with X-bracing achieved a 20% weight reduction but still struggled with stiffness, requiring additional bracing. However, increasing bracing density, significantly increases joint complexity and cost, raising concerns over economic feasibility for pultruded designs.

To advance FRP tower design, three strategies appear most promising:

1. **Material optimisation:** selectively substituting GFRP with CFRP to exploit its higher stiffness and strength while maintaining low weight.
2. **Load reduction:** employing lighter antenna equipment or aerodynamic shielding to reduce wind-induced forces.
3. **Re-evaluation of allowable deformation limits:** in specific applications, relaxing SLS criteria where safety and operational performance are not compromised. Emerging technologies may enable such adjustments without affecting reliability.

### *6.3.1. Consistency with Literature Findings*

The results of this study are consistent with previous research demonstrating that GFRP towers and truss structures are more flexible than their steel counterparts. This increased flexibility is primarily due to the relatively lower elastic modulus of GFRP, which, although beneficial for weight reduction, results in significantly greater deformations under service loading.

Gao et al. [19] conducted a study on a GFRP lattice tower designed and analysed using large deflection theory. The results confirmed that such structures exhibit pronounced large-deflection behaviour, with vibration and displacement responses notably higher than those of equivalent steel towers.

Field and experimental investigations further reinforce this trend. For instance, a 25 m telecommunication tower constructed with pultruded GFRP pipes as main members and steel braces/struts recorded a maximum displacement of 1103.24 mm, equivalent to 4.41 % of its height. Under typhoon conditions with a wind speed of 17.26 m/s, the same tower experienced a tip displacement of 10 m (40 % of its height) without suffering structural damage (see Figure 6.3). These findings demonstrate that, while GFRP towers can resist stresses effectively, the major challenge lies in their larger deformations [19].



**Figure 6. 3:** Observed tip displacement of a GFRP tower, reproduced from [19].

Similarly, Latif [64] examined a 30 m pultruded GFRP tower and reported considerably higher deflections than in a steel reference tower. These displacements were directly linked to the lower elastic modulus of the composite material. Despite these large deflections, stresses remained below allowable limits, making the Serviceability Limit State (SLS) the governing design criterion. This outcome again confirms that, for pultruded GFRP lattice systems, SLS is often the controlling limit state [60].

Overall, the large displacements observed in the present study are in full agreement with published findings, reinforcing the conclusion that geometric optimisation alone cannot ensure SLS compliance for tall GFRP towers. Strategies involving material substitution, load reduction, or adjustments to serviceability criteria remain necessary to achieve viable designs.

## 7. CONCLUSION AND FUTURE WORK

### 7.1. Conclusions

This study set out to design and analyse a 36 m self-supporting telecommunication tower using FRP materials—specifically GFRP and CFRP—meeting a 50-year service life, a maximum allowable head offset of  $0.66^\circ$ , and modular truss segments of 6 m or 12 m. Applying the Geometry–Architecture–Process (GAP) methodology, the optimal configurations, materials, and manufacturing approaches were defined, with pultruded profiles selected for their availability and cost-effectiveness. Design actions were determined according to Eurocode standards, and structural behaviour was simulated via FEA and compared with a steel reference tower.

When comparing the steel reference tower with the GFRP pultruded profile tower, the results showed a substantial weight reduction, but a 6.26-times increase in displacement, exceeding both the allowable tilt angle and the SLS requirements. However, ULS verification of axial stresses confirmed that the GFRP tower remained within the strength limits.

The analysis showed that GFRP towers, while achieving mass reductions of up to 20 %, struggled to meet Serviceability Limit State (SLS) requirements without significant geometric optimisation. CFRP substitution markedly improved stiffness, enabling compliance with both SLS and ULS, with a full CFRP design achieving a 44 % weight reduction compared to steel. SLS verifications, such as tip displacement and tilt angle, were identified as the governing design criteria for GFRP configurations, while ULS checks confirmed all designs met strength requirements.

Several truss arrangements and configurations were investigated, including X- and Z-bracing and tapered geometries. Increased bracing density improved stiffness but introduced complexity in joint design and fabrication, making overly complex GFRP geometries less viable for large-scale deployment. The influence of internal diagonals was negligible, while tapered towers exhibited better stiffness, and base width was found to significantly affect the mechanical performance of the tower.

The findings confirm the feasibility of FRP towers as a sustainable alternative to steel, provided that either high-modulus materials (e.g., CFRP) or targeted geometric optimisation is implemented. In conclusion, FRP towers present a promising solution to replace traditional steel designs by enabling material optimisation, reducing the projected antenna area, or allowing slightly greater deformations where acceptable. Nevertheless, further studies are needed to fully evaluate and refine this emerging solution.

## 7.2. Future Work

Future work on FRP telecommunication towers should focus on both material innovation and design refinement. Hybrid GFRP–CFRP layouts appear particularly promising, as they can deliver the stiffness benefits of carbon fibre while keeping costs closer to those of glass fibre. In parallel, reducing applied loads—through lighter antenna equipment or aerodynamic shielding—could ease serviceability demands and extend design flexibility. In certain applications, relaxing current displacement limits may also be viable, provided that safety and operational requirements are maintained.

Advances in connection technology will be critical for making pultruded FRP towers more competitive. Optimised joint systems that are simple to fabricate, durable in aggressive environments, and cost-effective at scale would address one of the key barriers to implementation. Complementary to this, experimental validation—through scaled or full-scale testing—should be pursued to confirm numerical predictions, alongside long-term fatigue and durability assessments to understand in-service behaviour. From a practical perspective, manufacturing feasibility needs to be integrated into the design stage, ensuring that proposed solutions can be produced reliably and economically. Life-cycle assessments will also be important to quantify environmental and economic performance over the full-service life. Finally, targeted use of CFRP in key members, or strategic mixed-material configurations, could further enhance stiffness-to-weight efficiency while containing costs.

Additional research into dynamic response under wind-induced vibrations and fire performance for telecom safety compliance, would help move these solutions from experimental studies to real-world projects, supporting wider use of composite towers in telecommunications

## 8. REFERENCES

- [1] A. Azhar Abdulkareem Majeed, "Telecommunication Cell Tower Most Common Alternatives Overview," *American Journal of Civil Engineering*, vol. 5, no. 5, p. 268, 2017, doi: 10.11648/j.ajce.20170505.12.
- [2] Y. Elhakim, N. Hazem, T. Ismail, M. Mahmoud, and I. Fahim, "Towards greener telecommunication towers: A framework for 'LEED for telecom towers,'" *Cogent Eng*, vol. 10, no. 1, 2023, doi: 10.1080/23311916.2023.2185953.
- [3] M. L. Moss, S. M. Kaufman, and A. M. Townsend, "The relationship of sustainability to telecommunications," *Technol Soc*, vol. 28, no. 1–2, pp. 235–244, Jan. 2006, doi: 10.1016/j.techsoc.2005.10.011.
- [4] B. Kiriparan, J. Janusan, J. A. S. C. Jayasinghe, and U. I. Dissanayake, "Comparative Study on Different Structural Forms of Telecommunication Towers," *SSESL*, vol. 33, no. 02, 2023, Accessed: Apr. 04, 2025. [Online]. Available: <http://repo.lib.jfn.ac.lk/ujrr/handle/123456789/9991>
- [5] I. Vayas, J. Jaspert, A. Bureau, M. Tibolt, S. Reygner, and M. Papavasiliou, "Telecommunication and transmission lattice towers from angle sections – the ANGELHY project," *ce/papers*, vol. 4, no. 2–4, pp. 210–217, Sep. 2021, doi: 10.1002/cepa.1283.
- [6] R. T. Loto and C. A. Loto, "Corrosion and Protection of Facilities and Infrastructures in Telecommunications Industry - A Review," *IOP Conf Ser Mater Sci Eng*, vol. 1107, no. 1, p. 012014, Apr. 2021, doi: 10.1088/1757-899x/1107/1/012014.
- [7] D. V. Billionis, K. Vlachakis, D. Vamvatsikos, M. E. Dasiou, I. Vayas, and K. Lagouvardos, "Risk assessment of rehabilitation strategies for steel lattice telecommunication towers of Greece under extreme wind hazard," *Eng Struct*, vol. 267, Sep. 2022, doi: 10.1016/j.engstruct.2022.114625.
- [8] M. Abiad, S. Kadry, and S. Ionescu, "Preventive Predictive Maintenance of Telecommunication Equipment - A Review," in *Proceedings of the 4th International Conference on Applied and Theoretical Computing and Communication Technology, iCATccT 2018*, Institute of Electrical and Electronics Engineers Inc., Sep. 2018, pp. 154–159. doi: 10.1109/iCATccT44854.2018.9001972.

- 
- [9] V. Křivý, Z. Vašek, M. Vacek, and L. Mynarzová, “Corrosion Damage to Joints of Lattice Towers Designed from Weathering Steels,” *Materials*, vol. 15, no. 9, May 2022, doi: 10.3390/ma15093397.
- [10] Y. Elhakim, T. Ismail, and I. Fahim, “Optimum Selection of Communication Tower Structures Based on Wind Loads & lifecycle cost analysis,” *Cogent Eng*, vol. 9, no. 1, 2022, doi: 10.1080/23311916.2022.2132656.
- [11] S. Alshurafa and D. Polyzois, “Design recommendations and comparative study of FRP and steel guyed towers,” *Engineering Science and Technology, an International Journal*, vol. 21, no. 5, pp. 807–814, Oct. 2018, doi: 10.1016/j.jestch.2018.06.014.
- [12] N. Nguyen *et al.*, “Quantum computing for corrosion-resistant materials and anti-corrosive coatings design,” New-York, Apr. 2025. doi: <https://doi.org/10.48550/arXiv.2406.18759>.
- [13] A. R. M. Forkan *et al.*, “CorrDetector: A framework for structural corrosion detection from drone images using ensemble deep learning,” *Expert Syst Appl*, vol. 193, May 2022, doi: 10.1016/j.eswa.2021.116461.
- [14] T. Keller and T. Vallée, “Adhesively bonded lap joints from pultruded GFRP profiles. Part I: Stress-strain analysis and failure modes,” *Compos B Eng*, vol. 36, no. 4, pp. 331–340, Jun. 2005, doi: 10.1016/j.compositesb.2004.11.001.
- [15] S. Alshurafa, H. Alhayek, and D. Polyzois, “Development of GFRP Monopole Guyed Communication Tower,” *Journal of Composites for Construction*, vol. 27, no. 1, Feb. 2023, doi: 10.1061/jccof2.cceng-3799.
- [16] M. A. Ehlen, “Life-Cycle Costs of Fiber-Reinforced-Polymer Bridge Decks,” *Journal of Materials in Civil Engineering*, vol. 11, no. 3, pp. 224–230, Aug. 1999, doi: 10.1061/(ASCE)0899-1561(1999)11:3(224).
- [17] S. Alshurafa, H. Alhayek, and D. Polyzois, “Finite element method for the static and dynamic analysis of FRP guyed tower,” *J Comput Des Eng*, vol. 6, no. 3, pp. 436–446, Jul. 2019, doi: 10.1016/j.jcde.2018.08.004.
- [18] I. Ramirez-Vazquez, R. Hernández-Corona, and J. E. Salgado-Talavera, “Composite Materials As an Alternative to Replace Steel Members on Lattice Power Transmission Towers,” 2015, doi: 10.1061/(ASCE)MT.1943.
- [19] H. Gao, Y. Sun, X. Lei, Y. Gao, and H. Liu, “Mechanical properties and application of glass fiber reinforced polyurethane composites communication lattice tower,” *Constr Build Mater*, vol. 411, p. 134180, Jan. 2024, doi: 10.1016/j.conbuildmat.2023.134180.

- 
- [20] Y. Chen, M. Duan, X. Zou, Y. Feng, and G. Li, "Experimental and Numerical Investigation of Joints for a Pultruded Fiber-Reinforced Polymer Truss," *Polymers (Basel)*, vol. 14, no. 22, Nov. 2022, doi: 10.3390/polym14224810.
- [21] B. A. Andrew Ochonski and B. Andrew Ochonski, "Development of Latticed Towers Using Advanced Composite Materials," The University of Manitoba, 2009.
- [22] P. Liu, Q. Zhao, F. Li, J. Liu, and H. Chen, "Research on the mechanical properties of a glass fiber reinforced polymer-steel combined truss structure," *Scientific World Journal*, vol. 2014, 2014, doi: 10.1155/2014/309872.
- [23] R. M. Hizam, A. C. Manalo, and W. Karunasena, "A review of FRP composite truss systems and its connection.," in *In Proceedings of the 22nd Australasian Conference on the Mechanics of Structures and Materials (ACMSM22)*., University of Southern Queensland, Jan. 2013.
- [24] C. Hunt, "WrapToR composite truss structures," University-of-Bristol, Bristol, 2021.
- [25] C. J. Hunt, M. R. Wisnom, and B. K. S. Woods, "WrapToR composite truss structures: Improved process and structural efficiency," 2019, doi: 10.5523/bris.gtlkwtjxtba2vbzo432xstso.
- [26] E. J. Barbero, *Introduction to Composite Materials Design*, 3rd ed. CRC Press, 2017. doi: 10.1201/9781439894132.
- [27] M. Balasubramanian, *Composite materials and Processing*. CRC Press, 2014. doi: 10.1201/B15551.
- [28] H. V. S. GangaRao and W. Prachasaree, *FRP Composite Structures*. Boca Raton: CRC Press, 2021. doi: 10.1201/9781003196754.
- [29] Y. Lin, J. Min, H. Teng, J. Lin, J. Hu, and N. Xu, "Flexural Performance of Steel-FRP Composites for Automotive Applications," *Automotive Innovation*, vol. 3, no. 3, pp. 280–295, Sep. 2020, doi: 10.1007/S42154-020-00109-X/FIGURES/23.
- [30] V. V. Vasiliev, V. A. Barynin, and A. F. Razin, "Anisogrid composite lattice structures - Development and aerospace applications," *Compos Struct*, vol. 94, no. 3, pp. 1117–1127, Feb. 2012, doi: 10.1016/j.compstruct.2011.10.023.
- [31] M. Arowolo, W. Azoti, and B. Castanié, "Comparative study of the thermomechanical properties of natural fiber reinforced thermoplastic composites: A structural application for quadcopter design," *Mechanics of Advanced Materials and Structures*, vol. 32, no. 7, pp. 1425–1446, 2025, doi: 10.1080/15376494.2024.2364067.

- [32] B. CASTANIE, C. BOUVET, and M. Ginot, "Review of composite sandwich structure in aeronautic applications," *Composites Part C: Open Access*, vol. 1, p. 100004, Aug. 2020, doi: 10.1016/J.JCOMC.2020.100004.
- [33] B. Castanié *et al.*, "Review of monolithic composite laminate and stiffened structures in aeronautic applications," *Composites Part C: Open Access*, vol. 17, p. 100585, Jul. 2025, doi: 10.1016/J.JCOMC.2025.100585.
- [34] H. V. S. GangaRao and W. Prachasaree, *FRP Composite Structures*, 1st ed. Boca Raton: CRC Press, 2021. doi: 10.1201/9781003196754.
- [35] Manoochehr. Zoghi, "The international handbook of FRP composites in civil engineering," p. 682, 2014, Accessed: Aug. 01, 2025. [Online]. Available: [https://books.google.com/books/about/The\\_International\\_Handbook\\_of\\_FRP\\_Compos.html?id=NUbGAAAAQBAJ](https://books.google.com/books/about/The_International_Handbook_of_FRP_Compos.html?id=NUbGAAAAQBAJ)
- [36] A. Ulu, A. I. Tutar, A. Kurklu, and F. Cakir, "Effect of excessive fiber reinforcement on mechanical properties of chopped glass fiber reinforced polymer concretes," *Constr Build Mater*, vol. 359, p. 129486, Dec. 2022, doi: 10.1016/J.CONBUILDMAT.2022.129486.
- [37] D. Veit, "Carbon Fibers," *Fibers*, pp. 779–799, 2022, doi: 10.1007/978-3-031-15309-9\_38.
- [38] B. Castanié *et al.*, "Wood and plywood as eco-materials for sustainable mobility: A review," *Compos Struct*, vol. 329, p. 117790, Feb. 2024, doi: 10.1016/J.COMPSTRUCT.2023.117790.
- [39] S. Kangishwar, N. Radhika, A. A. Sheik, A. Chavali, and S. Hariharan, "A comprehensive review on polymer matrix composites: material selection, fabrication, and application," *Polymer Bulletin 2022 80:1*, vol. 80, no. 1, pp. 47–87, Jan. 2022, doi: 10.1007/S00289-022-04087-4.
- [40] S. Yan and Y. Abdin, "Fatigue behavior of Elium®-based thermoplastic composites fabricated by liquid composite molding : A review," *Compos B Eng*, vol. 295, p. 112159, Apr. 2025, doi: 10.1016/J.COMPOSITESB.2025.112159.
- [41] M. Rady *et al.*, "A Historical Twist on Long-Range Wireless: Building a 103 km Multi-Hop Network Replicating Claude Chappe's Telegraph," *Sensors (Basel)*, vol. 22, no. 19, p. 7586, Oct. 2022, doi: 10.3390/S22197586.
- [42] B.W. Smith, "50 years in the design of towers and masts. From IASS recommendations to current procedures," *riunet.upv.esB SMITHSymposium of the International Association for Shell and Spatial, 2009* • *riunet.upv.es*, 2009, Accessed: Aug. 03, 2025. [Online]. Available: <https://riunet.upv.es/handle/10251/6471>

- [43] B. W. . Smith, "Communication structures," 1st ed. 1 Vol. Thomas Telford Ltd, London, 2007, p. 338
- [44] A. Falade, "The telecoms sector on the Rise: The opportunities and the uncertainties," Vanguard. Accessed: Aug. 15, 2025. [Online]. Available: <https://www.vanguardngr.com/2024/06/the-telecoms-sector-on-the-rise-the-opportunities-and-the-uncertainties/>
- [45] E. Korzeniewska, A. K.-2019 I. International, and undefined 2019, "5G technology as the succesive stage in the history of wireless telecommunication," *ieeexplore.ieee.orgE Korzeniewska, A Krawczyk2019 IEEE International Conference on Modern Electrical and Energy, 2019 • ieeexplore.ieee.org*, Accessed: Aug. 03, 2025. [Online]. Available: <https://ieeexplore.ieee.org/abstract/document/8896516/>
- [46] S. C. Kasera, "Structural analysis of telecommunications towers: Report content and its importance to the industry and public," *World Journal of Advanced Engineering Technology and Sciences*, vol. 15, no. 1, pp. 153–162, Apr. 2025, doi: 10.30574/WJAETS.2025.15.1.0196.
- [47] J. Zhang, Y. Wang, Q. Xu, and H. Gao, "Life cycle cost of communication towers: identification and hierarchical classification of influencing factors," *Scientific Reports 2025 15:1*, vol. 15, no. 1, pp. 1–30, Jul. 2025, doi: 10.1038/s41598-025-06334-w.
- [48] J. Asassfeh, F. Samson, M. A.-I. J. of, and undefined 2017, "Reviewing and classifying the effective factors in selection telecommunication antenna towers sites," *go.gale.comJA Asassfeh, F Samson, M AITarawnehInternational Journal of Digital Information and Wireless Communications, 2017 • go.gale.com*, Mar. 2018, Accessed: Aug. 03, 2025. [Online]. Available: <https://go.gale.com/ps/i.do?id=GALE%7CA536388881&sid=googleScholar&v=2.1&it=r&linkaccess=abs&issn=2225658X&p=AONE&sw=w>
- [49] D. Xu, K. Yang, and W. Duan, "Visual Analysis of Carbon Emissions in Steel Industry Based on CiteSpace," Sep. 2021, doi: 10.21203/RS.3.RS-770036/V1.
- [50] L. Huaccho Huatuco and P. D. Ball, "The quest for achieving United Nations sustainability development goals (SDGs) Infrastructure and innovation for responsible production and consumption," *RAUSP Management Journal*, vol. 54, no. 3, pp. 357–362, Nov. 2019, doi: 10.1108/RAUSP-04-2019-0068.
- [51] E. Bontempi *et al.*, "Sustainable Materials and their Contribution to the Sustainable Development Goals (SDGs): A Critical Review Based on an Italian Example," *Molecules 2021, Vol. 26, Page 1407*, vol. 26, no. 5, p. 1407, Mar. 2021, doi: 10.3390/MOLECULES26051407.

- [52] C. J. Hunt, F. Morabito, C. Grace, Y. Zhao, and B. K. S. Woods, "A review of composite lattice structures," Mar. 15, 2022, *Elsevier Ltd.* doi: 10.1016/j.compstruct.2021.115120.
- [53] D. Wang and M. M. Abdalla, "Global and local buckling analysis of grid-stiffened composite panels," *Compos Struct*, vol. 119, pp. 767–776, Jan. 2015, doi: 10.1016/J.COMPSTRUCT.2014.09.050.
- [54] S. Shroff, E. Acar, and C. Kassapoglou, "Design, analysis, fabrication, and testing of composite grid-stiffened panels for aircraft structures," *Thin-Walled Structures*, vol. 119, pp. 235–246, Oct. 2017, doi: 10.1016/J.TWS.2017.06.006.
- [55] G. D. Xu, J. J. Zhai, T. Zeng, Z. H. Wang, S. Cheng, and D. N. Fang, "Response of composite sandwich beams with graded lattice core," *Compos Struct*, vol. 119, pp. 666–676, Jan. 2015, doi: 10.1016/J.COMPSTRUCT.2014.09.042.
- [56] S. Yin, L. Wu, L. Ma, and S. Nutt, "Pyramidal lattice sandwich structures with hollow composite trusses," *Compos Struct*, vol. 93, no. 12, pp. 3104–3111, Nov. 2011, doi: 10.1016/J.COMPSTRUCT.2011.06.025.
- [57] J. Xiong, L. Ma, A. Vaziri, J. Yang, and L. Wu, "Mechanical behavior of carbon fiber composite lattice core sandwich panels fabricated by laser cutting," *Acta Mater*, vol. 60, no. 13–14, pp. 5322–5334, Aug. 2012, doi: 10.1016/J.ACTAMAT.2012.06.004.
- [58] M. Clayton, "Design Characteristics of the IsoTruss® Geometry," 2022. Accessed: Aug. 15, 2025. [Online]. Available: <https://isotruss.com/wp-content/uploads/2022/12/Design-Characteristics-of-IsoTruss.pdf>
- [59] Aswani Asok and Mervin Ealiyas Mathews, "Study on Stability of Isotrussed Grid Wind Turbine Tower," *International Journal of Engineering Research and*, vol. V5, no. 08, Aug. 2016, doi: 10.17577/IJERTV5IS080439.
- [60] M. S. Pfeil, A. M. A. J. Teixeira, and R. C. Battista, "Experimental tests on GFRP truss modules for dismountable bridges," *Compos Struct*, vol. 89, no. 1, pp. 70–76, Jun. 2009, doi: 10.1016/j.compstruct.2008.06.019.
- [61] B. K. S. Woods, I. Hill, and M. I. Friswell, "Ultra-efficient wound composite truss structures," *Compos Part A Appl Sci Manuf*, vol. 90, pp. 111–124, Nov. 2016, doi: 10.1016/j.compositesa.2016.06.022.
- [62] D. Bačinskas *et al.*, "Structural Analysis of GFRP Truss Bridge Model," *Procedia Eng*, vol. 172, pp. 68–74, Jan. 2017, doi: 10.1016/J.PROENG.2017.02.018.

- [63] C. Bhowmik, K. Gupta, and P. Chakraborti, "Stability analysis of glass fibre polyamide composite transmission tower," *Journal of Reinforced Plastics and Composites*, vol. 39, no. 23–24, pp. 918–931, Dec. 2020, doi: 10.1177/0731684420937357.
- [64] I. S. Latif, "FRP TELECOME TOWER," Master dissertation, Dept. Civil Eng., Nirma University, 2009.
- [65] A. Godat, F. Légeron, V. Gagné, and B. Marmion, "Use of FRP pultruded members for electricity transmission towers," *Compos Struct*, vol. 105, pp. 408–421, Nov. 2013, doi: 10.1016/J.COMPSTRUCT.2013.05.025.
- [66] A. Syamsir *et al.*, "Performance Analysis of Full Assembly Glass Fiber-Reinforced Polymer Composite Cross-Arm in Transmission Tower," *Polymers 2022, Vol. 14, Page 1563*, vol. 14, no. 8, p. 1563, Apr. 2022, doi: 10.3390/POLYM14081563.
- [67] J. P. Pereira, E. M. Carvalho, W. D. Varela, and J. D. Vieira, "Dynamic analysis of a composite material telecommunications tower under wind loads," *In XLII Ibero-Latin American Congress on Computational Methods in Engineering*, vol. 3, no. 3, Nov. 2021.
- [68] N. Prasad Rao, R. P. Rokade, and R. Balagopal, "Failure investigation of GFRP communication towers," *Eng Fail Anal*, vol. 79, pp. 397–407, Sep. 2017, doi: 10.1016/j.engfailanal.2017.05.002.
- [69] M. R. M. Asyraf *et al.*, "Effect of Fibre Layering Sequences on Flexural Creep Properties of Kenaf Fibre-reinforced Unsaturated Polyester Composite for Structural Applications," *Fibers and Polymers*, vol. 23, no. 11, pp. 3232–3240, Nov. 2022, doi: 10.1007/S12221-022-4386-7/METRICS.
- [70] J. M. G. Rabelo, J. S. Becho, M. Greco, and C. A. Cimini, "Modeling the creep behavior of GRFP truss structures with Positional Finite Element Method," *Latin American Journal of Solids and Structures*, vol. 15, no. 2, p. e17, Apr. 2018, doi: 10.1590/1679-78254432.
- [71] M. F. Sá, A. M. Gomes, J. R. Correia, and N. Silvestre, "Creep behavior of pultruded GFRP elements – Part 2: Analytical study," *Compos Struct*, vol. 93, no. 9, pp. 2409–2418, Aug. 2011, doi: 10.1016/J.COMPSTRUCT.2011.04.001.
- [72] N. Aldoumani *et al.*, "Optimisation of the Filament Winding Approach Using a Newly Developed In-House Uncertainty Model," *Eng 2020, Vol. 1, Pages 122-136*, vol. 1, no. 2, pp. 122–136, Oct. 2020, doi: 10.3390/ENG1020008.
- [73] C. J. Hunt, M. R. Wisnom, and B. K. S. Woods, "WrapToR composite truss structures: Improved process and structural efficiency," 2019, doi: 10.5523/bris.gtlkwtjtba2vbzo432xstso.

- [74] Addcomposites, "What is the Pultrusion Manufacturing Process?" Accessed: Aug. 15, 2025. [Online]. Available: <https://www.addcomposites.com/post/pultrusion>
- [75] L. Bank, *Composites for construction: structural design with FRP materials*. 2006. Accessed: Aug. 06, 2025. [Online]. Available: <https://books.google.com/books?hl=en&lr=&id=IB2mTpDtUoAC&oi=fnd&pg=PP1&dq=composit+for+construction+book+lawrence&ots=7nKBvQycLD&sig=Mfjrgn0xOhpbvrc6l3TJRkpoAEc>
- [76] Tadipol, "The composite tower of valencia", REINFORCEDplastics, 2004.
- [77] D. Tobalina-Baldeon, F. Sanz-Adán, M. Martinez-Calvo, C. Gómez, I. Sanz-Pena, and F. Cavas, "Feasibility Analysis of Bolted Joints with Composite Fibre-Reinforced Thermoplastics," *Polymers (Base)*, vol. 13, no. 12, p. 1904, Jun. 2021, doi: 10.3390/POLYM13121904.
- [78] A. A. Zekavati, M. A. Jafari, and A. Saeedi, "Experimental and numerical investigation on the structural performance of a novel type of pultruded composite cross-arm for power transmission towers," *Structures*, vol. 35, pp. 833–844, Jan. 2022, doi: 10.1016/j.istruc.2021.11.047.
- [79] A. H. Valdez *et al.*, "Connection method design for redundant elements of composite materials for transmission towers," in *2016 IEEE PES Transmission & Distribution Conference and Exposition-Latin America (PES T&D-LA)*, IEEE, Sep. 2016, pp. 1–5. doi: 10.1109/TDC-LA.2016.7805627.
- [80] A. Parashar and P. Mertiny, "Adhesively bonded composite tubular joints: Review," *Int J Adhes Adhes*, vol. 38, pp. 58–68, 2012, doi: 10.1016/j.ijadhadh.2012.05.004.
- [81] X. Yang, Y. Bai, F. J. Luo, X. L. Zhao, and F. Ding, "Dynamic and fatigue performances of a large-scale space frame assembled using pultruded GFRP composites," *Compos Struct*, vol. 138, pp. 227–236, Mar. 2016, doi: 10.1016/j.compstruct.2015.11.064.
- [82] S. J. Smith, I. D. Parsons, and K. D. Hjelmstad, "An experimental study of the behavior of connections for pultruded GFRP I-beams and rectangular tubes," *Compos Struct*, vol. 42, no. 3, pp. 281–290, Jul. 1998, doi: 10.1016/S0263-8223(98)00082-8.
- [83] J. Duhovnik and P. Tomšič, "A comparative criteria method for telecommunications towers with different topological designs," *Mechanika*, vol. 18, no. 2, pp. 127–134, 2012, doi: 10.5755/J01.MECH.18.2.1566.
- [84] European Committee for Standardization, *EN 1991-1-4: Eurocode 1: Actions on structures - Part 1-4: General actions - Wind actions*. Brussels, 2005.
- [85] P. Gavrilovic, D. Jurukovski, Z. Rakicevic, and A. Bogdanovic, "Structural design for seismic and wind action of a telecommunication tower-case study", doi: 10.5592/CO/1CroCEE.2021.206.

- [86] European Committee for Standardization, *EN 1991-1-1 Eurocode 1: Actions on structures – Part 1-1: General actions – Densities, self-weight, imposed loads for buildings*. Brussels, 2002. Accessed: Aug. 09, 2025. [Online]. Available: <https://www.icab.fr/doc/icabforce/eurocode/en1991-1-1.htm>
- [87] European Committee for Standardization, *EN 1990: Eurocode - Basis of structural design*. Brussels, 2002.
- [88] G. J. Turvey and Y. Zhang, “Mechanical properties of pultruded GFRP WF, channel and angle profiles for limit state/permmissible stress design,” *Compos B Eng*, vol. 148, pp. 260–271, Sep. 2018, doi: 10.1016/J.COMPOSITESB.2018.04.010.
- [89] European Committee for Standardization, *CEN/TS 19101:2022. Design of fibre-polymer composite structures*. Brussels, 2022. Accessed: Aug. 10, 2025. [Online]. Available: [https://standards.iteh.ai/catalog/standards/cen/bebb5d0f-108f-4472-b688-f904ca7e91ce/cen-ts-19101-2022?srltid=AfmBOoquPzrNdgRWA\\_bN9NxAKXh7zE6wNzQxwnJ5TG80YWmYQF2wt-QN](https://standards.iteh.ai/catalog/standards/cen/bebb5d0f-108f-4472-b688-f904ca7e91ce/cen-ts-19101-2022?srltid=AfmBOoquPzrNdgRWA_bN9NxAKXh7zE6wNzQxwnJ5TG80YWmYQF2wt-QN)
- [90] F. Neveu, B. Castanié, and P. Olivier, “The GAP methodology: A new way to design composite structures,” *Mater Des*, vol. 172, Jun. 2019, doi: 10.1016/j.matdes.2019.107755.
- [91] R. Zhu, F. Li, D. Zhang, and J. Tao, “Effect of Joint Stiffness on Deformation of a Novel Hybrid FRP–Aluminum Space Truss System,” *Journal of Structural Engineering*, vol. 145, no. 11, Nov. 2019, doi: 10.1061/(ASCE)ST.1943-541X.0002426.
- [92] Association Française de Normalisation, “AFNOR, NF EN 1991-1-4/NA:2008 Eurocode 1 – Actions sur les structures – Partie 1-4: Actions générales – Actions du vent – Annexe nationale à la NF EN 1991-1-4:2005.,” Saint-Denis La Plaine, 2008. Accessed: Aug. 10, 2025. [Online]. Available: <https://www.boutique.afnor.org/fr-fr/norme/nf-en-199114-na/eurocode-1-actions-sur-les-structures-partie-14-actions-generales-actions-d/fa155316/30800>
- [93] European Committee for Standardization., *EN 1993-3-1 Eurocode 3 Calcul des structures en acier et Document d’Application Nationale – Tours, mâts et cheminées*, 1st ed., vol. I. 2006.
- [94] L. Sudries, J. Chambe, I. Diboune, J. Serra, W. Azoti, and B. Castanié, “Caractérisation de structures composites thermoplastiques à renforts en fibres de carbone, verre, et biosourcés mises en forme par pultrusion,” Toulouse, 2025. Accessed: Aug. 28, 2025. [Online]. Available: <https://insa-toulouse.hal.science/hal-05170203/>

**ANNEX A**

## LOAD CALCULATION

### 1. Radio equipment (coaxial, antennas, amplifiers, modules)

#### Linear equipment ( distributed along the height of the pylon)

H tower            36            m

#### Coaxial cable

Operator	Unit	-	Op1			Op2			Op2		
Number	-	-	6	4	6	6	4	6	6	4	6
Dimensions	mm	-	7/8"	1/2"	FO+Alim	7/8"	1/2"	FO+Alim	7/8"	1/2"	FO+Alim
Linear mass unit	kg/m	-	0.49	0.22	0.30	0.49	0.22	0.30	0.49	0.22	0.30
Windward surface	m2/m	-	-	-	-	-	-	-	-	-	-
Cable path capacity	m	-	0.4								
Filling coefficient	-	-	1								

#### Total mass and span of linear equipment

Total mass	kg	-	106.575	31.9	65.25	106.575	31.9	65.25	106.575	31.9	65.25
Total sail area	m2/m	-	0.4								

#### Point Equipments (load apply in the head)

##### Panel Antennas

Operator	Unit	-	Op1			Op2			Op2		
Type of antenna	-	-									
Level	m	-									
Number	-	-									
Dimensions	m	-									
Azimut	°	-									
Mass	kg	-	675			675			450		
Weigthed sail	m2	C.S.	9			9			6		

##### FH Antennas

Operator	Unit	-	Op1			Op2			Op2		
Type of antenna	-	-									
Level	m	-									
Number	-	-									
Dimensions	m	-									
Azimut	°	-									
Mass	kg	-									
Weighted sail	m2	C.S.									

#### Amplifiers and modules

Operator	Unit	-	Op1			Op2			Op2		
Type of antenna	-	-									
Level	m	-									
Number	-	-									
Dimensions	m	-									
Azimut	°	-									
Mass	kg	-									
Weighted sail	m2	C.S.									

#### Specific equipment

Operator	Unit	-	Op1			Op2			Op2		
Type of antenna	-	-									
Level	m	-									
Number	-	-									
Dimensions	m	-									
Azimut	°	-									
Mass	kg	-									
Weighted sail	m2	C.S.									

#### Mass and total sail of punctual equipments

Total mass	kg	-	675	0	0	675	0	0	450	0	0
Total weighted sail area	m2	C.S.	9	0	0	9	0	0	6	0	0



## 2.1. Mass of the tower (structure and equipment)

	Units	Section 1	Section 2	Section 3	Section 4	Section 5	Section 6	Base 6
Mass of the structure	kg	524	642	627	755	801	1059	159
Mass of tower equipment	kg	980	967	967	94	103	266	3
Cable tray mass	kg	96	96	96	96	96	96	4
Mass of the antennas	kg	675	675	450				
Total mass	kg	2275	2380	2140	945	1001	1421	166

### Mass of the tower (structure and equipment)

#### Mass of the structure

	Units	Section 1	Section 2	Section 3	Section 4	Section 5	Section 6	Base 6
Main member	kg	266.9	317.3	328.9	398.7	398.7	522.7	26.0
Head flange	kg	11.6	11.6	15.6	19.7	26.3	31.7	39.6
Base flange	kg	11.1	22.1	28.3	31.3	46.8	37.7	88.2
Cross member (tube)	kg	0	0	68.7	104.4	115.7	170.5	0
Cross member (angle)	kg	82.0	111.6	0	0	0	0	0
Diagonal	kg	130.9	153.8	160.4	171.4	183.2	257.5	0.0
Bracing	kg	0	0	0	0	0	0	0
Z-type gusset	kg	5.3	5.3	5.3	5.3	5.3	5.3	
Gusset plate type 'X'	kg	0	0	0	0	0	0	0
Structural bolts	kg	16.7	20.4	19.9	24	25.5	33.7	5.2

#### Mass of pylon equipment

	Units	Section 1	Section 2	Section 3	Section 4	Section 5	Section 6	Base 6
Main ladder	kg	43.6	43.6	43.6	43.6	43.6	43.6	1.8
Cable tray support	kg	25.2	25.2	25.2	25.2	34.7	44.1	
Rail lifeline	kg	19.2	19.2	19.2	19.2	19.2	19.2	0.8
Cable lifeline (jib)	kg							
Cable lifeline (cable)	kg							
Safety cage	kg							
Lightning rod + support	kg	12.4						
Secondary ladder	kg							
Antennas support(s)	kg	396	396	396				
Top working landing	kg							
Working landing	kg	477.4	477.4	477.4				
Resting level(s)	kg	5.9	5.9	5.9	5.9	5.9		
Anti-intrusion	kg						57	
Anti-climbing harrow	kg						102.5	
Bay frames	kg							
Other equipment	kg							
Weight of equipment	kg							

#### Mass of radio equipment

	Units	Section 1	Section 2	Section 3	Section 4	Section 5	Section 6	Base 6
Cable tray	kg	95.9	95.9	95.9	95.9	95.9	95.9	4.0
Antennas	kg	675	675	450				

#### Total mass

Total mass	kg	2275.0	2380.3	2140.2	944.7	1000.7	1421.5	165.7
------------	----	--------	--------	--------	-------	--------	--------	-------

## 2.2. Mass of the frost (structure and equipment)

### Frost in the tower structure

	Units	Section 1	Section 2	Section 3	Section 4	Section 5	Section 6	Base 6
Main member	kg	136.70	136.70	162.55	191.67	191.67	243.37	10.14
Upper flange	kg	0.64	0.64	0.74	0.84	1.12	1.29	1.61
Lower flange	kg	0.64	0.98	1.12	1.40	1.61	1.61	2.42
Crossmember (Tube)	kg	0	0	68.11	79.01	107.60	120.64	0
Crossmember (Angle)	kg	48.86	57.00	0	0	0	0	0
Diagonal	kg	82.21	141.95	151.63	162.07	173.15	184.74	
Bracing	kg							
Z' type gusset	kg							
X' type gusset	kg							

### Frost mass of pylon equipment

	Units	Section 1	Section 2	Section 3	Section 4	Section 5	Section 6	Base 6
Main ladder	kg	36.0	36.0	36.0	36.0	36.0	36.0	0.0
Cable tray support	kg	21.6	21.6	21.6	21.6	28.8	36	
Rail lifeline	kg	14.2	14.2	14.2	14.2	14.2	14.2	0.6
Cable lifeline (jib)	kg							
Cable lifeline (cable)	kg							
Safety cage	kg							
Lightning rod + support	kg	5,6						
Secondary ladder	kg							
Antennas support(s)	kg	199.4	199.4	199.4				
Top working landing	kg							
Working landing	kg	302.4	302.4	302.4				
Resting level(s)	kg	3.5	3.5	3.5	3.5	3.5		
Anti-intrusion	kg						54	
Anti-climbing harrow	kg						45.5	
Bay frames	kg							
Other equipment	kg							
Weight of equipment	kg							

### Frost mass of the radio equipment's

Cable tray	kg	89.9	89.9	89.9	89.9	89.9	89.9	3.7
Antennas	kg	421.2	421.2	280.8				

### Total frost mass

Total frost mass	kg	1357.2	1425.5	1332.0	600.2	647.5	827.3	18.5
------------------	----	--------	--------	--------	-------	-------	-------	------

## 2.3 Operational load

	Units	Section 1	Section 2	Section 3	Section 4	Section 5	Section 6	Base 6
Concentrated vertical load	N	1000	1000	1000				
Vertical surface load	N/m2	2000	2000	2000				
Man falling	N	0	0	0				
Surface area of a landing	m2	2.49	2.49	2.49				
Number of landings in operation	-	2	2	2				
Load on the landings	N	9960	9960	9960				

Operational load	N	9960	9960	9960	0	0	0	0
------------------	---	------	------	------	---	---	---	---

## 2.4 Snow Load

	Units	Section 1	Section 2	Section 3	Section 4	Section 5	Section 6	Base 6
Snow load	N	0	0	0	0	0	0	0

Hypothesis: The effects of snow on the structure are assumed to be negligible

## 2.5 Load exerted by temperature

	Units	Section 1	Section 2	Section 3	Section 4	Section 5	Section 6	Base 6
Load exerted by temperature	N	0	0	0	0	0	0	0

Hypothesis: The effects of temperature on the structure are assumed to be negligible

## 2.6 Wind loads (structure and equipment) (without frost)

### Wind Region

	Unit	Parameter	Value
Wind Region	-	-	3
Fundamental value of basic wind velocity	m/s	Vb,0	26
Directional Coefficient	-	Cdir	1
Seasonal Coefficient	-	Cseason	1
Reference Wind Speed	m/s	Vb	26

$$V_b = C_{dir} \cdot C_{season} \cdot V_{b,0}$$

### Terrain Category

	Unit	Parameter	Value
Terrain Category	-	-	II
Roughness length	m	z0	0.05
Minimum height	m	zmin	2
Terrain factor	-	kr	0.19

$$k_r = 0.19 \cdot \left( \frac{z_0}{z_{0,II}} \right)^{0.07}$$

### Height of the tower

Total height of the tower	m	h	36.25
---------------------------	---	---	-------

### Structural coefficient (without frost)

Coefficient structural	-	CsCd	0.935
------------------------	---	------	-------

### Peak dynamic pressure

	Unit	Parameter	Section 1	Section 2	Section 3	Section 4	Section 5	Section 6
Height above ground	m	z	36.25	30.25	24.25	18.25	12.25	6.25
Roughness coefficient	-	Cr(z)	1.25	1.22	1.17	1.12	1.05	0.92
Orography coefficient	-	CO(z)	1.0	1.0	1.0	1.0	1.0	1.0
Average wind speed	m/s	Vm(z)	32.5	31.6	30.5	29.1	27.2	23.9
Turbulence coefficient	-	kl	1.0	1.0	1.0	1.0	1.0	1.0
Turbulence intensity	-	Iv(z)	0.15	0.16	0.16	0.17	0.18	0.21
Air density	kg/m3	ρ	1.225	1.225	1.225	1.225	1.225	1.225
Peak dynamic pressure	Pa	qp(z)	1337.5	1283.4	1218.7	1137.6	1028.0	853.6

### Strength coefficient of structural elements (without frost)

Reference area	m2	Aref	5.18	5.33	5.58	6.01	6.21	6.91
----------------	----	------	------	------	------	------	------	------

Projected area of main members	m2	-	1.37	1.37	1.68	2.02	2.02	2.63
Projected Area of Top Flanges	m2	-	0.01	0.01	0.01	0.01	0.01	0.01
Projected Area of Bottom Flanges	m2	-	0.01	0.01	0.01	0.02	0.02	0.02
Projected Area of Crossmembers (Tube)	m2	-	0	0	0.27	0.32	0.46	0.51
Projected Area of Crossmembers (Angle)	m2	-	0.27	0.32	0	0	0	0
Projected Area of Diagonals	m2	-	0.56	0.66	0.65	0.69	0.74	0.77
Projected Area of Braces	m2	-						
Projected Area of Gussets (Type "Z")	m2	-	0.08	0.08	0.08	0.08	0.08	0.08
Projected Area of Gussets (Type "X")	m2	-						

Af	0.37	0.42	0.10	0.10	0.11	0.11
Ac	1.94	2.03	2.60	3.03	3.22	3.92

Projected area of the section	m2	As	2.30	2.45	2.70	3.13	3.33	4.03
Circumscribed area	m2	Ac	15.09	15.09	16.44	19.01	21.41	24.11
Solidity ratio	-	$\phi$	0.15	0.16	0.16	0.16	0.16	0.17

C1 (triangular structure)	-	C1	1.9	1.9	1.9	1.9	1.9	1.9
C2 (triangular structure)	-	C2	1.4	1.4	1.4	1.4	1.4	1.4
Overall perpendicular force coefficient (L)	-	Cf,0,f	2.71	2.67	2.66	2.66	2.70	2.65
Overall perpendicular force coefficient (subcritical $\phi$ )	-	Cf,0,c	1.56	1.54	1.54	1.54	1.55	1.53
Overall perpendicular force coefficient (supercritical $\phi$ )	-	Cf,0,c,sup	1.08	1.08	1.08	1.08	1.08	1.08
Overall force coefficient		Cf,s,0	1.74	1.73	1.58	1.57	1.59	1.56
Angle of incidence	°	$\theta$	90	90	90	90	90	90
Reduction coefficient	-	KA	0.8	0.8	0.8	1	1	1
Incidence factor	-	K $\theta$	1.0	1.0	1.0	1.0	1.0	1.0
Structural force coefficient	-	Cf,s	0.61	0.63	0.61	0.82	0.85	0.91

#### Strength coefficient of linear equipment (without frost)

Projected area of the ladder (stile)	m2	-	0.48	0.48	0.48	0.48	0.48	0.48
Projected area of the ladder (rung)	m2	-						
Projected area of the cable tray	m2	-	2.4	2.4	2.4	2.4	2.4	2.4
Projected area of the rail lifeline	m2	-						
Projected area of the cable lifeline	m2	-						
Projected area of the safety cage	m2	-						

Projected area of linear equipment	m2	AA	2.88	2.88	2.88	2.88	2.88	2.88
Drag coefficient of linear equipment	m2	C,f,A,0	2.0	2.0	2.0	2.0	2.0	2.0
Drag coefficient of linear equipment	m2	C,f,A,0	1.2	1.2	1.2	1.2	1.2	1.2
Reduction coefficient	-	KA	1	1	1	0.8	0.8	0.8
Angle of incidence	°	$\psi$	90	90	90	90	90	90
Force coefficient of linear equipment	-	Cf,A	0.74	0.72	0.63	0.47	0.46	0.41

#### Total force coefficient (without frost)

Total force coefficient	-	Cf	1.35	1.35	1.25	1.29	1.31	1.32
-------------------------	---	----	------	------	------	------	------	------

#### Wind force (without frost)

Wind force	N	Fw	8764.7	8659.9	7920.0	8243.7	7799.4	7273.4
------------	---	----	--------	--------	--------	--------	--------	--------

#### Wind force (average) (without frost)

Wind force (average)	N	Fm,w(z)	4544.2	4425.5	3973.2	4032.5	3670.8	3175.4
----------------------	---	---------	--------	--------	--------	--------	--------	--------

#### Wind force (gusts) (without frost)

Wind force (gusts)	N	FT,w(z)	9608.8	9249.6	8273.3	8457.2	7893.7	7297.8
--------------------	---	---------	--------	--------	--------	--------	--------	--------

<b>Max wind force</b>	<b>N</b>	<b>Fw,max</b>	<b>9608.8</b>	<b>9249.6</b>	<b>8273.3</b>	<b>8457.2</b>	<b>7893.7</b>	<b>7297.8</b>
-----------------------	----------	---------------	---------------	---------------	---------------	---------------	---------------	---------------

#### Force coefficient of point equipment (pylon) (without frost)

	Units	Parameter	Section 1	Section 2	Section 3	Section 4	Section 5	Section 6
Level	m	-	33.3	27.3	21.3	15.3	9.3	3.3
Projected area of the jib	m2	-						
Projected area of the lightning rod + support	m2	-	0.11					
Projected area of the secondary ladder	m2	-						

Projected area of the antenna supports	m2	-	0.15	0.15	0.15			
Projected area of the top working landing	m2	-						
Projected area of the working landings	m2	-	1.20	1.20	1.20			
Projected area of the rest landings	m2	-						
Projected area of the anti-intrusion	m2	-						
Projected area of the anti-climbing portcullis	m2	-						
Projected area of the bay frame	m2	-						0.26
Projected area of "other equipment"	m2	-						

Projected area of point equipment	m2	AA	1.46	1.35	1.35	0	0	0.26
Drag coefficient of point equipment	m2	C,f,A,0	1.2	1.2	1.2	1.2	1.2	1.2
Reduction coefficient	-	KA	0.8	0.8	0.8	0.8	0.8	0.8
Force coefficient of point equipment	-	Cf,A	0.96	0.96	0.96	0.96	0.96	0.96

#### Wind force (without frost)

Wind force	N	Fw	1752.77	1555.20	1476.76	0.00	0.00	199.22
------------	---	----	---------	---------	---------	------	------	--------

#### Wind force (average) (without frost)

Wind force (average)	N	Fm,w(z)	908.76	794.76	740.84	0.00	0.00	86.98
----------------------	---	---------	--------	--------	--------	------	------	-------

#### Wind force (gusts) (without icing)

Wind force (gusts)	N	FT,w(z)	1921.58	1661.11	1542.62	0.00	0.00	199.89
--------------------	---	---------	---------	---------	---------	------	------	--------

<b>Max wind force point equipment</b>	<b>N</b>	<b>Fw,max</b>	<b>1921.6</b>	<b>1661.1</b>	<b>1542.6</b>	<b>0.0</b>	<b>0.0</b>	<b>199.9</b>
---------------------------------------	----------	---------------	---------------	---------------	---------------	------------	------------	--------------

#### Force coefficient of point equipment (radio) (without frost)

Level (HMA)	m	-	33.0	27.0	21.0			
Projected antenna area	m2	AA	9.0	9.0	6.0			
Drag coefficient of point equipment	m2	Cf,A,0	1	1	1	1	1	1
Reduction coefficient	-	KA	1	1	1	1	1	1
Force coefficient of point equipment	-	Cf,A	1.0	1.0	1.0	1.0	1.0	1.0

#### Wind force (without frost)

Wind force	N	Fw	11254.97	10799.98	6836.83	0	0	0
------------	---	----	----------	----------	---------	---	---	---

#### Wind force (average) (without frost)

Wind force (average)	N	Fm,w(z)	5835.37	5519.14	3429.82	0.00	0.00	0.00
----------------------	---	---------	---------	---------	---------	------	------	------

#### Wind force (gusty) (without frost)

Wind force (gusts)	N	FT,w(z)	12338.89	11535.45	7141.77	0	0	0
--------------------	---	---------	----------	----------	---------	---	---	---

<b>Max wind force radio equipment</b>	<b>N</b>	<b>Fw,max</b>	<b>12338.9</b>	<b>11535.5</b>	<b>7141.8</b>	<b>0.0</b>	<b>0.0</b>	<b>0.0</b>
---------------------------------------	----------	---------------	----------------	----------------	---------------	------------	------------	------------

### 2.7 Wind loads (structure and equipment) (with frost)

#### Wind Region

	Unit	Parameter	Value
Wind Region	-	-	3
Fundamental value of basic wind velocity	m/s	Vb,0	26
Directional Coefficient	-	Cdir	1
Seasonal Coefficient	-	Cseason	1
Reference Wind Speed	m/s	Vb	26

### Terrain Category

	Unit	Parameter	Value
Terrain Category	-	-	II
Roughness length	m	z0	0.05
Minimum height	m	zmin	2
Terrain factor	-	kr	0.19

### Height of the tower

Total height of the tower	m	h	36.25
---------------------------	---	---	-------

### Structural coefficient (with frost)

Coefficient structural	-	CsCd	1.088
------------------------	---	------	-------

### Peak dynamic pressure

	Unit	Parameter	Section 1	Section 2	Section 3	Section 4	Section 5	Section 6
Height above ground	m	z	36.25	30.25	24.25	18.25	12.25	6.25
Roughness coefficient	-	Cr(z)	1.25	1.22	1.17	1.12	1.05	0.92
Orography coefficient	-	C0(z)	1.0	1.0	1.0	1.0	1.0	1.0
Average wind speed	m/s	Vm(z)	32.5	31.6	30.5	29.1	27.2	23.9
Turbulence coefficient	-	kl	1.0	1.0	1.0	1.0	1.0	1.0
Turbulence intensity	-	Iv(z)	0.15	0.16	0.16	0.17	0.18	0.21
Air density	kg/m3	$\rho$	1.225	1.225	1.225	1.225	1.225	1.225
Peak dynamic pressure	Pa	qp(z)	1337.5	1283.4	1218.7	1137.6	1028.0	853.6

### Strength coefficient of structural elements (with frost)

Reference area	m2	Aref	6.29	6.43	6.69	7.16	7.40	8.14
----------------	----	------	------	------	------	------	------	------

Projected area of main members	m2	-	1.85	1.85	2.16	2.50	2.50	3.11
Projected Area of Top Flanges	m2	-	0.02	0.02	0.02	0.02	0.03	0.03
Projected Area of Bottom Flanges	m2	-	0.02	0.02	0.03	0.03	0.04	0.04
Projected Area of Crossmembers (Tube)	m2	-			0.45	0.53	0.70	0.79
Projected Area of Crossmembers (Angle)	m2	-	0.46	0.50				
Projected Area of Diagonals	m2	-	0.71	0.81	0.80	0.85	0.90	0.95
Projected Area of Braces	m2	-						
Projected Area of Gussets (Type "Z")	m2	-	0.11	0.11	0.11	0.11	0.11	0.11
Projected Area of Gussets (Type "X")	m2	-						
		Af	0.60	0.65	0.16	0.16	0.17	0.18
		Ac	2.56	2.66	3.41	3.87	4.11	4.84

Projected area of the section	m2	As	3.17	3.31	3.57	4.04	4.28	5.02
Circumscribed area	m2	Ac	15.09	15.09	16.44	19.01	21.41	24.11
Filling rate	-	$\varphi$	0.21	0.22	0.22	0.21	0.20	0.21

C1 (triangular structure)	-	C1	1.9	1.9	1.9	1.9	1.9	1.9
C2 (triangular structure)	-	C2	1.4	1.4	1.4	1.4	1.4	1.4
Overall perpendicular force coefficient (L)	-	Cf,0,f	2.51	2.48	2.49	2.50	2.54	2.51
Overall perpendicular force coefficient (subcritical $\phi$ )	-	Cf,0,c	1.46	1.45	1.45	1.46	1.48	1.47
Overall perpendicular force coefficient (supercritical $\phi$ )	-	Cf,0,c,sup	1.08	1.08	1.08	1.08	1.08	1.08
Overall force coefficient	-	Cf,s,0	1.66	1.65	1.50	1.50	1.52	1.50
Angle of incidence	°	$\theta$	90	90	90	90	90	90
Reduction coefficient	-	KA	1	1	1	1	1	1
Incidence factor	-	K $\theta$	1.0	1.0	1.0	1.0	1.0	1.0
Structural force coefficient	-	Cf,s	0.83	0.84	0.80	0.85	0.88	0.93

**Strength coefficient of linear equipment (with frost)**

Projected area of the ladder (stile)	m2	-	0.72	0.72	0.72	0.72	0.72	0.72
Projected area of the ladder (rung)	m2	-						
Projected area of the cable tray	m2	-	2.40	2.40	2.40	2.40	2.40	2.40
Projected area of the rail lifeline	m2	-						
Projected area of the cable lifeline	m2	-						
Projected area of the safety cage	m2	-						

Projected area of linear equipment	m2	AA	3.12	3.12	3.12	3.12	3.12	3.12
Drag coefficient of linear equipment	m2	C,f,A,0	2.0	2.0	2.0	2.0	2.0	2.0
Drag coefficient of linear equipment	m2	C,f,A,0	1.2	1.2	1.2	1.2	1.2	1.2
Reduction coefficient	-	KA	0.8	0.8	0.8	0.8	0.8	0.8
Angle of incidence	°	ψ	90	90	90	90	90	90
Force coefficient of linear equipment	-	Cf,A	0.54	0.53	0.46	0.43	0.42	0.38

**Total force coefficient (with frost)**

Total force coefficient	-	Cf	1.37	1.37	1.26	1.28	1.29	1.30
-------------------------	---	----	------	------	------	------	------	------

**Wind force (with frost)**

Wind force	N	Fw	12496.8	12302.4	11162.7	11302.4	10715.3	9848.5
------------	---	----	---------	---------	---------	---------	---------	--------

**Wind force (average) (with frost)**

Wind force (average)	N	Fm,w(z)	5568.1	5402.8	4812.5	4751.2	4333.9	3695.0
----------------------	---	---------	--------	--------	--------	--------	--------	--------

**Wind force (gusts) (with frost)**

Wind force (gusts)	N	FT,w(z)	13882.5	13263.3	11731.0	11634.5	10861.0	9885.0
--------------------	---	---------	---------	---------	---------	---------	---------	--------

<b>Max wind force</b>	<b>N</b>	<b>Fw,max</b>	<b>13882.5</b>	<b>13263.3</b>	<b>11731.0</b>	<b>11634.5</b>	<b>10861.0</b>	<b>9885.0</b>
-----------------------	----------	---------------	----------------	----------------	----------------	----------------	----------------	---------------

**Force coefficient of point equipment (pylon) (with frost)**

	Units	Parameter	Section 1	Section 2	Section 3	Section 4	Section 5	Section 6
Level	m	-	33.3	27.3	21.3	15.3	9.3	3.3
Projected area of the jib	m2	-						
Projected area of the lightning rod + support	m2	-	0.24					
Projected area of the secondary ladder	m2	-						
Projected area of the antenna supports	m2	-	0.32	0.32	0.32			
Projected area of the top working landing	m2	-						
Projected area of the working landings	m2	-	1.68	1.68	1.68			
Projected area of the rest landings	m2	-						
Projected area of the anti-intrusion	m2	-						
Projected area of the anti-climbing portcullis	m2	-						
Projected area of the bay frame	m2	-						0.56
Projected area of "other equipment"	m2	-						

Projected area of point equipment	m2	AA	2.24	2	2	0	0	0.56
Drag coefficient of linear equipment	m2	Cf,G,0	2.0	2.0	2.0	2.0	2.0	2.0
Drag coefficient of point equipment	m2	C,f,G,0	1.2	1.2	1.2	1.2	1.2	1.2
Reduction coefficient	-	KA	0.8	0.8	0.8	0.8	0.8	0.8
Force coefficient of point equipment	-	Cf,A	0.96	0.96	0.96	0.96	0.96	0.96

**Wind force (with frost)**

Wind force	N	Fw	3129.24	2681.01	2545.79	0.00	0.00	499.31
------------	---	----	---------	---------	---------	------	------	--------

**Wind force (average) (with frost)**

Wind force (average)	N	Fm,w(z)	1394.27	1177.42	1097.54	0.00	0.00	187.33
----------------------	---	---------	---------	---------	---------	------	------	--------

**Wind force (gusts) (with frost)**

Wind force (gusts)	N	FT,w(z)	3476.23	2890.42	2675.41	0.00	0.00	501.16
--------------------	---	---------	---------	---------	---------	------	------	--------

<b>Max wind force point equipment</b>	<b>N</b>	<b>Fw,max</b>	<b>3476.2</b>	<b>2890.4</b>	<b>2675.4</b>	<b>0.0</b>	<b>0.0</b>	<b>501.2</b>
---------------------------------------	----------	---------------	---------------	---------------	---------------	------------	------------	--------------

**Force coefficient of point equipment (radio) (with frost)**

Level (HMA)	m	-	33.0	27.0	21.0			
Projected antenna area	m <sup>2</sup>	AA	10.4	10.4	6.9			
Drag coefficient of point equipment	m <sup>2</sup>	Cf,A,0	1	1	1	1	1	1
Reduction coefficient	-	KA	1	1	1	1	1	1
Force coefficient of point equipment	-	Cf,A	1.0	1.0	1.0	1.0	1.0	1.0

**Wind force (without frost)**

Wind force	N	Fw	15133.95	14522.16	9148.92	0.00	0.00	0.00
------------	---	----	----------	----------	---------	------	------	------

**Wind force (average) (with frost)**

Wind force (average)	N	Fm,w(z)	6743.10	6377.68	3944.29	0.00	0.00	0.00
----------------------	---	---------	---------	---------	---------	------	------	------

**Wind force (gusty) (with frost)**

Wind force (gusts)	N	FT,w(z)	16812.12	15656.46	9614.754	0	0	0
--------------------	---	---------	----------	----------	----------	---	---	---

<b>Max wind force radio equipment</b>	<b>N</b>	<b>Fw,max</b>	<b>16812.1</b>	<b>15656.5</b>	<b>9614.8</b>	<b>0.0</b>	<b>0.0</b>	<b>0.0</b>
---------------------------------------	----------	---------------	----------------	----------------	---------------	------------	------------	------------

**Summary of loads**

**Section height**

	Units		Section 1	Section 2	Section 3	Section 4	Section 5	Section 6	Base 6
Section height	m	-	6.0	6.0	6.0	6.0	6.0	6.0	0.25

**Permanent load**

Tower mass (structure and equipment)	kg	-	2275.0	2380.3	2140.2	944.7	1000.7	1421.5	165.7
--------------------------------------	----	---	--------	--------	--------	-------	--------	--------	-------

**Variable loads**

Frost mass (structure and equipment)	kg	-	1357.2	1425.5	1332.0	600.2	647.5	827.3	18.5
--------------------------------------	----	---	--------	--------	--------	-------	-------	-------	------

Operating load	N	-	9960	9960	9960	0	0	0	0
----------------	---	---	------	------	------	---	---	---	---

Snow load	N	-	0	0	0	0	0	0	0
-----------	---	---	---	---	---	---	---	---	---

Temperature load	N	-	0	0	0	0	0	0	0
------------------	---	---	---	---	---	---	---	---	---

Wind without frost (structure)	N	-	9608.8	9249.6	8273.3	8457.2	7893.7	7297.8	207.9
--------------------------------	---	---	--------	--------	--------	--------	--------	--------	-------

Wind without frost (equipment)	N	-	1921.6	1661.1	1542.6	0.0	0.0	199.9	0.0
--------------------------------	---	---	--------	--------	--------	-----	-----	-------	-----

Wind without frost (antennas)	N	-	12338.9	11535.5	7141.8	0.0	0.0	0.0	0.0
-------------------------------	---	---	---------	---------	--------	-----	-----	-----	-----

Antenna level	m	-	33	27	21	0	0	0	0
---------------	---	---	----	----	----	---	---	---	---

Wind with frost (structure)	N	-	13882.5	13263.3	11731.0	11634.5	10861.0	9885.0	301.0
-----------------------------	---	---	---------	---------	---------	---------	---------	--------	-------

Wind with icing (equipment)	N	-	3476.2	2890.4	2675.4	0.0	0.0	501.2	0.0
-----------------------------	---	---	--------	--------	--------	-----	-----	-------	-----

Wind with icing (antennas)	N	-	16812.12	15656.46	9614.754	0	0	0	0
----------------------------	---	---	----------	----------	----------	---	---	---	---

Antenna level	m	-	33	27	21	0	0	0	0
---------------	---	---	----	----	----	---	---	---	---

**Load combinations**

**1 Weighting coefficients related to reliability class**

Reliability class	-	2
Coefficient for permanent actions	γG	1.1
Coefficient for variable actions	γQ	1.4

**2 Elementary Loads**

	Code	units	Section 1	Section 2	Section 3	Section 4	Section 5	Section 6	Base 6
1 Weight of structure and equipment (Y)	1	N	22317.3	23350.7	20995.4	9267.2	9817.3	13944.8	1625.3
2 Weight of frost (Y)	2	N	13314.6	13983.9	13066.4	5887.8	6352.4	8115.4	181.2
3 Weight of structure and equipment (Z)	3	N	22317.3	23350.7	20995.4	9267.2	9817.3	13944.8	1625.3
4 Weight of frost (Z)	4	N	13314.6	13983.9	13066.4	5887.8	6352.4	8115.4	181.2
-	5								
6 Wind without frost (Y)	6	N	23869.3	22446.2	16957.7	8457.2	7893.7	7497.7	207.9
7 Wind without frost (X)	7								
-	8								
9 Wind with frost (Y)	9	N	34170.9	31810.2	24021.2	11634.5	10861.0	10386.2	301.0
10 Wind with frost (X)	10								
-	11								
12 Operating load (Z)	12		9960	9960	9960	0	0	0	0

**3 Action Combinations**

Hypothesis: Dominant variable action = Wind

ELS · No-Ice Clean Mode	=	1	<b>1</b>						
ELS · With-Ice Clean Mode	=	1	<b>1</b>	+	1	<b>2</b>			
ELS · Offset (Y)	=	1	<b>3</b>	+	1	<b>6</b>	+	0.7	<b>12</b>
ELS · Offset (-Y)	=	1	<b>3</b>	-	1	<b>6</b>	+	0.7	<b>12</b>
ELS · Offset (X)	=	1	<b>3</b>	+	1	<b>7</b>	+	0.7	<b>12</b>
ELS · Offset (-X)	=	1	<b>3</b>	-	1	<b>7</b>	+	0.7	<b>12</b>
ULS · No-frost · Wind (Y+) · (Z) unfavorable	=	1.1	<b>3</b>	+	1.4	<b>6</b>	+	1.05	<b>12</b>
ULS · No-frost · Wind (Y-) · (Z) unfavorable	=	1.1	<b>3</b>	-	1.4	<b>6</b>	+	1.05	<b>12</b>
ULS · no frost · Wind (X+) · (Z) unfavorable	=	1.1	<b>3</b>	+	1.4	<b>7</b>	+	1.05	<b>12</b>
ULS · no frost · Wind (X-) · (Z) unfavorable	=	1.1	<b>3</b>	-	1.4	<b>7</b>	+	1.05	<b>12</b>

Uls - no frost - Wind (Y+) - (Z) favorable	=	1	<b>3</b>	+	1.4	<b>6</b>		
Uls - no frost - Wind (Y-) - (Z) favorable	=	1	<b>3</b>	.	1.4	<b>6</b>		
Uls - no frost - Wind (X+) - (Z) favorable	=	1	<b>3</b>	+	1.4	<b>7</b>		
Uls - no frost - Wind (X-) - (Z) favorable	=	1	<b>3</b>	.	1.4	<b>7</b>		
Uls - with frost - Wind (Y+) - (Z) unfavorable	=	1.1	<b>3</b>	+	0.9	<b>9</b>	+	0.84
Uls - with frost - Wind (Y-) - (Z) unfavorable	=	1.1	<b>3</b>	.	0.9	<b>9</b>	+	0.84
Uls - with frost - Wind (X+) - (Z) unfavorable	=	1.1	<b>3</b>	+	0.9	<b>10</b>	+	0.84
Uls - with frost - Wind (X-) - (Z) unfavorable	=	1.1	<b>3</b>	.	0.9	<b>10</b>	+	0.84
Uls - with frost - Wind (Y+) - (Z) favorable	=	1	<b>3</b>	+	0.9	<b>9</b>	+	0.84
Uls - with frost - Wind (Y-) - (Z) favorable	=	1	<b>3</b>	.	0.9	<b>9</b>	+	0.84
Uls - with frost - Wind (X+) - (Z) favorable	=	1	<b>3</b>	+	0.9	<b>10</b>	+	0.84
Uls - with frost - Wind (X-) - (Z) favorable	=	1	<b>3</b>	.	0.9	<b>10</b>	+	0.84

#### 4 Assumptions for Structural Analysis

According to standard NF EN 1993-3-1

Chapter 5: Structural Analysis

NOTE 1 Freestanding lattice towers can be analyzed based on the initial geometry (first-order theory)

#### Combinations

Uncombined, unweighted values

#### ELS COMBINATIONS

Load combination for deformation Y-Y (103)	=	1	<b>3</b>	+	1	<b>6</b>	+	0.7	<b>12</b>
--	---	---	----------	---	---	----------	---	-----	-----------

Type	Section 1	Section 2	Section 3	Section 4	Section 5	Section 6	Base 6
Additional Dead Load	17611.3	17634.7	15522.0	2650.4	2974.8	4617.7	1370.1
Wind Load Structure (without frost)	9608.8	9249.6	8273.3	8457.2	7893.7	7297.8	207.9
Wind load linear equipment (without frost)	1921.6	1661.1	1542.6	0.0	0.0	199.9	0.0
Wind antennas equipment (without frost)	12338.9	11535.5	7141.8	0.0	0.0	0.0	0.0
0.7*operational load	9960.0	9960.0	9960.0	0.0	0.0	0.0	0.0
				0.0014	0.0013	0.0011	0.0008

#### ULS COMBINATIONS

Uls - No-frost - Wind (Y+) - (Z) unfavorable	110	=	+	1.1	<b>3</b>	+	1.4	<b>6</b>
--	-----	---	---	-----	----------	---	-----	----------

Type	Section 1	Section 2	Section 3	Section 4	Section 5	Section 6	Base 6
Additional Dead Load	19372.5	19398.2	17074.2	2915.4	3272.3	5079.4	1507.1
Wind Load Structure (without frost)	13452.3	12949.5	11582.6	11840.1	11051.1	10216.9	291.0
Wind load linear equipment (without frost)	2690.2	2325.5	2159.7	0.0	0.0	279.8	0.0
Wind antennas equipment (without frost)	17274.4	16149.6	9998.5	0.0	0.0	0.0	0.0
Operational load	10458.0	10458.0	10458.0	0.0	0.0	0.0	0.0

Uls - with frost - Wind (Y+) - (Z) unfavorable	120	=	+	1.1	<b>3</b>	+	0.9	<b>9</b>
--	-----	---	---	-----	----------	---	-----	----------

Type	Section 1	Section 2	Section 3	Section 4	Section 5	Section 6	Base 6
Additional Dead Load	19372.5	19398.2	17074.2	2915.4	3272.3	5079.4	1507.1
Wind Load Structure (without frost)	12494.3	11937.0	10557.9	10471.1	9774.9	8896.5	270.9
Wind load linear equipment (without frost)	3128.6	2601.4	2407.9	0.0	0.0	451.0	0.0
Wind antennas equipment (without frost)	15130.9	14090.8	8653.3	0.0	0.0	0.0	0.0
Weight of frost	11184.2	11746.5	10975.8	4945.8	5336.0	6817.0	152.2

#### ENVELOPE ULS

Type	Section 1	Section 2	Section 3	Section 4	Section 5	Section 6	Base 6
Additional Dead Load	19372.5	19398.2	17074.2	2915.4	3272.3	5079.4	1507.1
Wind Load Structure (without frost)	13452.3	12949.5	11582.6	11840.1	11051.1	10216.9	291.0
Wind load linear equipment (without frost)	3128.6	2601.4	2407.9	0.0	0.0	451.0	0.0
Wind antennas equipment (without frost)	17274.4	16149.6	9998.5	0.0	0.0	0.0	0.0
Non-permanent additional load Z	11184.2	11746.5	10975.8	4945.8	5336.0	6817.0	152.2

**STRUCTURAL COEFFICIENT**

	Units	Parameter	Value
Building height	m	h	36.25
Building width	m	b	4.00
Maximum displacement	m	x1	0.2557
Reference height	m	zs	22
Roughness length	m	z0	0.05
Alpha-a value	-	alpha	0.52
Reference height	m	zt	200
Reference scale	m	Lt	300
Turbulence scale	m	L(zs)	95
Fundamental frequency	Hz	n1	0.986
Mean wind speed	m/s	Vm(zs)	30.0
Dimensionless frequency	-	fl(z,n)	3.11
Wind distribution	-	SL(z,n)	0.06
Quasi-static response coefficient	-	B^2	0.656
hh	-	nh	5.477
Aerodynamic admittance function	-	Rh	0.17
hb	-	nb	0.604
Aerodynamic Admittance Function	-	Rb	0.694
Structural Damping	-	delta_s	0.050
Aerodynamic Damping	-	delta_a	0.265
Special Device Damping	-	delta_d	0.000
Logarithmic Damping Decrement	-	delta	0.315
Resonant Response Coefficient	-	R^2	0.114
Crossover Frequency	Hz	Vm(zs)	0.380
Mean Velocity Integration Time	s	T	600
Peak Factor	-	kp	3.477
Turbulence Intensity	-	lv(zs)	0.165
Structural Coefficient	-	CsCd	0.931

<b>Aerodynamic Damping (without frost)</b>	Units	Parameter	Section 1	Section 2	Section 3	Section 4	Section 5	Section 6	Base 6
Section height	m	-	6	6	6	6	6	6	0.25
Level	m	-	36.25	30.25	24.25	18.25	12.25	6.25	0.25
Area density	kg/m3	rho	1.225	1.225	1.225	1.225	1.225	1.225	1.225
Force coefficient	-	cf	1.35	1.35	1.25	1.29	1.31	1.32	1.37
Mean wind speed	m/s	vm(z)	32.54	31.64	30.55	29.15	27.18	23.85	18.20
C for metal lattice towers	-	ç	2.5	2.5	2.5	2.5	2.5	2.5	2.5
fundamental bending mode	-	φ1 (z)	1.00	0.70	0.45	0.25	0.11	0.03	0.00
mass per unit length	kg/m3	m(s)	379.16	396.72	356.70	157.45	166.79	236.92	662.72
m(s)φ1^2 (s)	-	-	379.16	192.38	71.44	10.11	2.18	0.21	0.00
φ1^2 (s)	-	-	1.00	0.48	0.20	0.06	0.01	0.00	0.00
Equivalent mass kg/m	kg/m3	me	371.717						
Aerodynamic damping	-	delta_a	0.265						

**STRUCTURAL COEFFICIENT**

	Units	Parameter	Value
Building height	m	h	36.25
Building width	m	b	4
Maximum displacement	m	x1	0.3682
Reference height	m	zs	22
Roughness length	m	z0	0.05
Alpha-a value	-	alpha	0.52
Reference height	m	zt	200
Reference scale	m	Lt	300
Turbulence scale	m	L(zs)	95
Fundamental frequency	Hz	n1	0.822
Mean wind speed	m/s	Vm(zs)	30.0
Dimensionless frequency	-	fl(z,n)	2.59
Wind distribution	-	SL(z,n)	0.07
Quasi-static response coefficient	-	B^2	0.656
hh	-	nh	4.564
Aerodynamic admittance function	-	Rh	0.195
hb	-	nb	0.504
Aerodynamic Admittance Function	-	Rb	0.734
Structural Damping	-	delta_s	0.050
Aerodynamic Damping	-	delta_a	0.198
Special Device Damping	-	delta_d	0.000
Logarithmic Damping Decrement	-	delta	0.248
Resonant Response Coefficient	-	R^2	0.201
Crossover Frequency	Hz	Vm(zs)	0.398
Mean Velocity Integration Time	s	T	600
Peak Factor	-	kp	3.491
Turbulence Intensity	-	lv(zs)	0.165
Structural Coefficient	-	CsCd	0.959

Aerodynamic Damping (without frost)	Units	Parameter	Section 1	Section 2	Section 3	Section 4	Section 5	Section 6	Base 6
Section height	m	-	6	6	6	6	6	6	0.25
Level	m	-	36.25	30.25	24.25	18.25	12.25	6.25	0.25
Area density	kg/m <sup>3</sup>	rho	1.225	1.225	1.225	1.225	1.225	1.225	1.225
Force coefficient	-	cf	1.37	1.37	1.26	1.28	1.29	1.30	1.36
Mean wind speed	m/s	vm(z)	32.54	31.64	30.55	29.15	27.18	23.85	18.20
$\zeta$ for metal lattice towers	-	$\zeta$	2.5	2.5	2.5	2.5	2.5	2.5	2.5
fundamental bending mode	-	$\phi_1(z)$	1.00	0.70	0.45	0.25	0.11	0.03	0.00
mass per unit length	kg/m <sup>3</sup>	m(s)	605.37	634.30	578.69	257.48	274.71	374.79	736.60
$m(s)\phi_1^2(s)$	-	-	605.37	307.58	115.89	16.54	3.58	0.33	0.00
$\phi_1^2(s)$	-	-	1.00	0.48	0.20	0.06	0.01	0.00	0.00
Equivalent mass kg/m	kg/m <sup>3</sup>	me	595.057						
Aerodynamic damping	-	delta_a	0.198						

**ANNEX B**

**Load Calculation 2nd Design Loop Non-Tapered**  
**Results from the triangular model, incidence angle 0°**

**Section height**

	Units	Section 1	Section 2	Section 3	Section 4	Section 5	Section 6	Base 6
Section height	m	6.0	6.0	6.0	6.0	6.0	6.0	0.25

**Permanent load**

Tower mass (structure and equipment)	kg	2188.8	2183.2	1957.7	641.4	655.6	826.8	50.7
--------------------------------------	----	--------	--------	--------	-------	-------	-------	------

**Variable loads**

Frost mass (structure and equipment)	kg	1595.0	1595.2	1454.8	672.4	679.9	783.1	40.6
--------------------------------------	----	--------	--------	--------	-------	-------	-------	------

Operating load	N	9960	9960	9960	0	0	0	0
----------------	---	------	------	------	---	---	---	---

Snow load	N	0	0	0	0	0	0	0
-----------	---	---	---	---	---	---	---	---

Temperature load	N	0	0	0	0	0	0	0
------------------	---	---	---	---	---	---	---	---

Wind without frost (structure)	N	14006.2	13080.1	12130.5	10301.2	9181.0	7554.8	165.7
--------------------------------	---	---------	---------	---------	---------	--------	--------	-------

Wind without frost (equipment)	N	2051.5	1770.6	1642.0	0.0	0.0	212.3	0.0
--------------------------------	---	--------	--------	--------	-----	-----	-------	-----

Wind without frost (antennas)	N	13173.2	12295.5	7601.9	0.0	0.0	0.0	0.0
-------------------------------	---	---------	---------	--------	-----	-----	-----	-----

Antenna level	m	33	27	21	0	0	0	0
---------------	---	----	----	----	---	---	---	---

Wind with frost (structure)	N	16457.6	15353.7	14224.6	13024.9	11603.5	9544.9	218.5
-----------------------------	---	---------	---------	---------	---------	---------	--------	-------

Wind with icing (equipment)	N	3312.5	2757.3	2554.5	0.0	0.0	479.3	0.0
-----------------------------	---	--------	--------	--------	-----	-----	-------	-----

Wind with icing (antennas)	N	16020.40	14935.18	9180.20	0	0	0	0
----------------------------	---	----------	----------	---------	---	---	---	---

Antenna level	m	33	27	21	0	0	0	0
---------------	---	----	----	----	---	---	---	---

**ELS COMBINATIONS**

Type	Units	Section 1	Section 2	Section 3	Section 4	Section 5	Section 6	Base 6
Additional Dead Load	N	17573.8	17518.5	15306.4	2394.1	2533.5	4213.0	453.9
Wind Load Structure (without frost)	N	14006.2	13080.1	12130.5	10301.2	9181.0	7554.8	165.7
Wind load linear equipment (without frost)	N	2051.5	1770.6	1642.0	0.0	0.0	212.3	0.0
Wind antennas equipment (without frost)	N	13173.2	12295.5	7601.9	0.0	0.0	0.0	0.0
0.7*operational load	N	9960.0	9960.0	9960.0	0.0	0.0	0.0	0.0

**Results from the square model, incidence angle 0°**

**Section height**

	Units	Section 1	Section 2	Section 3	Section 4	Section 5	Section 6	Base 6
Section height	m	6.0	6.0	6.0	6.0	6.0	6.0	0.25

**Permanent load**

Tower mass (structure and equipment)	kg	2333.1	2329.7	2104.1	790.2	806.0	979.9	65.5
--------------------------------------	----	--------	--------	--------	-------	-------	-------	------

**Variable loads**

Frost mass (structure and equipment)	kg	1764.0	1764.2	1623.8	841.5	849.0	952.2	52.6
--------------------------------------	----	--------	--------	--------	-------	-------	-------	------

Operating load	N	9960	9960	9960	0	0	0	0
----------------	---	------	------	------	---	---	---	---

Snow load	N	0	0	0	0	0	0	0
-----------	---	---	---	---	---	---	---	---

Temperature load	N	0	0	0	0	0	0	0
Wind without frost (structure)	N	14839.6	13861.1	12857.0	10974.7	9782.2	8050.0	165.6
Wind without frost (equipment)	N	2034.5	1756.2	1629.0	0.0	0.0	210.6	0.0
Wind without frost (antennas)	N	13063.7	12195.8	7541.5	0.0	0.0	0.0	0.0
Antenna level	m	33	27	21	0	0	0	0
Wind with frost (structure)	N	17285.5	16127.0	14942.0	13682.2	12189.2	10026.9	220.1
Wind with icing (equipment)	N	3301.6	2748.4	2546.4	0.0	0.0	477.8	0.0
Wind with icing (antennas)	N	15967.5	14887.0	9151.2	0	0	0	0
Antenna level	m	33	27	21	0	0	0	0

#### ELS COMBINATIONS

Type	Units	Section 1	Section 2	Section 3	Section 4	Section 5	Section 6	Base 6
Additional Dead Load	N	17690.0	17656.9	15443.1	2554.2	2709.1	4415.4	583.5
Wind Load Structure (without frost)	N	14839.6	13861.1	12857.0	10974.7	9782.2	8050.0	165.6
Wind load linear equipment (without frost)	N	2034.5	1756.2	1629.0	0.0	0.0	210.6	0.0
Wind antennas equipment (without frost)	N	13063.7	12195.8	7541.5	0.0	0.0	0.0	0.0
0.7*operational load	N	9960.0	9960.0	9960.0	0.0	0.0	0.0	0.0

#### Results from the square model, incidence angle 45°

##### Section height

	Units	Section 1	Section 2	Section 3	Section 4	Section 5	Section 6	Base 6
Section height	m	6.0	6.0	6.0	6.0	6.0	6.0	0.25

##### Permanent load

Tower mass (structure and equipment)	kg	2333.1	2329.7	2104.1	790.2	806.0	979.9	65.5
--------------------------------------	----	--------	--------	--------	-------	-------	-------	------

##### Variable loads

Frost mass (structure and equipment)	kg	1764.0	1764.2	1623.8	841.5	849.0	952.2	52.6
Operating load	N	9960	9960	9960	0	0	0	0
Snow load	N	0	0	0	0	0	0	0
Temperature load	N	0	0	0	0	0	0	0
Wind without frost (structure)	N	20343.4	19007.0	17631.8	15731.4	14024.7	11541.6	182.1
Wind without frost (equipment)	N	1012.2	873.8	810.6	0.0	0.0	104.8	0.0
Wind without frost (antennas)	N	9191.7	8582.0	5307.4	0.0	0.0	0.0	0.0
Antenna level	m	33	27	21	0	0	0	0
Wind with frost (structure)	N	24937.7	23275.0	21569.3	19756.5	17605.0	14483.0	236.6
Wind with icing (equipment)	N	1632.8	1359.6	1259.9	0.0	0.0	236.5	0.0
Wind with icing (antennas)	N	11210.8	10454.8	6459.1	0	0	0	0
Antenna level	m	33	27	21	0	0	0	0

#### ELS COMBINATIONS

Type	Units	Section 1	Section 2	Section 3	Section 4	Section 5	Section 6	Base 6
Additional Dead Load	N	17690.0	17656.9	15443.1	2554.2	2709.1	4415.4	583.5
Wind Load Structure (without frost)	N	20343.4	19007.0	17631.8	15731.4	14024.7	11541.6	182.1
Wind load linear equipment (without frost)	N	1012.2	873.8	810.6	0.0	0.0	104.8	0.0
Wind antennas equipment (without frost)	N	9191.7	8582.0	5307.4	0.0	0.0	0.0	0.0
0.7*operational load	N	9960.0	9960.0	9960.0	0.0	0.0	0.0	0.0

**Results from the hexagon model, incidence angle 0°**

**Section height**

	Units	Section 1	Section 2	Section 3	Section 4	Section 5	Section 6	Base 6
Section height	m	6.0	6.0	6.0	6.0	6.0	6.0	0.25

**Permanent load**

Tower mass (structure and equipment)	kg	2400.4	2399.1	2173.4	861.6	879.5	1053.4	91.4
--------------------------------------	----	--------	--------	--------	-------	-------	--------	------

**Variable loads**

Frost mass (structure and equipment)	kg	2046.9	2047.3	1906.9	1124.7	1132.3	1235.5	49.7
--------------------------------------	----	--------	--------	--------	--------	--------	--------	------

Operating load	N	23560	23560	23560	0	0	0	0
----------------	---	-------	-------	-------	---	---	---	---

Snow load	N	0	0	0	0	0	0	0
-----------	---	---	---	---	---	---	---	---

Temperature load	N	0	0	0	0	0	0	0
------------------	---	---	---	---	---	---	---	---

Wind without frost (structure)	N	25358.8	23707.9	21958.1	19275.6	17166.4	14119.5	393.3
--------------------------------	---	---------	---------	---------	---------	---------	---------	-------

Wind without frost (equipment)	N	2191.6	1888.6	1749.2	0.0	0.0	225.6	0.0
--------------------------------	---	--------	--------	--------	-----	-----	-------	-----

Wind without frost (antennas)	N	14072.8	13115.1	8098.1	0.0	0.0	0.0	0.0
-------------------------------	---	---------	---------	--------	-----	-----	-----	-----

Antenna level	m	33	27	21	0	0	0	0
---------------	---	----	----	----	---	---	---	---

Wind with frost (structure)	N	33128.8	30933.9	28614.9	26239.4	23361.2	19206.4	517.4
-----------------------------	---	---------	---------	---------	---------	---------	---------	-------

Wind with icing (equipment)	N	3597.4	2989.0	2764.9	0.0	0.0	517.4	0.0
-----------------------------	---	--------	--------	--------	-----	-----	-------	-----

Wind with icing (antennas)	N	17398.2	16190.4	9936.4	0	0	0	0
----------------------------	---	---------	---------	--------	---	---	---	---

Antenna level	m	33	27	21	0	0	0	0
---------------	---	----	----	----	---	---	---	---

**ELS COMBINATIONS**

Type	Units	Section 1	Section 2	Section 3	Section 4	Section 5	Section 6	Base 6
Additional Dead Load	N	17865.1	17851.9	15638.1	2769.3	2945.2	4651.5	808.9
Wind Load Structure (without frost)	N	25358.8	23707.9	21958.1	19275.6	17166.4	14119.5	393.3
Wind load linear equipment (without frost)	N	2191.6	1888.6	1749.2	0.0	0.0	225.6	0.0
Wind antennas equipment (without frost)	N	14072.8	13115.1	8098.1	0.0	0.0	0.0	0.0
0.7*operational load	N	23560.0	23560.0	23560.0	0.0	0.0	0.0	0.0